



Defense Threat Reduction Agency  
8725 John J. Kingman Road, MS  
6201 Fort Belvoir, VA 22060-6201



DTRA-TR-16-53

# TECHNICAL REPORT

## Novel Chalcogenide Materials for x-ray and $\gamma$ -ray Detection

Distribution Statement A. Approved for public release; distribution is unlimited.

May 2016

HDTRA1-09-1-0044

Mercouri Kanatzidis

Prepared by:  
Northwest University  
2145 N Sheridan Road  
Evanston, IL 60208

DESTRUCTION NOTICE:

Destroy this report when it is no longer needed.  
Do not return to sender.

PLEASE NOTIFY THE DEFENSE THREAT REDUCTION  
AGENCY, ATTN: DTRIAC/ J9STT, 8725 JOHN J. KINGMAN ROAD,  
MS-6201, FT BELVOIR, VA 22060-6201, IF YOUR ADDRESS  
IS INCORRECT, IF YOU WISH IT DELETED FROM THE  
DISTRIBUTION LIST, OR IF THE ADDRESSEE IS NO  
LONGER EMPLOYED BY YOUR ORGANIZATION.

<b>REPORT DOCUMENTATION PAGE</b>				<i>Form Approved</i> <b>OMB No. 0704-0188</b>	
Public reporting burden for this collection of information is estimated to average 1 hour per response, including the time for reviewing instructions, searching existing data sources, gathering and maintaining the data needed, and completing and reviewing this collection of information. Send comments regarding this burden estimate or any other aspect of this collection of information, including suggestions for reducing this burden to Department of Defense, Washington Headquarters Services, Directorate for Information Operations and Reports (0704-0188), 1215 Jefferson Davis Highway, Suite 1204, Arlington, VA 22202-4302. Respondents should be aware that notwithstanding any other provision of law, no person shall be subject to any penalty for failing to comply with a collection of information if it does not display a currently valid OMB control number. <b>PLEASE DO NOT RETURN YOUR FORM TO THE ABOVE ADDRESS.</b>					
<b>1. REPORT DATE (DD-MM-YYYY)</b>		<b>2. REPORT TYPE</b>		<b>3. DATES COVERED (From - To)</b>	
<b>4. TITLE AND SUBTITLE</b>				<b>5a. CONTRACT NUMBER</b>	
				<b>5b. GRANT NUMBER</b>	
				<b>5c. PROGRAM ELEMENT NUMBER</b>	
<b>6. AUTHOR(S)</b>				<b>5d. PROJECT NUMBER</b>	
				<b>5e. TASK NUMBER</b>	
				<b>5f. WORK UNIT NUMBER</b>	
<b>7. PERFORMING ORGANIZATION NAME(S) AND ADDRESS(ES)</b>				<b>8. PERFORMING ORGANIZATION REPORT NUMBER</b>	
<b>9. SPONSORING / MONITORING AGENCY NAME(S) AND ADDRESS(ES)</b>				<b>10. SPONSOR/MONITOR'S ACRONYM(S)</b>	
				<b>11. SPONSOR/MONITOR'S REPORT NUMBER(S)</b>	
<b>12. DISTRIBUTION / AVAILABILITY STATEMENT</b>					
<b>13. SUPPLEMENTARY NOTES</b>					
<b>14. ABSTRACT</b>					
<b>15. SUBJECT TERMS</b>					
<b>16. SECURITY CLASSIFICATION OF:</b>			<b>17. LIMITATION OF ABSTRACT</b>	<b>18. NUMBER OF PAGES</b>	<b>19a. NAME OF RESPONSIBLE PERSON</b>
<b>a. REPORT</b>	<b>b. ABSTRACT</b>	<b>c. THIS PAGE</b>			<b>19b. TELEPHONE NUMBER (include area code)</b>

## UNIT CONVERSION TABLE

### U.S. customary units to and from international units of measurement<sup>\*</sup>

U.S. Customary Units	<div style="display: flex; align-items: center; justify-content: center;"> <div style="margin-right: 10px;"> </div> Multiply by </div> <div style="display: flex; align-items: center; justify-content: center;"> <div style="margin-right: 10px;"> </div> Divide by<sup>†</sup> </div>	International Units
<b>Length/Area/Volume</b>		
inch (in)	2.54 $\times 10^{-2}$	meter (m)
foot (ft)	3.048 $\times 10^{-1}$	meter (m)
yard (yd)	9.144 $\times 10^{-1}$	meter (m)
mile (mi, international)	1.609 344 $\times 10^3$	meter (m)
mile (nmi, nautical, U.S.)	1.852 $\times 10^3$	meter (m)
barn (b)	1 $\times 10^{-28}$	square meter (m <sup>2</sup> )
gallon (gal, U.S. liquid)	3.785 412 $\times 10^{-3}$	cubic meter (m <sup>3</sup> )
cubic foot (ft <sup>3</sup> )	2.831 685 $\times 10^{-2}$	cubic meter (m <sup>3</sup> )
<b>Mass/Density</b>		
pound (lb)	4.535 924 $\times 10^{-1}$	kilogram (kg)
unified atomic mass unit (amu)	1.660 539 $\times 10^{-27}$	kilogram (kg)
pound-mass per cubic foot (lb ft <sup>-3</sup> )	1.601 846 $\times 10^1$	kilogram per cubic meter (kg m <sup>-3</sup> )
pound-force (lbf avoirdupois)	4.448 222	newton (N)
<b>Energy/Work/Power</b>		
electron volt (eV)	1.602 177 $\times 10^{-19}$	joule (J)
erg	1 $\times 10^{-7}$	joule (J)
kiloton (kt) (TNT equivalent)	4.184 $\times 10^{12}$	joule (J)
British thermal unit (Btu) (thermochemical)	1.054 350 $\times 10^3$	joule (J)
foot-pound-force (ft lbf)	1.355 818	joule (J)
calorie (cal) (thermochemical)	4.184	joule (J)
<b>Pressure</b>		
atmosphere (atm)	1.013 250 $\times 10^5$	pascal (Pa)
pound force per square inch (psi)	6.984 757 $\times 10^3$	pascal (Pa)
<b>Temperature</b>		
degree Fahrenheit (°F)	$[T(^{\circ}\text{F}) - 32]/1.8$	degree Celsius (°C)
degree Fahrenheit (°F)	$[T(^{\circ}\text{F}) + 459.67]/1.8$	kelvin (K)
<b>Radiation</b>		
curie (Ci) [activity of radionuclides]	3.7 $\times 10^{10}$	per second (s <sup>-1</sup> ) [becquerel (Bq)]
roentgen (R) [air exposure]	2.579 760 $\times 10^{-4}$	coulomb per kilogram (C kg <sup>-1</sup> )
rad [absorbed dose]	1 $\times 10^{-2}$	joule per kilogram (J kg <sup>-1</sup> ) [gray (Gy)]
rem [equivalent and effective dose]	1 $\times 10^{-2}$	joule per kilogram (J kg <sup>-1</sup> ) [sievert (Sv)]

<sup>\*</sup> Specific details regarding the implementation of SI units may be viewed at <http://www.bipm.org/en/si/>.

<sup>†</sup> Multiply the U.S. customary unit by the factor to get the international unit. Divide the international unit by the factor to get the U.S. customary unit.

**FINAL REPORT OF PROJECT:**  
**Novel chalcogenide materials for x-ray and  $\gamma$ -ray detection**

*HDTRA1-09-1-0044*

*Mercouri Kanatzidis, PI*  
*Northwestern University*

*Bruce Wessels, Arthur J. Freeman Northwestern University (co-PIs)*

*Department of Materials Science & Engineering,*

*Department of Physics and Astronomy*

*Northwestern University, Evanston, Illinois 60208*

*October 5, 2014*

## **OBJECTIVES**

This project focused on exploring the potential of a new heavy atom chalcogenide family of semiconductors for room temperature gamma radiation detection. Its goal was to accelerate nuclear detector material discovery and development through innovative materials design/selection, synthesis and characterization. The project succeeded in expanding the currently small portfolio of potential materials. It allowed the assessment of fundamental limits for performance of the new materials. The project also focused in delineating clear relationships between material composition, structure and properties and the targeted performance and how they evolve from one material to the next. The close coupling of experiment and theory created an accelerated fundamental materials discovery effort which is greatly needed to develop the next generation radiation detector materials. The project investigated ternary chalcogenide semiconductors using selection criteria relevant to  $\gamma$ -ray detection at room temperature. These include heavy element composition, extended structures and wide energy band gap  $1.8 < E_g < 2.5$  eV.

## **PROJECT REPORT**

This project focused on the synthesis, physical characterization and properties optimization of several new compounds. These compounds possess good properties within the required selection criteria to be considered as the best candidates for the X-ray and gamma ray detectors on par or even may be better than the bench mark material CZT.

### **1. TERNARY MATERIALS**

The availability of highly efficient hard radiation detection materials will impact biomedical diagnostics, nuclear safety and homeland security applications. Semiconductor materials promise excellent energy-resolution for X-ray and  $\gamma$ -ray detection; however, few are being considered because of strict demands on physical and crystal properties. These include the challenging combination of high mass density (e.g.  $> 6 \text{ g/cm}^3$ ) and high atomic number (Z) with a wide energy band gap ( $> 1.5$  eV). In this DTRA funded project we applied a materials design tool called “dimensional reduction” which creates new candidate semiconductors for hard radiation detection. We then utilized theoretical electronic band structure calculations as a guide to aid in the selection of new materials among the variety of possibilities indicated by dimensional reduction. As a result of this concept, we discovered several promising new materials (ternary compounds  $\text{Cs}_2\text{Hg}_6\text{S}_7$ ,  $\text{Cs}_2\text{Cd}_3\text{Te}_4$ ) that show high  $\mu \cdot \tau$  products and great promise as superior new detector materials. Several quaternary materials were also identified which are presented in this final report.

Main achievements for  $\text{Cs}_2\text{Hg}_6\text{S}_7$ : successful scale-up synthesis of material, Bridgman-Stockbarger single crystalline boules of dimensions 1/4 inch in diameter  $> 1.5$  in long, and electrical resistivity  $> 2 \text{ M}\Omega \cdot \text{cm}$ . For  $\text{Cs}_2\text{Cd}_3\text{Te}_4$ : the large single crystals of 6-8 mm plate grown by direct heating of the starting binaries and electrical resistivity  $\sim 2 \text{ M}\Omega \cdot \text{cm}$ . We have characterized the optical and optoelectronic properties of high Z chalcogenide semiconductor materials for x-ray and  $\gamma$ -ray detector applications. The semiconductor crystals are grown by the modified Bridgman method. We have measured the bandgap energy and optical absorption

coefficient of the materials using UV-Vis-near IR transmission and reflection spectra over the range of 300-2500 nm. For determination of detector material properties, critical parameters such as the mobility-lifetime product of electron and hole carriers, as well as carrier lifetimes have been obtained using steady-state and transient photoconductivity measurements. We have built an x-ray/gamma ray spectrometer system (>20 keV), and tested high Z chalcogenide materials as potential detectors at x-ray and  $\gamma$ -ray energies. To improve detector performance, we are developing device processing techniques that include cutting and polishing of crystals, electrode deposition, and encapsulation. The compounds investigated most extensively are described below.

### 1.1. Synthesis and Crystal Growth

**$\text{Cs}_2\text{Hg}_6\text{S}_7$ :** The synthesis of the compound was based on mixing  $\text{Cs}_2\text{S}$ , prepared separately in liquid ammonia, and  $\text{HgS}$  inside carbon coated silica tubes. Careful control of the synthesis and purification of the starting materials allowed the successful scaling up of each reaction batch to about 10g. We have also identified the conditions to rapidly produce the precursor phase, before crystal growth, by flame reaction and thus speed up the overall growth process.

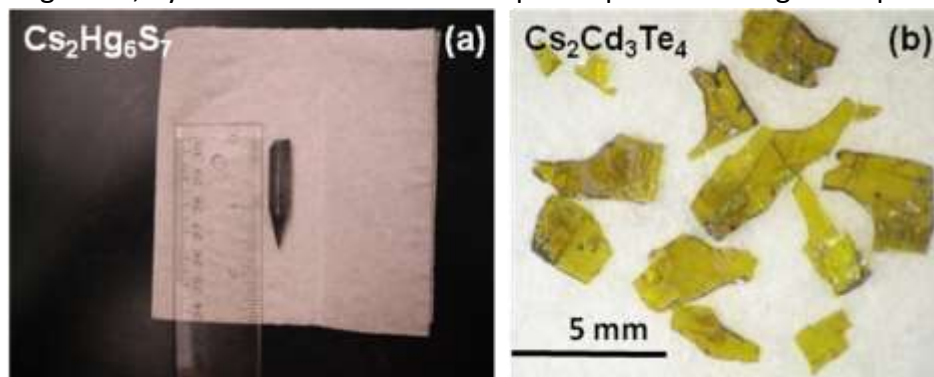


**Figure 1.** Large single crystals of  $\text{Cs}_2\text{Hg}_6\text{S}_7$  and  $\text{Cs}_2\text{Cd}_3\text{Te}_4$ .

$\text{Cs}_2\text{Hg}_6\text{S}_7$  crystallizes in a new structure type. The structure comprises a three-dimensional  $\text{HgS}$  network that is composed of channels (Figure 2a). 2D layered structure of  $\text{Cs}_2\text{Cd}_3\text{Te}_4$  comprising  $[\text{CdTe}]^{2-}$  sheets separated by  $\text{Cs}^+$  cations (Figure 2b). The attenuation length of such materials is much shorter than the CZT benchmark, Figure 3.

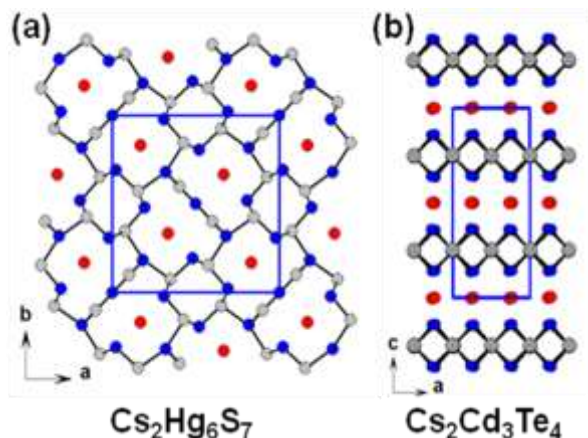


**Figure 2.** Crystal structure of (a)  $\text{Cs}_2\text{Hg}_6\text{S}_7$  and (b)  $\text{Cs}_2\text{Cd}_3\text{Te}_4$ .

The Bridgman and the modified Bridgman-Stockbarger (BS) growth techniques were utilized for the growth of single crystalline boules. The modified BS method was found to be superior in producing higher quality crystals with better physical properties (Figure 1a). A study of the optimal growth conditions with the BS method, in terms of temperature profiles and feed speed, was also initiated. So far, the best crystals were grown by keeping the hot zone of the furnace about 40 °C above the melting point and the post annealing zone about 10 °C below the recrystallization point. Typical dimensions of single crystalline boules using the above conditions are ~1/4 inch in diameter and >1.5 inch in length. The single crystalline nature of the ingots was confirmed with backscattering Laue reflections.

**Synthesis, crystal growth and annealing treatment of  $\text{Cs}_2\text{Hg}_6\text{S}_7$ .** High purity Hg (99.9999%, Aldrich), Cs (>99.9%, Aldrich), and S (99.98%, 5N Plus Inc.) were used as starting materials. All manipulations were carried out in a glovebox under  $\text{N}_2$  protective atmosphere with  $\text{O}_2$  and  $\text{H}_2\text{O}$  levels below 0.1 ppm. Stoichiometric amounts of Hg and  $\text{Cs}_2\text{S}_7$  were weighed and loaded into a fused silica tube and subsequently sealed under a  $10^{-4}$  mbar vacuum. In order to prevent the volatilization of Hg during sealing, the tube was cooled using liquid  $\text{N}_2$ . The mixture was raised to 240°C over 12 h and kept there for 1 d, followed by heating at 620°C for 1 d, and then cooling to room temperature. The polycrystalline raw  $\text{Cs}_2\text{Hg}_6\text{S}_7$  material was then transferred into a conically tipped fused silica ampoule and sealed. The ampoule was loaded into a two-zone vertical Bridgman furnace. The temperature gradient of the furnace was set to 5-20°C/cm at the middle of the growth zone. The growth run was unseeded. A stepping motor was used to control the lowering speed at 0.8-2.0 cm/d. After the growth run, the furnace was slowly cooled to room temperature. When  $\text{Cs}_2\text{Hg}_6\text{S}_7$  is ground to a powder and exposed in air for several weeks it shows signs of decomposition where some HgS can be seen in the powder X-ray diffraction pattern. Therefore, the material should be stored in an inert atmosphere.

Because all elements in  $\text{Cs}_2\text{Hg}_6\text{S}_7$  have relatively high vapor pressures above the melting point, it was difficult to determine which element would be off stoichiometric during the growth procedure. After the first growth run, some orange or reddish  $\text{Cs}_2\text{S}_{1+x}$  was found to have condensed at the top of the tube. Therefore, an excess of  $\text{Cs}_2\text{S}_7$  and S were added to compensate for the loss of Cs and S in further growth runs. The starting compositions for different growth runs are summarized in **Table 1**.

The  $\text{Cs}_2\text{Hg}_6\text{S}_7$  ingots were cut into wafers and rectangular blocks using a Struers Accutom-50 waferizing saw and then polished with different grit SiC sandpapers. The crystals were oriented using Laue X-ray back-reflection with white Ag X-ray irradiation. The scanned X-ray diffraction pattern was oriented using OrientExpress software. Crystals used for annealing were loaded into a fused silica tube and sealed under a  $10^{-4}$  mbar vacuum. The crystals were heated for 1.5 d at 280°C and cooled to room temperature in 12h. The DC resistivity values of the  $\text{Cs}_2\text{Hg}_6\text{S}_7$  samples were measured using a Keithley Model 617 electrometer.

**Defects, optical and thermal characterization.** To understand the microscopic defects in the samples,  $\text{Cs}_2\text{Hg}_6\text{S}_7$  crystals were examined under a Hitachi S3400N-II scanning electron microscope (SEM) equipped with an energy dispersive spectroscopy (EDS) detector. Powder X-ray diffraction (PXRD) patterns of ground crystals were collected using a CPS 120 INEL



diffractometer. Differential thermal analysis was performed on the samples using a computer-controlled Shimadzu DTA-50 thermal analyzer. Solid-state diffuse reflectance UV-vis spectroscopy was performed on powder samples of crushed crystals at room temperature with a Shimadzu UV-3101 PC double-beam, double-monochromator spectrophotometer operating in the 200-2500 nm region.

Low temperature Photoluminescence (PL) measurements were performed on polished samples with the samples placed in a helium vapor cryostat. The excitation source was a He-Ne laser with emission wavelength of 633 nm. The PL spectrum was analyzed with a 0.75-m SPEX grating monochromator and the signal was detected with a R928 Hamamatsu photomultiplier tube (PMT) with a phase sensitive detection lock-in system.

**Table 1.** Material properties of  $\text{Cs}_2\text{Hg}_6\text{S}_7$  crystals grown with different synthesis conditions

Sample No.	$\text{Cs}_2\text{S}_7$ excess	S excess	Resistivity (not annealed) ( $\text{M}\Omega\cdot\text{cm}$ )	Resistivity (annealed) ( $\text{M}\Omega\cdot\text{cm}$ )	$(\mu\tau)_e$ ( $\text{cm}^2/\text{V}$ )	$(\mu\tau)_h$ ( $\text{cm}^2/\text{V}$ )
Sample 1	none	none	1.7	6.8	$9.00 \times 10^{-4}$	$1.20 \times 10^{-4}$
Sample 2	none	5%	2.1	8.3	$1.20 \times 10^{-3}$	$1.01 \times 10^{-4}$
Sample 3	3%	none	0.8	1.2	—	—
Sample 4	1%	2%	1.3	3.5	$8.16 \times 10^{-5}$	$1.09 \times 10^{-4}$

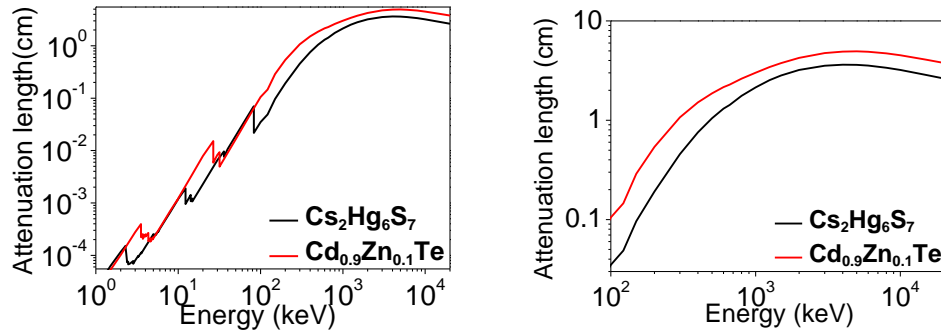


**Figure 3.** (a) Calculated attenuation length as a function of incident photon energy in  $\text{Cs}_2\text{Hg}_6\text{S}_7$  and CZT. (b) Expanded view of the high energy region.

Photoconductivity was measured in a homemade setup. Gold electrodes of  $\sim 80\text{nm}$  were evaporated on the front and back surfaces of the samples in a parallel plate configuration. A He-Ne laser (633nm) chopped at 585 Hz was focused on the surface of the samples. The output photocurrent signal is collected as the voltage drop on a load resistance  $R$  (5 k $\Omega$ ) and analyzed by the lock-in amplifier. The  $\mu\tau$  products for electrons and holes were obtained by applying either negative or positive voltage to the illuminated electrode, and measuring the photocurrent for electrons and holes.

The thermal expansion coefficient of a  $\text{Cs}_2\text{Hg}_6\text{S}_7$  crystal was determined by a single crystal X-ray diffraction study on a Stoe IPDS II diffractometer in the range of 100–400 K. One black needle single crystal with dimensions  $0.28 \times 0.02 \times 0.02 \text{ mm}^3$  was selected from the starting polycrystalline raw material and mounted on the tip of a glass fiber. Individual frames were

collected with a 2 min exposure time and a 1.0  $\omega$  rotation. X-Area software was used for data extraction. Two coins of  $\varnothing \sim 8$  mm and 1~2 mm thickness were cut (parallel and perpendicular to the  $c$ -axis, respectively) and polished for the thermal diffusivity measurements. The thermal diffusivity  $D$  along two different directions (parallel and perpendicular to the  $c$ -axis) was measured using the laser flash diffusivity method in a Netzsch LFA457. The density of the  $\text{Cs}_2\text{Hg}_6\text{S}_7$  crystal was determined by the helium gas displacement method (pycnometry), the volume of small  $\text{Cs}_2\text{Hg}_6\text{S}_7$  crystal fragments was measured using an Accupyc 1340 Gas Pycnometer and the mass was measured using a 4 digit balance.

### 1.2. Discussion of synthesis and crystal growth

Our original method for the synthesis of  $\text{Cs}_2\text{Hg}_6\text{S}_7$  involved the combination of  $\text{Cs}_2\text{S}$  and  $\text{HgS}$  but it tends to give incomplete reaction with some unreacted  $\text{HgS}$  remaining as a secondary phase. The new method we developed last year uses  $\text{Cs}_2\text{S}_7$  and  $\text{Hg}$  as starting materials is more effective in producing high purity  $\text{Cs}_2\text{Hg}_6\text{S}_7$  as determined from X-ray diffraction, **Figure 4**. The DTA curve of the  $\text{Cs}_2\text{Hg}_6\text{S}_7$  product (**Figure 5a**) indicates that there is only one endothermic peak at 587°C and one exothermic peak at 542°C, confirming the purity of the material. Likewise, the electronic absorption spectrum (**Figure 5b**) confirms the band gap of  $\text{Cs}_2\text{Hg}_6\text{S}_7$  is 1.63 eV; these results are in good agreement with previous reports.

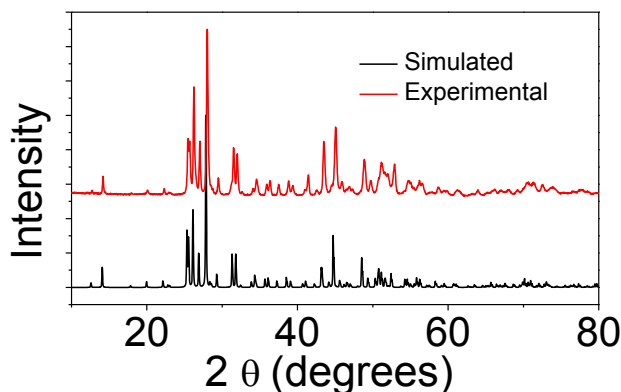


**Figure 4.** Powder X-ray diffraction pattern of the synthesized  $\text{Cs}_2\text{Hg}_6\text{S}_7$  compound, using  $\text{Cs}_2\text{S}_7$  and  $\text{Hg}$  as starting materials.

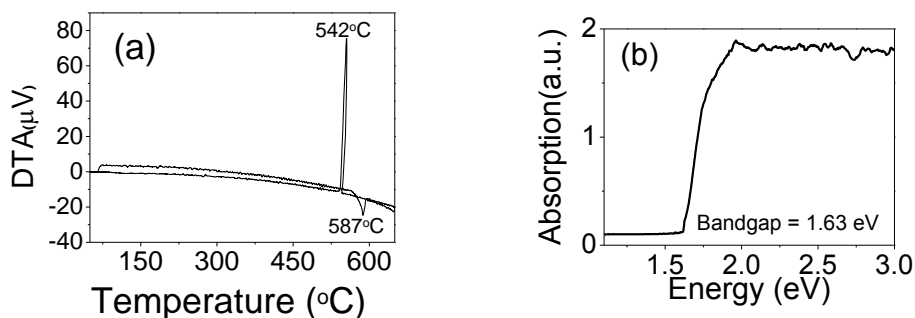


**Figure 5.** (a) The DTA curve of the synthesized  $\text{Cs}_2\text{Hg}_6\text{S}_7$ . (b) Solid state electronic absorption spectrum of  $\text{Cs}_2\text{Hg}_6\text{S}_7$ .

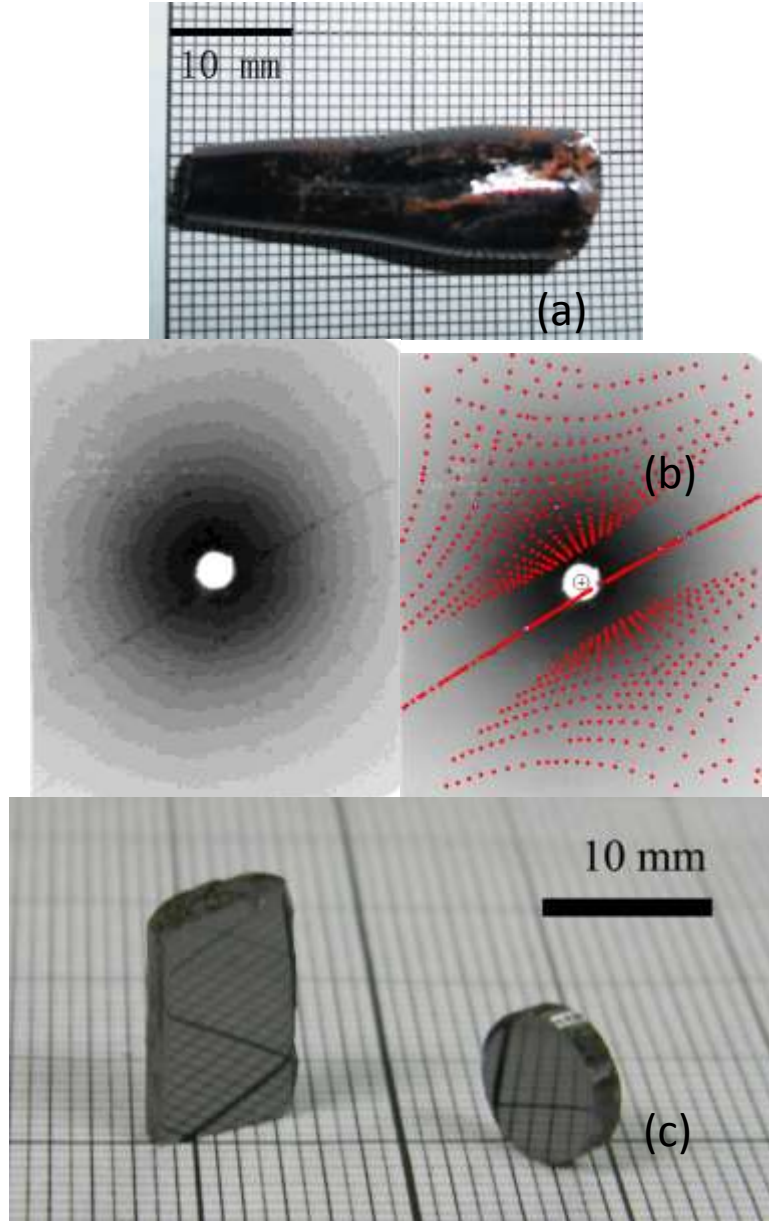


**Figure 6.** (a) As-grown  $\text{Cs}_2\text{Hg}_6\text{S}_7$  single crystal ingot (sample 2) with dimensions up to  $35 \times \Phi 11 \text{ mm}^3$ . (b) The Laue back reflection pattern recorded on a crystal cleaved parallel to the  $c$ -axis and oriented by OrientExpress program. (c) Typical crystals cut and polished. The crystal growth direction in the ingot is along the crystallographic  $c$ -axis.

Before the final Bridgman crystal growth run, two fast Bridgman growth runs (2-4 d for each) were used to further purify the raw  $\text{Cs}_2\text{Hg}_6\text{S}_7$  material. The top and bottom parts of the ingot were discarded to minimize impurities. After the growth procedure, several cm-sized ingots were obtained. One  $\text{Cs}_2\text{Hg}_6\text{S}_7$  crystal sample with dimensions of  $35 \times \Phi 11 \text{ mm}^3$  is shown in **Figure 6**. X-ray Laue back-reflection experiments were used to determine the single crystalline nature and to allow orientation of the samples. **Figure 6** shows a Laue back-reflection X-ray diffraction pattern from a  $\text{Cs}_2\text{Hg}_6\text{S}_7$  sample with a natural cleaved surface ( $//c$ -axis) taken from a Bridgman-grown ingot, confirming that the sample is a single crystal.

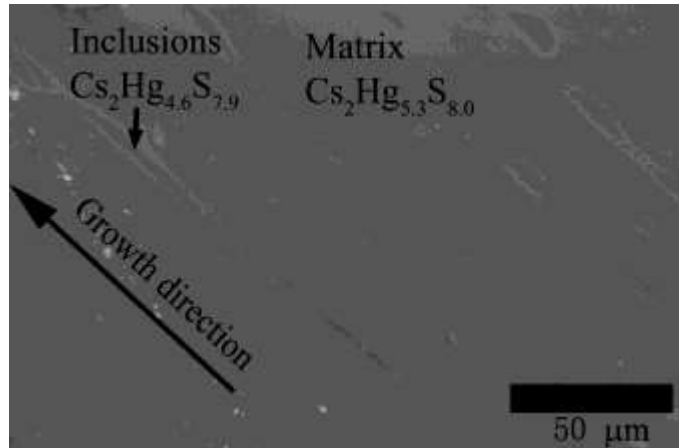


**Figure 7.** Scanning electron micrograph of the inclusions in  $\text{Cs}_2\text{Hg}_6\text{S}_7$  crystal.

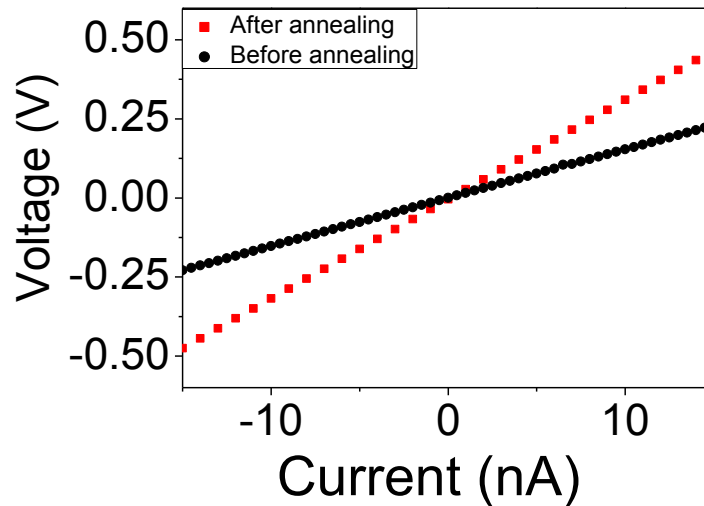


**Figure 8.** Current-voltage characteristics of a  $\text{Cs}_2\text{Hg}_6\text{S}_7$  crystal (sample 4) before and after annealing.

### 1.3. Microscopic defects, annealing effects, and resistivity of $\text{Cs}_2\text{Hg}_6\text{S}_7$

The Bridgman grown crystals of  $\text{Cs}_2\text{Hg}_6\text{S}_7$  were examined with respect to macro and microscopic defects. Microscopic defects in detector materials such as silicon, CZT, etc. have been studied for decades and there are numerous reports on their basic properties and effects on the performance of solid-state devices. For example, the growth of CZT is not straightforward. One problem is the solubility of tellurium in CZT wherein the melt essentially is “supersaturated” with Te at the growth temperature, and this excess Te precipitates as the solid ingot cools. The tellurium-rich regions have been shown to significantly degrade the materials’ performance. To further examine the quality of the  $\text{Cs}_2\text{Hg}_6\text{S}_7$  crystals, SEM was performed on a sample cleaved from the as-grown ingot with relatively large natural faces; the sample was not polished further or etched. The optical micrograph of the surface show inclusions with dimensions ranging from 5-50  $\mu\text{m}$  in size; most of them are in rod-shaped and are oriented parallel to the growth direction, see **Figure 6**. EDS analysis on these inclusions shows an average composition of  $\text{Cs}_2\text{Hg}_{4.6}\text{S}_{7.9}$ , which is different from the average composition

of the matrix “Cs<sub>2</sub>Hg<sub>5.3</sub>S<sub>8.0</sub>”. This indicates that the inclusions are Hg-deficient and this could result from the high vapor pressure of Hg at the growth temperature leading to loss of Hg.

Thermal annealing is a commonly used processing method to improve the quality of semiconductor crystals (e.g., CuInS<sub>2</sub>, HgCdTe and CdTe) by reducing defects such as dislocations, vacancies, anti-site, etc. This can raise the electrical resistivity which is desirable to suppress dark current. Crystals of Cs<sub>2</sub>Hg<sub>6</sub>S<sub>7</sub> were annealed under vacuum at 280°C for 1.5 d. The current-voltage characteristics of sample 4 (with 1% excess of Cs<sub>2</sub>S<sub>7</sub> and 2% excess of S) both before and after annealing, measured parallel to the *c*-axis, are shown in **Figure 8**. The resistivity values of Cs<sub>2</sub>Hg<sub>6</sub>S<sub>7</sub> crystals increase noticeably after annealing, the resistivity of sample 4 increases from 1.3 MΩ.cm to 3.5 MΩ.cm. The resistivity values along the *c*-axis of the different samples are summarized in **Table 1**.

Comparing the resistivity of different crystals, sample 2 (with 5 at% excess S) shows the highest value followed by sample 1 (without any excess of Cs<sub>2</sub>S<sub>7</sub> or S) shows the next highest value. Initially, it was thought that S was the most volatile element in the growth process of Cs<sub>2</sub>Hg<sub>6</sub>S<sub>7</sub>, hence the addition of excess S was expected to help compensate the loss during growth. However, it turned out that Hg is deficient in the final crystals. Concurrent with the finding that the growth run containing 5 at% excess S gave the best resistivity, we speculate that the excess S may help create a higher pressure atmosphere in the sealed tube, reducing volatilization from the melt and overall providing better conditions for crystal growth. Additional annealing work is necessary aimed at investigating a broader set of experimental conditions to further raise the resistivity of Cs<sub>2</sub>Hg<sub>6</sub>S<sub>7</sub> crystals.

#### 1.4. Spectroscopic, photoelectric characterization and figure of merit $\mu\tau$ product

Analysis of the photoluminescent behavior of Cs<sub>2</sub>Hg<sub>6</sub>S<sub>7</sub> is useful in providing information about electronically active impurity and defect centers. **Figure 9** shows the PL spectrum measured at 24K on two plate crystals cut (*// c*-axis and  $\perp$  *c*-axis) from sample 1. A broad peak around 1.65 eV is observed in both spectra. A small peak centered at 1.74 eV is seen from the sample cut  $\perp$  *c*-axis and it does not show up in the sample cut *// c*-axis; this may be a result of the anisotropic character of the Cs<sub>2</sub>Hg<sub>6</sub>S<sub>7</sub> crystal. The peak at 1.74 eV observed in the sample the sample cut  $\perp$  to the *c*-axis is attributed to the recombination of free excitons (conduction-to-valence band transitions), this is consistent with an energy bandgap of 1.73 eV observed from spectral photoconductivity measurements. In **Figure 9(a)**, the broad PL peak at 1.65 eV can be decomposed by a Gaussian function to reveal four peaks with energies of 1.57 eV, 1.62 eV, 1.66 eV, and 1.68 eV.

To determine the  $\mu\tau$  products for both holes and electrons we performed photoconductivity measurements on suitably cut as-grown Cs<sub>2</sub>Hg<sub>6</sub>S<sub>7</sub> crystals. Different voltage polarities were applied to the illuminated electrode. For strongly absorbed light, the photocurrent can be modeled by:

$$I(V) = \frac{I_0 \mu\tau V}{L^2} \frac{\left( 1 - e^{\frac{-L^2}{\mu\tau V}} \right)}{1 + \frac{L}{V} \frac{s}{\mu}} \quad (1)$$

where  $I_0$  is saturation current,  $L$  is the sample thickness,  $s$  is the surface recombination velocity, and  $V$  is the applied voltage. The electron and hole photoconductivity curves for sample 1 are shown in **Figure 10**. Using fits of the data to formula (1), the  $\mu\tau$  values were obtained for electrons and holes of all samples and are summarized in **Table 2**. Since sample 3 degraded in air, there was no good response during measurement. The samples which show higher resistivity give higher  $\mu\tau$  values presumably because a reduced number of structural defects giving correspondingly longer carrier lifetimes. The  $\mu\tau$  products for the  $\text{Cs}_2\text{Hg}_6\text{S}_7$  samples, especially sample 2 (  $(\mu\tau)_e = 1.10 \times 10^{-3} \text{cm}^2\text{V}^{-1}$ ,  $(\mu\tau)_h = 1.01 \times 10^{-4} \text{cm}^2\text{V}^{-1}$  ), are comparable to commercial CZT (  $(\mu\tau)_e = 4 \times 10^{-3} \text{cm}^2\text{V}^{-1}$ ,  $(\mu\tau)_h = 1.2 \times 10^{-4} \text{cm}^2\text{V}^{-1}$  ) and much higher than other detector-grade crystals such as  $\text{HgI}_2$  (  $(\mu\tau)_e = 3 \times 10^{-4} \text{cm}^2\text{V}^{-1}$ ,  $(\mu\tau)_h = 4 \times 10^{-5} \text{cm}^2\text{V}^{-1}$  ) and  $\text{TlBr}$  (  $(\mu\tau)_e = 5 \times 10^{-4} \text{cm}^2\text{V}^{-1}$ ,  $(\mu\tau)_h = 2 \times 10^{-6} \text{cm}^2\text{V}^{-1}$  ).

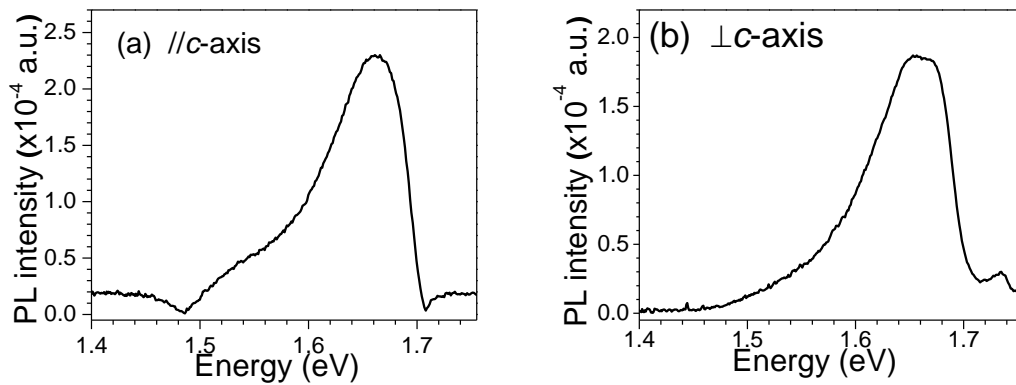


**Figure 9.** Photoluminescence spectra of  $\text{Cs}_2\text{Hg}_6\text{S}_7$  (sample 1) near the band edge at 24K, (a) //  $c$ -axis cut, (b)  $\perp c$ -axis cut.

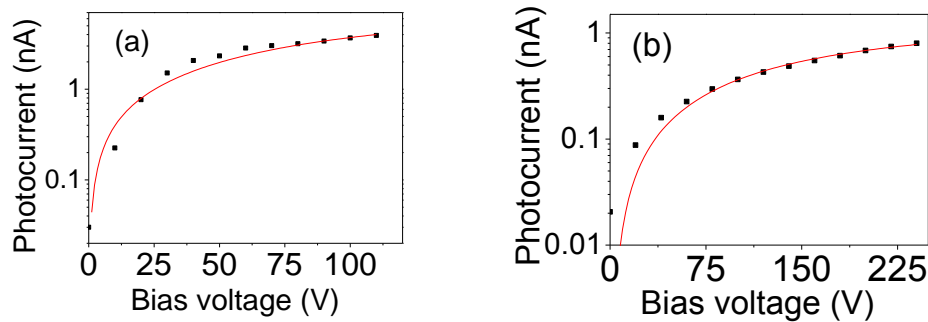


**Figure 10.** Photocurrent versus applied voltage (a) for electrons (b) for holes, measured on a  $\text{Cs}_2\text{Hg}_6\text{S}_7$  plate cut from sample 1.

### 1.5. Thermal expansion coefficient and thermal conductivity

Thermal properties should be considered in the crystal growth process, since thermal stresses in the crystal can induce dislocations or cracks during growth and cooling. For this reason it is necessary to measure the thermal expansion and thermal conductivity. The thermal expansion was assessed with variable temperature lattice constant determination using X-ray diffraction in the range of 100-400 K. **Figure 11** shows the thermal expansion curves, respectively. The linear thermal expansion coefficient is defined as:

$$\alpha_i = \frac{1}{L_i} \cdot \frac{\Delta L_i}{\Delta T} \quad (2)$$

Where  $L_i$  is the unit cell dimension along the  $i$ -axis. The volumetric thermal expansion coefficient is defined as:

$$\beta = \frac{1}{V} \frac{\Delta V}{\Delta T} \quad (3)$$

where  $V$  is the unit cell volume.

The average thermal expansion coefficients of  $\text{Cs}_2\text{Hg}_6\text{S}_7$  along the  $a$  and  $c$  – axes are  $\alpha_a = 2.168 \times 10^{-5} \text{K}^{-1}$  and  $\alpha_c = 1.282 \times 10^{-5} \text{K}^{-1}$ , respectively, in the temperature range of 100-400K. Apparently, the thermal expansion coefficients of  $\text{Cs}_2\text{Hg}_6\text{S}_7$  are anisotropic, but the difference between  $\alpha_a$  and  $\alpha_c$  is not large. The volumetric thermal expansion coefficient of  $\text{Cs}_2\text{Hg}_6\text{S}_7$  is  $\beta = 5.663 \times 10^{-5} \text{K}^{-1}$ , which is moderate. These values suggest that  $\text{Cs}_2\text{Hg}_6\text{S}_7$  can sustain relatively high thermal shock during crystal growth and annealing.

The thermal conductivity of  $\text{Cs}_2\text{Hg}_6\text{S}_7$  was determined using the flash thermal diffusivity method. The samples were coated with a thin layer of graphite to minimize errors on the emissivity of the material. The thermal conductivity was calculated from  $k = D C_p \rho$ , where  $D$  is the thermal diffusivity coefficient,  $C_p$  is the specific heat capacity which was indirectly derived using a standard sample (Pyrocera 9606) in the range of 300-575K, and the density  $\rho$  of the sample was determined using the sample dimensions and mass. The experimental density  $\rho$  is  $6.896 \text{ g/cm}^3$ , which matches well the calculated value of  $6.94 \text{ g/cm}^3$ . **Figure 12** shows the thermal conductivity of  $\text{Cs}_2\text{Hg}_6\text{S}_7$  parallel and perpendicular to the  $c$ -axis (crystal growth direction).

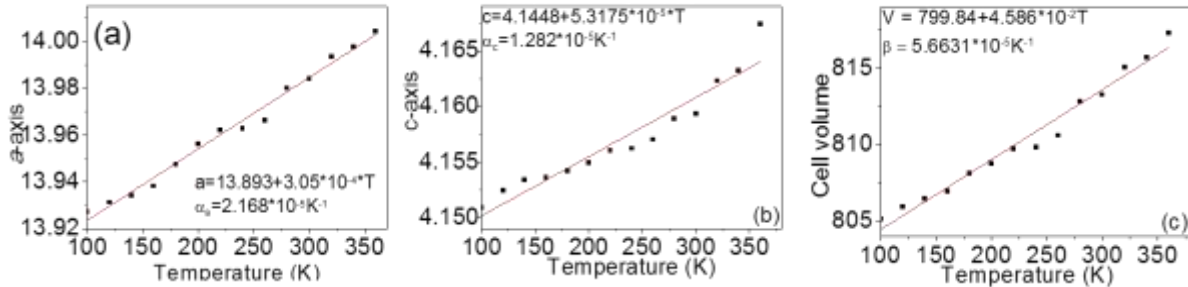


**Figure 11.** Temperature variation of the lattice parameters and cell volume for  $\text{Cs}_2\text{Hg}_6\text{S}_7$  from 100K to 400K. (a)  $a$ -axis; (b)  $c$ -axis; (c) cell volume.

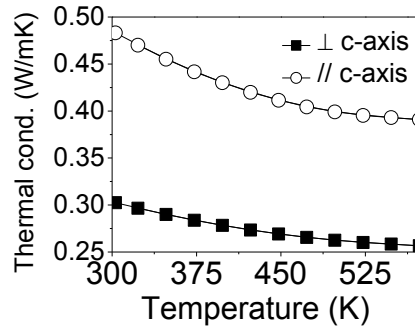


**Figure 12.** Variable-temperature total thermal conductivity for oriented  $\text{Cs}_2\text{Hg}_6\text{S}_7$  plates. Because of high resistivity of  $\text{Cs}_2\text{Hg}_6\text{S}_7$  crystals, the electronic component  $\kappa_{el}$  to the thermal conductivity is negligible.

The thermal conductivity exhibits a significant anisotropic character as the room temperature value measured //  $c$ -axis of 0.48 W/mK is almost twice of that obtained along the direction  $\perp c$ -axis of 0.30 W/mK. This is likely the result of the highly anisotropic crystal structure of  $\text{Cs}_2\text{Hg}_6\text{S}_7$ . The room temperature lattice thermal conductivity of the compound is extremely low.

In conclusion of this section, Large scale synthesis of  $\text{Cs}_2\text{Hg}_6\text{S}_7$  was achieved using  $\text{Cs}_2\text{S}_7$  and Hg as starting materials. Cm-scale crystals have been grown with the Bridgman method. The samples grown with excess S show the highest resistivity and mobility-lifetime ( $\mu\tau$ ) products. We presume that excess S increases the pressure in the sealed tube, which provides better conditions for crystal growth. Hg-deficient inclusions have been observed by SEM and a simple annealing procedure leads to improvement of the resistivity. Weak SHG was detected, but  $\text{Cs}_2\text{Hg}_6\text{S}_7$  can generate continuously tunable, doubled frequency light from the visible to near IR regions. The thermal expansion coefficients of  $\text{Cs}_2\text{Hg}_6\text{S}_7$  along the  $a$ - and  $c$ - axis are relatively small, and the thermal conductivity is low at 0.48 W/mK and 0.3 W/mK parallel and perpendicular to the  $c$ -axis respectively. In comparison with the other leading  $\gamma$ -ray detector crystals, the  $\mu\tau$  products for the  $\text{Cs}_2\text{Hg}_6\text{S}_7$  samples match those of CZT and are much higher than in  $\text{HgI}_2$  and  $\text{TlBr}$ . In the future, growth of crystals with dimensions  $\geq \Phi 20\text{mm}$  is feasible, and further improvements in the synthesis and crystal growth of  $\text{Cs}_2\text{Hg}_6\text{S}_7$  could promote this promising material to levels appropriate for  $\gamma$ -ray applications. More work is underway to optimize the crystal growth and annealing conditions in order to continue improvements in  $\text{Cs}_2\text{Hg}_6\text{S}_7$  crystal quality.

Using first-principles calculations, we investigated the electronic and thermodynamic properties of possible intrinsic defects of the newly proposed  $\gamma$ -ray detector material,  $\text{Cs}_2\text{Hg}_6\text{S}_7$ . Furthermore, we examined the concentration of the defects and the carrier density as a function of chemical environment to predict the optimal growth condition for reducing the concentration of defects as well as the carrier density which can lower detector efficiency. We found that S-vacancy and HgCs-antisite defects provide deep levels and Cs-vacancy forms a shallow acceptor level. We predict that the net carrier density can be reduced by controlling the partial pressure of Cs. This work is still ongoing.

Further research is needed to optimize and achieve high sensitivity detectors. In particular, we will be growing thicker and higher density samples for more efficient absorption of X-rays and  $\gamma$ -rays. Furthermore low-temperature photoluminescence and photocurrent mapping measurements will be performed to determine the nature of radiative and non-radiative defects, which may limit detector sensitivity. Near field scanning optical microscopy will be used to determine compositional inhomogeneity at the nanoscale. Detector response of selected materials will be measured at x-ray and gamma ray energies.

### **1.6. Synthesis of $\text{Cs}_2\text{Cd}_3\text{Te}_4$**

**$\text{Cs}_2\text{Cd}_3\text{Te}_4$ :** Large single crystals of  $\text{Cs}_2\text{Cd}_3\text{Te}_4$  were synthesized from the reaction of  $\text{Cs}_2\text{Te}_3$ , Cd, Te in the ratio 1:3:1 at 600 C. The  $\text{Cs}_2\text{Te}_3$  reactive flux was synthesized from stoichiometric mixtures of the elements in liquid ammonia. Yellow plates of  $\text{Cs}_2\text{Cd}_3\text{Te}_4$  formed from the reaction (Figure 1b). Attempts to grow large crystals via the Bridgman method using carbon



coated silica tubes failed due to severe attack of the tubes by Cs and Cd vapor. The use of carbon and glassy carbon tubes was also not successful because the crystals stick on the crucible walls and can only be removed mechanically thus crushing the bulk volume of the crystal. Currently we are using boron nitride crucibles which we expected to solve both problems.

**Physical properties.** Diffuse reflectance spectroscopy on pulverized parts of the single crystalline ingots was consistent in yielding band gaps  $\sim 1.6$  eV and 2.5 eV for  $\text{Cs}_2\text{Hg}_6\text{S}_7$  and  $\text{Cs}_2\text{Cd}_3\text{Te}_4$ , respectively, **Figure 13**. Photoluminescence measurements performed independently on high quality single crystals gave comparable results with the values obtained by diffuse reflectance spectroscopy. The electrical resistivity was found to be sensitive on the synthesis processes. Low quality crystals show a resistivity of a few hundred  $\text{k}\Omega\cdot\text{cm}$ . Improvements in purification of the reaction starting materials, and optimization of crystal growth has resulted in resistivity  $\sim 2\text{M}\Omega\cdot\text{cm}$  in the direction of the growth and  $\sim 5\text{M}\Omega\cdot\text{cm}$  perpendicular to the growth direction for  $\text{Cs}_2\text{Hg}_6\text{S}_7$  and  $\sim 1\text{M}\Omega\cdot\text{cm}$  in the direction of the growth and  $\sim 2\text{M}\Omega\cdot\text{cm}$  perpendicular to the growth direction for  $\text{Cs}_2\text{Cd}_3\text{Te}_4$ .

Since typical 4 probe method may give erroneous results in highly resistive specimens, we have developed a 2-probe electrical conductivity method with the use of an electrometer. In the set up that we have developed source voltages  $\pm 100\text{V}$  and detection currents of  $0.1\text{pA}$  under dark conditions allow the measurement of resistivity values  $\sim 1\text{T}\Omega$ . The setup was fully computerized with software that we have developed and takes into account electric field relaxation processes at high source voltages.

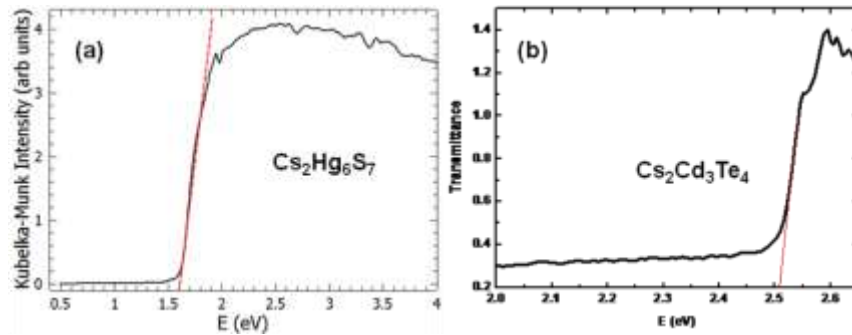


**Figure 13.** Diffuse reflectance measurement on  $\text{Cs}_2\text{Hg}_6\text{S}_7$  and  $\text{Cs}_2\text{Cd}_3\text{Te}_4$  crystal.

### 1.7. Optical and Electrical measurements ( $\mu\cdot\tau$ determination) of $\text{Cs}_2\text{Cd}_3\text{Te}_4$

**Optical characterization and measurement of absorption coefficient for the determination of bandgap.** Semiconductor bandgaps were determined by measuring the transmission and reflection spectra using a UV-VIS spectrometer in the wavelength range of 300 - 1500 nm. In the transmission configuration, the transmittance  $T$ , the reflectance  $R$ , and absorption coefficient  $\alpha$  are given by:

$$T = \frac{(1 - R^2)e^{-\alpha d}}{1 - R^2e^{-\alpha d}} ; \left( \alpha = \frac{1}{d} \ln \left[ \frac{(1 - R^2)}{2T} + \sqrt{\left( \frac{(1 - R)}{2} \right)^4 + (4T^2)} + R^2 \right] \right)$$

where  $d$  is the thickness of the sample. The unit of absorption coefficient is  $\text{cm}^{-1}$ . For bulk semiconductors we assume that  $\alpha d \gg 1$ , and thus  $T = (1 - R)^2 e^{-\alpha d}$  and  $(= (2 \ln(1 - R))/d - \ln T/d)$ . The spectrometer has a limited sensitivity for small values of the transmittance  $T$ . Therefore, for thick and strongly absorbing materials it is difficult to obtain reliable absorption data for wavelengths above the bandgap. Nevertheless, the estimation of bandgap is possible since it depends on the sharp transition between low and high absorption. The variation of absorption coefficient,  $\alpha$  was determined for the case of allowed direct ( $\alpha^2$ ) and indirect ( $\alpha^{1/2}$ ) optical transitions.

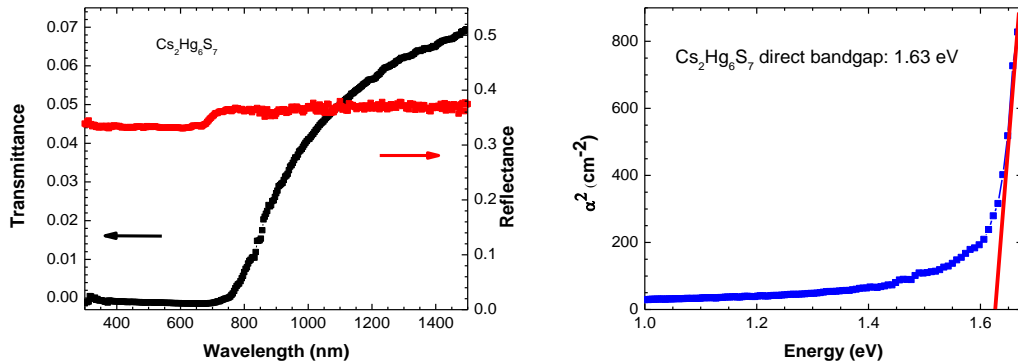


**Figure 14.** (a) Spectral distribution of transmittance and reflectance for  $\text{Cs}_2\text{Hg}_6\text{S}_7$  in the wavelength range of 300 - 500 nm (b) Dependence of the square of absorption coefficient ( $\alpha^2$ ) on photon energy for  $\text{Cs}_2\text{Hg}_6\text{S}_7$ .

**Figure 14** shows the transmission and reflection spectra, as well as the allowed direct gap optical transition in the case of  $\text{Cs}_2\text{Hg}_6\text{S}_7$ . Extrapolating the linear part of the  $\alpha^2$  curve towards lower photon energies and finding the point of interception with the energy axis gives the corresponding direct energy bandgap. The bandgap energy is 1.63 eV. Similarly the direct optical bandgap of  $\text{Cs}_2\text{Cd}_3\text{Te}_4$  was determined to be 2.45 eV.

### 1.8. Photoconductivity studies

Photoconductivity measurements were conducted on  $\text{Cs}_2\text{Hg}_6\text{S}_7$ , and  $\text{Cs}_2\text{Cd}_3\text{Te}_4$ .  $\text{Cd}_{0.9}\text{Zn}_{0.1}\text{Te}$  was used as a reference and calibration sample for comparison. The thickness of the CZT sample was 2 mm while those of  $\text{Cs}_2\text{Hg}_6\text{S}_7$ , and  $\text{Cs}_2\text{Cd}_3\text{Te}_4$  were 2 mm and 850  $\mu\text{m}$  respectively. The steady-state (DC) photocurrent technique gives information about transport parameters such as the mobility-lifetime product  $\mu\tau$  and the surface recombination velocity. It also plays a complementary role with respect to high-energy photon spectroscopy and provides an evaluation of the surface quality of samples. In addition, transient photoconductivity measurements enable the determination of carrier lifetimes in these materials.

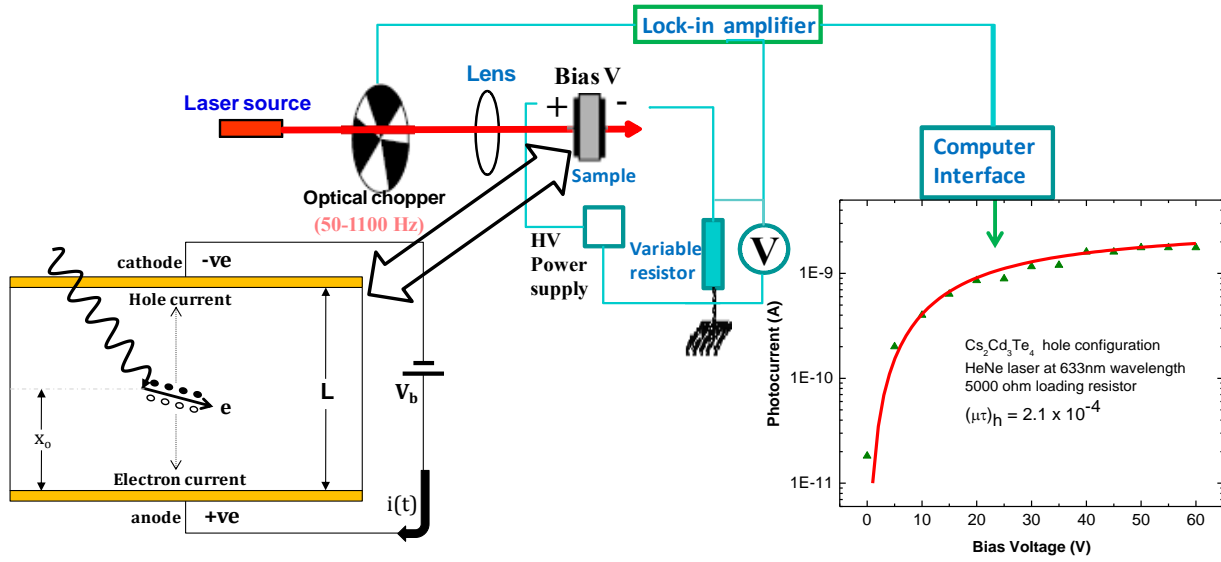


**Figure 15.** DC photoconductivity setup for a planar detector. The plot shows the hole photocurrent response of  $\text{Cs}_2\text{Cd}_3\text{Te}_4$ .

The setup for the photoconductivity measurement (**Figure 15**) consists of a He-Ne laser light source (633 nm) suitably filtered and focused with a lens, a chopper signal that is operating at 200 Hz, a high voltage power supply, and a lock-in amplifier that is used to reduce noise and remove the dark current contribution. Gold electrodes of  $\sim 80$  nm thick were evaporated on the front and back surfaces of the sample. For the photocurrent measurement, the light was focused onto the metal contact. Transparency of the gold contacts ensured that sufficient incident radiation reached the detector surface. Ionizing radiation that is absorbed in the volume of the detector generates electron-hole pairs in direct proportion to the energy deposited. Applying an electric field across the detector subsequently causes the carriers to drift towards the appropriate electrode (**Figure 15**). Electron and hole photocurrents can be measured separately by changing the bias direction, and the corresponding  $\mu\tau$  product can be obtained, respectively.

**Table 2** Summary of detector parameters measured

Sample	$E_g$ (eV)	$\tau_e$ (s)	$\tau_h$ (s)	$(\mu\tau)_e$ $\text{cm}^2/\text{V}$	$(s/\mu)_e$ $\text{V}/\text{cm}$	$(\mu\tau)_h$ $\text{cm}^2/\text{V}$	$(s/\mu)_h$ $\text{V}/\text{cm}$
$\text{Cs}_2\text{Hg}_6\text{S}_7$	1.63	$1.35 \times 10^{-3}$	$1.79 \times 10^{-3}$	$1.92 \times 10^{-3}$	$0.44 \times 10^2$	$3.42 \times 10^{-4}$	$1.18 \times 10^2$
$\text{Cs}_2\text{Cd}_3\text{Te}_4$	2.45	$0.64 \times 10^{-3}$	$0.47 \times 10^{-3}$	$7.8 \times 10^{-4}$	N/A	$2.1 \times 10^{-4}$	N/A
$\text{Cd}_{0.9}\text{Zn}_{0.1}\text{Te}$	1.56	$9.9 \times 10^{-6}$	$1.2 \times 10^{-5}$	$6.6 \times 10^{-4}$	$0.74 \times 10^2$	$3.1 \times 10^{-4}$	$0.125 \times 10^2$

From the current dependence on voltage under illumination fit to eq (1),  $\mu\tau$  and the carrier surface recombination ( $s/\mu$ ) were obtained for several detector materials (**Table 2**). It is to be

noted that the above equation makes the following assumptions: (i) the electric field and the transport properties are constant within the sample volume. (ii) The material properties are not modified by the electric field.

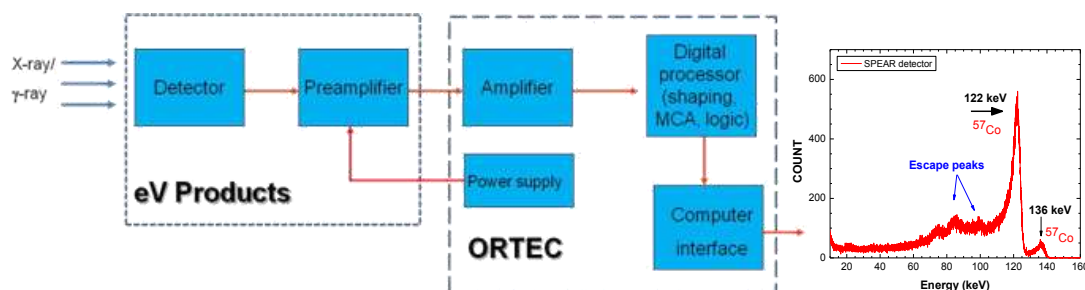
The data for the CZT calibration sample for a 633 nm excitation compares favorably with that reported in the literature for 650 nm excitation. It is to be noted that the surface recombination plays an important role as the light excitation wavelength decreases to 800 nm and lower. The shorter wavelengths have less penetration into the sample, and hence, surface recombination is higher and surface recombination velocities are larger. In addition, it has also been reported that a detector material without chemical etching is difficult to saturate. The E-field of a chemically treated surface is much smaller than the untreated sample. Thus a polished surface without etching has a larger surface recombination velocity. However, the  $\mu\tau$  values are fairly independent of the surface conditions at longer wavelengths (below band gap). We are currently investigating treatment options for our detector materials.

## 2.0. Design of X-ray detector and spectrometer system.

We have built up an x-ray and gamma ray spectrometer system for characterizing high Z chalcogenide materials. A schematic of the x-ray/  $\gamma$ -ray radiation detection system is shown in **Figure 16**. It includes a detector, preamplifier, amplifier, digital processor (shaping, MCA, logic), computer interface and power supplies of the minibin from eV Products and ORTEC. A calibration run of the spectrometer system was done on a CZT detector using  $^{57}\text{Co}$  X-ray source. The spectral response of the system to  $^{57}\text{Co}$  source is shown in Figure 6 with a 5 mm thick CZT detector.

## 2.1. Comparison of our materials to other detector materials reported in the literature

The measured optical, electrical, and detector parameters of our materials compares very well with that of other materials reported in the literature [A. Burger et. al., *J. Electron Mat.* **32**, 756 (2003)]. Specifically, the mobility-lifetime products for  $\text{Cs}_2\text{Hg}_6\text{S}_7$  are better than that reported for  $\text{PbI}_2$  and  $\text{HgI}_2$ . The resolution of the spectrometer system for CZT also compares favorably with that reported in the literature, indicating that our gamma ray spectrometer system can be used for high resolution measurements of other chalcogenide materials.



**Figure**

**16.** Schematic of x-ray and  $\gamma$ -ray radiation detection system and spectral response of the system to  $^{57}\text{Co}$  source with CZT detector.

## 2.2. Theoretical investigation of Hg-based chalcogenides for $\gamma$ -ray detector candidates

The theoretical investigation aid in materials pre-screening and selection ahead of actual synthesis and crystal growth experiments which are costly and time consuming. We perform “exploratory theory” to identify materials that meet the basic criteria for  $\gamma$ -ray detection. In this context we investigated electronic structures of mainly Hg-based chalcogenides for  $\gamma$ -ray detector candidates using the highly precise full-potential linearized augmented plane-wave (FLAPW) method.

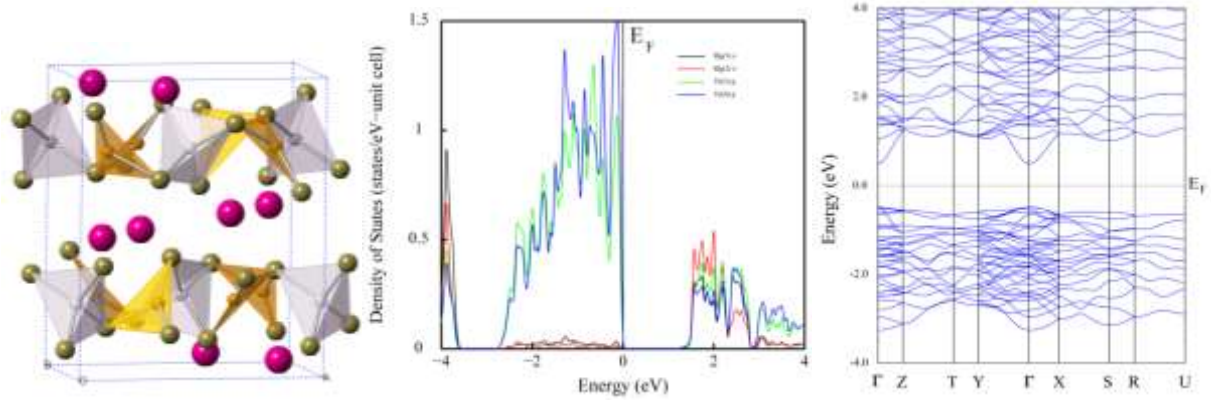


**Figure 17.** Crystal structure, density of states, and band structure of  $\text{Rb}_2\text{Hg}_3\text{Te}_4$ .

First-principles calculations show that Hg-based chalcogenides can be good candidates in terms of density, band gap, and band dispersions of the conduction and valence bands. One of the common characteristics of Hg-based chalcogenides is that their conduction band edges always show very dispersive bands due to the significant contribution of Hg-s states, which indicates they have advantages of small  $n$ -type effective masses for high mobilities.

As representative examples of Hg-based chalcogenides, we report here theoretical results of  $\text{Rb}_2\text{Hg}_3\text{Te}_4$ ,  $\text{HgGa}_2\text{Se}_4$  and  $\text{HgIn}_2\text{S}_4$ . They all show large dispersion in the conduction band minimum (CBM), but dispersive and flat bands together in valence band maximum (VBM). In  $\text{Rb}_2\text{Hg}_3\text{Te}_4$ , there are two different Hg types in the crystal structure. The first type of Hg (orange in **Figure 17**) has 8 trigonal sites in the unit cell and the second type of Hg has 4 tetrahedral sites. The projected density of states (PDOS) in **Figure 17** also shows the difference of local geometries of Hg sites in  $\text{Rb}_2\text{Hg}_3\text{Te}_4$ . Especially, the second type of Hg has a larger contribution to the CBM, due to possibly more bonds with Te atoms. The density of  $\text{Rb}_2\text{Hg}_3\text{Te}_4$  is  $6.6 \text{ g/cm}^3$ , which is good for  $\gamma$ -ray detectors. The FLAPW calculations with the local density approximation (LDA) yield an indirect band gap, 0.98 eV, and, for the accurate band gap of  $\text{Rb}_2\text{Hg}_3\text{Te}_4$ , we plan to apply the non-local screened-exchange LDA method (sX-LDA).

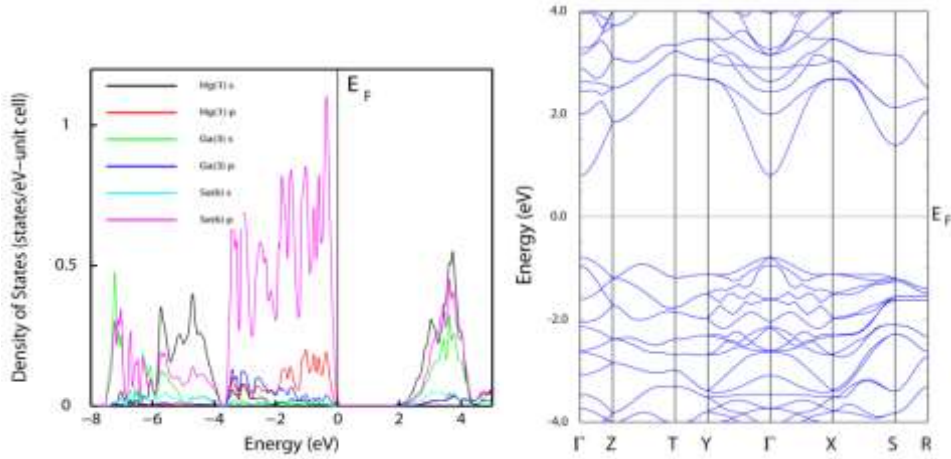
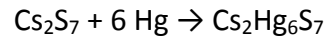
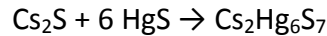


**Figure 18.** Projected density of states, and band structure of  $\text{HgGa}_2\text{Se}_4$ .

For  $\text{HgGa}_2\text{Se}_4$ , we obtained an accurate band gap with the  $\text{X-LDA}$  method, which is direct and 1.63 eV while the LDA band gap is only 0.67 eV. This is within optimal range of the band gap for  $\gamma$ -ray detector candidates. The density of  $\text{HgGa}_2\text{Se}_4$  is slightly smaller than that of  $\text{Rb}_2\text{Hg}_3\text{Te}_4$ , 6.21 g/cm<sup>3</sup>. Again, due to Hg  $s$ -states in the CBM (see PDOS in **Figure 18**), the band structure of  $\text{HgGa}_2\text{Se}_4$  shows also very dispersive bands, and thus small effective masses for  $n$ -type. Its valence band edges also appear to be better (more dispersive) than those of  $\text{Rb}_2\text{Hg}_3\text{Te}_4$ . Both  $\text{HgGa}_2\text{Se}_4$  and  $\text{Rb}_2\text{Hg}_3\text{Te}_4$  are attractive for experimental crystal growth studies.

### **3.0. Further work on $\text{Cs}_2\text{Hg}_6\text{S}_7$ done in the last year of this five years project.**

Because of the promising results on  $\text{Cs}_2\text{Hg}_6\text{S}_7$  presented above, we paid additional attention to this material in order to understand it at a deeper level and to further improve its properties with regard to hard radiation detection. As described above initially (the first year or two of this grant) we synthesized  $\text{Cs}_2\text{Hg}_6\text{S}_7$  using the following reactions:



Though large quantity of raw material for crystal growth can be obtained using reaction (2), the resistivity of the as grown crystals is in the range of 0.8 -  $8.3 \times 10^6 \Omega\cdot\text{cm}$ , which is too low for practical X-ray and  $\gamma$ -ray detection applications. Later we employed a new method to synthesize  $\text{Cs}_2\text{Hg}_6\text{S}_7$  raw material with higher purity for crystal growth and obtained specimens with resistivity of the order of  $10^8 \Omega\cdot\text{cm}$ .

The low energy native defects in  $\text{Cs}_2\text{Hg}_6\text{S}_7$  have been theoretically calculated by our theory collaborators (Freeman) using density functional calculations which suggested that the most stable ones are likely Cs and Hg vacancies. Based on this prediction we assumed the undoped samples are likely to be  $p$ -type. Under this premise and based on the experimental Seebeck

measurements which indicate *p*-type character for undoped stoichiometric samples, we chose to explore *n*-type dopants to compensate the majority carrier and realize high resistivity. In order to control the carrier concentration, *n*-type In/Cl doping was tried on Cs<sub>2</sub>Hg<sub>6</sub>S<sub>7</sub>. We also investigated the effects of Cd alloying in Cs<sub>2</sub>Hg<sub>6-x</sub>Cd<sub>x</sub>S<sub>7</sub> to understand how the properties vary with composition. We found that Ag X-ray detection can be realized using the HgCl<sub>2</sub> doped Cs<sub>2</sub>Hg<sub>6</sub>S<sub>7</sub> crystal.

### 3.1. Experimental section.

**Reagents** The high purity (i) Hg ( 99.9999%, Aldrich ) metal; (ii) Cs ( 99.9%, Aldrich ) metal; (iii) Indium metal ( 99.99%, Cerac, Milwaukee, WI ); (iv) Cadmium powder, ( 99.99%, Alfa Aesar ); (v) HgCl<sub>2</sub> ( 99.999%, Aldrich ) were used as received, (vi) Sulfur shot, ( 99.99%, 5N Plus Inc., St-Laurent, QC, Canada) was further purified by melting under vacuum. CdS was prepared by heating the mixture of Cd and S powder at 450 °C for three days, then ground and reacted for another time for complete reaction. HgS was synthesized by the method described previously<sup>1,13</sup> and ground prior to use. Cs<sub>2</sub>S was synthesized by a stoichiometric reaction in liquid ammonia.<sup>3,14,15</sup> All manipulations were conducted in a nitrogen filled glove box with O<sub>2</sub> and H<sub>2</sub>O levels below 0.1ppm.

**Cs<sub>2</sub>Hg<sub>6-x</sub>Cd<sub>x</sub>S<sub>7</sub>** Syntheses of Cs<sub>2</sub>Hg<sub>6-x</sub>Cd<sub>x</sub>S<sub>7</sub> ( *x* = 0.25, 0.5, 0.75, 1.0, 1.35, 2.0, 3.0, 4.0 ) were performed by direct reaction of a mixture of Cs<sub>2</sub>S, ( 6-*x* ) HgS, and *x* CdS; each sample with total amount around 500 mg was weighted and loaded into a fused silica tube and subsequently sealed under a 10<sup>-4</sup> mbar vacuum. The samples were put into tube furnaces, and heated from room temperature to 200 °C in 6h and kept at 200 °C for 8h, followed by heating to 620 °C in 12h, soaked there for 24h, then slowly cooled to 150 °C in 48 h. They were finally cooled to room temperature in 3h. The reactions of samples with *x* < 1 yielded black needle crystals of Cs<sub>2</sub>Hg<sub>6-x</sub>Cd<sub>x</sub>S<sub>7</sub> determined by EDS analysis; but for samples with *x* ≥ 1, in addition to black/dark red needles of Cs<sub>2</sub>Hg<sub>6-x</sub>Cd<sub>x</sub>S<sub>7</sub> crystals, there were red polyhedra and yellow plate-like crystals of Hg<sub>1-y</sub>Cd<sub>y</sub>S (red) and Cs<sub>2</sub>Hg<sub>3-z</sub>Cd<sub>z</sub>S<sub>4</sub> (yellow) phases respectively determined by EDS analysis. For samples with *x* > 2, most of the products are yellow and red phases. All the EDS data are summarized in **Table 3**. Black/dark red needle crystals from reactions with *x* < 2 were handpicked for single crystal X-ray diffraction.

**Table 3.** The atomic ratio values of Cs<sub>2</sub>Hg<sub>6-x</sub>Cd<sub>x</sub>S<sub>7</sub> samples (*x* = 0.25, 0.5, 0.75, 1.0, 1.35, 2, 3, 4) measured by SEM-EDS.

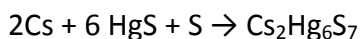
Elements	S(at%)	Cd(at%)	Cs(at%)	Hg(at%)	Experimental <i>x</i> values (When total number of Cd and Hg atoms = 6)	Average <i>x</i> value
sample 1 <i>x</i> =0.25	52.24335	0.282012	12.48309	34.99156	0.047970032	
	51.81487	0.444229	16.08285	31.65805	0.0830276	

		52.74967	0.276106	13.27457	33.69965	0.048759286	
		52.27602	0.403268	13.13895	34.18177	0.06996112	0.068549
		52.21656	0.525225	12.9512	34.30701	0.090472265	
		52.60228	0.326559	12.796	34.27516	0.056625846	
		51.81487	0.444229	16.08285	31.65805	0.0830276	
sample 2 x=0.5		52.08602	0.827294	11.66304	35.42365	0.136927839	
		51.6579	0.883963	12.43037	35.02777	0.14768928	
		51.90471	0.73936	12.8357	34.52024	0.12581418	
		51.86313	0.805151	13.02607	34.30565	0.137590227	0.145328
		52.55655	0.912793	12.88166	33.64899	0.158462865	
		52.91283	0.816468	13.07453	33.19617	0.144029017	
		52.82019	0.872714	12.80014	33.50695	0.152307512	
		51.27245	0.959814	12.69001	35.07773	0.159802409	
sample 3 x=0.75		52.74134	1.47794	12.69642	33.0843	0.256570176	
		52.74134	1.47794	12.69642	33.0843	0.256570176	
		52.65987	1.507828	12.977	32.8553	0.26327545	
		52.56814	1.586439	12.87989	32.96552	0.275487535	
		52.26493	1.506621	12.74688	33.48158	0.258364984	0.260054
		51.93881	1.329547	12.33354	34.3981	0.223280363	
		52.9296	1.645987	12.62794	32.79647	0.286736861	
		52.07786	1.648128	12.85691	33.41711	0.282010577	
		52.49615	1.362447	13.18407	32.95733	0.238191583	
sample 4 x=1.0		50.49464	2.408613	14.81202	32.28473	0.416554784	
		51.5592	2.320111	12.74966	33.37104	0.390031299	
		51.67809	2.332738	12.69239	33.29678	0.39283237	
		51.34947	2.439106	12.48845	33.72297	0.404695682	
		51.47483	2.454115	12.83652	33.23452	0.412587649	0.422545
		52.74257	2.57824	12.74657	31.93262	0.448248464	
		52.89166	2.160128	12.55746	32.39075	0.375121234	
		48.94675	2.323502	22.18451	26.54523	0.482910437	
		49.14406	2.310269	21.9727	26.57296	0.479919125	
sample 5 x=1.35		51.96757	3.490113	12.5059	32.03642	0.589437703	
		52.12397	3.185663	12.83886	31.85151	0.545534253	
		51.52463	3.720544	12.42972	32.32512	0.619305113	0.602124
		51.33074	3.388704	13.05623	32.22433	0.57092086	
		52.16997	3.989928	12.90318	30.93691	0.685420421	



sample 6 x=2	Cs <sub>2</sub> Hg <sub>3-y</sub> Cd <sub>y</sub> S <sub>4</sub>	50.45241	2.186717	19.63253	27.72834		
		50.81602	1.920035	19.00564	28.2583		
	Hg <sub>1-z</sub> Cd <sub>z</sub> S	51.44691	42.94452	0.205656	5.402908		
		51.47849	43.02058	0.162341	5.338583		
sample 7 x=3	Cs <sub>2</sub> Hg <sub>3-y</sub> Cd <sub>y</sub> S <sub>4</sub>	49.48634	1.977836	21.36971	27.16611		
		49.33762	2.198386	21.90692	26.55708		
		49.37362	2.230139	21.01614	27.3801		
	Hg <sub>1-z</sub> Cd <sub>z</sub> S	51.56449	44.55389	4.49E-02	3.836735		
		51.13931	45.6271	6.84E-02	3.165223		
sample 8 x=4	Cs <sub>2</sub> Hg <sub>3-y</sub> Cd <sub>y</sub> S <sub>4</sub>	49.42684	1.085954	21.44284	28.04437		
		49.33336	0.803704	21.3545	28.50843		
		48.9037	0.607424	22.70875	27.78012		
	Hg <sub>1-z</sub> Cd <sub>z</sub> S	51.59128	43.41001	0.26117	4.737543		
		51.73935	43.1731	0.343739	4.743814		
		51.95506	42.57869	0.383986	5.082272		

**Crystal growth of Cs<sub>2</sub>Hg<sub>6</sub>S<sub>7</sub>:** A new method referred to here as “vapor transport method” was adopted to synthesize polycrystalline Cs<sub>2</sub>Hg<sub>6</sub>S<sub>7</sub> for the purpose of using it as starting material for crystal growth. HgS and S powders were loaded into a 15mm silica tube first, and a 9mm short quartz crucible filled with stoichiometric amount of Cs metal was then inserted into the 15mm tube, and held in place by an indentation made in the middle of the wall of the larger tube. This setup is schematically shown in **Figure 19(a)**. The reaction scheme is



The tube was sealed under a vacuum of  $< 10^{-4}$  mbar, (the bottom part of the tube was cooled in liquid N<sub>2</sub> to prevent evaporation of Cs metal during sealing) and then placed vertically into a tube furnace. The furnace was heated to 90 °C first and soaked there for 48h and followed by cooling to room temperature. After this step, the Cs metal was evaporated and all reacted. Some white and yellow powder (Cs<sub>2</sub>S<sub>x</sub>) were condensed in the 9mm crucible and also on the inside wall of the 15mm tube. The 15mm tube was then transferred back in the glove box and opened on the top. All the white/yellow powder in the 9mm crucible was collected and loaded back into the 15mm tube. The 9mm crucible was removed. The 15mm tube was resealed under a vacuum of  $< 10^{-4}$  mbar and put back into the tube furnace. The furnace was heated to 620 °C in 12h, soaking there for 24h and cooled to room temperature in 10h. The obtained products inside the 15mm quartz were collected, mixed and sealed in another silica tube, and heated again to 620 °C for 24h to ensure complete reaction. The obtained polycrystalline ingot is shown in **Figure 19b**. The purity of the sample was confirmed by powder X-ray diffraction.

$\text{Cs}_2\text{Hg}_6\text{S}_7$  polycrystalline starting material was synthesized as described above for the different growth runs. One run was carried out to grow undoped- $\text{Cs}_2\text{Hg}_6\text{S}_7$ , one was with 5at% Cd alloying of  $\text{Cs}_2\text{Hg}_6\text{S}_7$  and two runs were with In- and Cl-doped (using  $\text{HgCl}_2$ )  $\text{Cs}_2\text{Hg}_6\text{S}_7$  respectively. The nominal doping concentration for In is  $1 \times 10^{19} \text{ cm}^{-3}$ , Cl is  $2 \times 10^{20} \text{ cm}^{-3}$ . For 5at% Cd alloying  $\text{Cs}_2\text{Hg}_6\text{S}_7$ :  $\text{Cs}_2\text{Hg}_6\text{S}_7$  polycrystalline powder (11.6 g, 6.84 mmol), CdS powder (0.312 g, 2.16 mmol) and  $\text{Cs}_2\text{S}$  (0.107 g, 0.36 mmol) were mixed, loaded and sealed into a 9mm quartz crucible with conical tip. In doped  $\text{Cs}_2\text{Hg}_6\text{S}_7$ :  $\text{Cs}_2\text{Hg}_6\text{S}_7$  polycrystalline powder (10.407 g, 6.14 mmol), In metal (0.0029 g, 0.02 mmol),  $\text{Cs}_2\text{S}$  (0.001 g, 0.004 mmol) and S (0.001 g, 0.02 mmol) were mixed, loaded and sealed into a 9mm quartz crucible with conical tip.  $\text{HgCl}_2$  doped  $\text{Cs}_2\text{Hg}_6\text{S}_7$ :  $\text{Cs}_2\text{Hg}_6\text{S}_7$  polycrystalline powder (10.88 g, 6.42 mmol),  $\text{HgCl}_2$  powder (0.071 g, 0.26 mmol) were mixed, loaded and sealed into a 9mm quartz crucible with conical tip in vacuum of  $< 1 \times 10^{-4} \text{ mbar}$ .

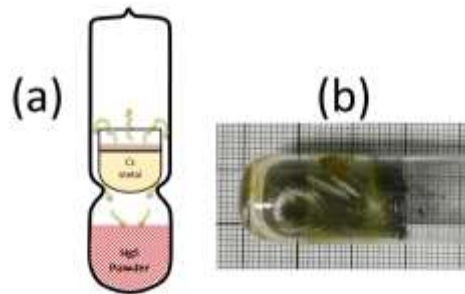


**Figure 19.** (a) The setup of the “vapor transport method” for synthesis of  $\text{Cs}_2\text{Hg}_6\text{S}_7$ ; (b) Synthesized polycrystalline  $\text{Cs}_2\text{Hg}_6\text{S}_7$  by the vapor transport method.

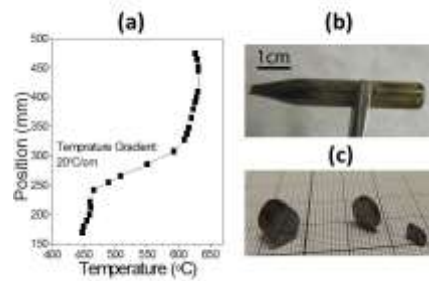


**Figure 20.** (a) Temperature profile of the utilized Bridgman furnace; (b) as grown undoped  $\text{Cs}_2\text{Hg}_6\text{S}_7$  ingot; (c) cut and polished crystal samples for further characterization.

In this work, the crystal growth parameters and the Bridgman furnace were improved. Two additional zones were added on the top and bottom part of the original two zone furnace, in order to obtain a more stable and homogeneous temperature. A homemade baffle was installed between the hot and cool zones to decrease the air flow disturbance, and to increase the temperature gradient. The optimized temperature profile is shown in **Figure 20(a)**, the

temperature gradient is  $\sim 20$  °C/cm. During several runs, the growth speed of  $\sim 1$ cm/day was deemed best for the crystal growth of  $\text{Cs}_2\text{Hg}_6\text{S}_7$ . After the growth was finished, the furnace cooled down to room temperature in one day. A typical undoped- $\text{Cs}_2\text{Hg}_6\text{S}_7$  ingot up to 5cm long is shown in **Figure 20(b)**. The crystal direction in the resulting ingots was determined by X-ray Laue back reflection experiments which indicated that the growth direction was along the *c*-axis. A Struers Accutom-50 saw was used to cut the  $\text{Cs}_2\text{Hg}_6\text{S}_7$  ingots into wafers ( $\phi 7\text{mm} \times 1.6\text{mm}$ ) and rectangular blocks (1.6mm thick) (**Figure 20(c)**), which were then polished using silicon carbide sandpaper with different grit sizes (from P600 to P12,000).

### 3.2. Crystallographic, optical, and electrical characterization of the crystals of $\text{Cs}_2\text{Hg}_6\text{S}_7$

Phase purity of the samples was checked by powder X-ray diffraction (PXRD) at room temperature using a calibrated CPS 120 INEL powder X-ray diffractometer (Cu  $K\alpha$  graphite monochromatized radiation) operating at 40 kV/20 mA and equipped with a position-sensitive detector with a  $2\theta$  range of 0-120°. In order to determine the cell parameters, the single crystal X-ray diffraction data for  $\text{Cs}_2\text{Hg}_{6-x}\text{Cd}_x\text{S}_7$  crystals were collected on a STOE Model IPDS II diffractometer, with graphite-monochromatized Mo  $K\alpha$  ( $\lambda = 0.71073$  Å) radiation operating at 50 kV and 40 mA.

Optical diffuse reflectance measurements were made at room temperature with a Shimadzu Model UV-3101PC double-beam, double-monochromator spectrophotometer operating at 200-2500 nm region. The optical transmission spectrum taken on single crystals of  $\text{Cs}_2\text{Hg}_6\text{S}_7$  was measured on a Lambda 1050 UV-vis-IR spectrophotometer in the range of 300-1500 nm.

The microscopic defects in the as grown  $\text{Cs}_2\text{Hg}_6\text{S}_7$  crystals were examined under a Hitachi S4700-II scanning electron microscope (SEM) equipped with an energy dispersive spectroscopy (EDS) detector. The resistivity was measured using a two probe method using a Keithley 617 electrometer. Silver paste TED PELLA, Inc. was the contact. Seebeck measurements as a function of temperature from 300-350 K were performed under vacuum using a custom setup including a Keithley 2182A nano voltmeter and MMR Technologies K-20 temperature controller and SB-100 unit. We used the integral method of measuring the Seebeck voltage  $V(T)$ , in which one end of the sample is held at a fixed temperature  $T_0$ , and the other end is varied through the temperature  $T$  range of interest.

Photoluminescence (PL) measurements were performed at 28 K. Polished samples were placed in a helium vapor cryostat, an excitation source of He-Ne laser with emission wavelength of 633 nm was used. The PL spectrum was analyzed with a 0.75-m SPEX grating monochromator and the signal was detected with a R928 Hamamatsu photomultiplier tube (PMT) with a phase sensitive detection lock-in system.

Photoconductivity response was measured on single crystalline samples in a custom setup described above. Gold electrodes were evaporated on the front and back surfaces of the samples in parallel plate configuration.

Detector properties were measured using Ag X-ray source with 40 kV accelerating voltage and 20 mA current. One undoped- $\text{Cs}_2\text{Hg}_6\text{S}_7$  crystal sample and another  $\text{HgCl}_2$  doped sample of the same dimensions of  $\phi 7.0$  mm  $\times$  2.0 mm were cut and polished for detector measurements. Carbon paste was used as contact electrode on both sides of the crystals. A spectroscopic grade CZT crystal bought from eV Products Inc. was used reference. The  $\mu\tau$  product for electrons of the CZT crystal was  $2 \times 10^{-3} \text{cm}^2/\text{V}$ . The  $\text{Cs}_2\text{Hg}_6\text{S}_7$  samples were placed in an eV-480 test fixture

attached to an eV-550 preamplifier box. The bias voltage was 500 V. An ORTEC 572A amplifier with a gain of 1000 and 0.5  $\mu$ s shaping time was used to amplify the signal before it is evaluated by a dual 16 K input multichannel analyzer (Model ASPEC-927).

### 3.3. Results

The  $\text{Cs}_2\text{Hg}_6\text{S}_7$  crystals grown previously (see above) had relatively low resistivity of  $\approx 5 \text{ M}\Omega\cdot\text{cm}$  in the direction perpendicular to the growth,<sup>3</sup> while the resistivity of crystals grown using the raw materials synthesized by scheme 2 was  $8.3 \text{ M}\Omega\cdot\text{cm}$  after annealing.<sup>1</sup> To further increase the resistivity of  $\text{Cs}_2\text{Hg}_6\text{S}_7$  crystals, a new synthesis method was adopted in this work. In addition, Cd alloying was investigated to study the effects on the properties, we find that the Cd solubility in the material is limited. To control the resistivity, Cl/In doping was carried out to determine if we could compensate the majority carrier.

#### 3.3.1. Synthesis and crystal growth

In the previous synthesis methods (eq (1) and (2)),  $\text{Cs}_2\text{S}$  and  $\text{Cs}_2\text{S}_7$  were used as starting materials which were prepared in liquid ammonia. Although we can obtain reasonably pure  $\text{Cs}_2\text{S}_x$  binary chalcogenides using this method, because of many steps involved, there is a concern for trace amount of impurities getting into the products. We speculated that this could be one reason that leads to the relatively low resistivity of the  $\text{Cs}_2\text{Hg}_6\text{S}_7$  crystals. The “vapor transport method” reported here for the synthesis of  $\text{Cs}_2\text{Hg}_6\text{S}_7$  has fewer steps, potentially reducing the probability of bringing impurities during transfer between containers. The purity of the final polycrystalline product was confirmed by PXRD, as shown in **Figure 21** by comparing experimental and simulated diffraction patterns. Using ground polycrystalline powder, the optical band gap measured with solid-state UV-Vis spectroscopy was 1.63 eV (**Figure 22(a)**), in agreement with previous reports.

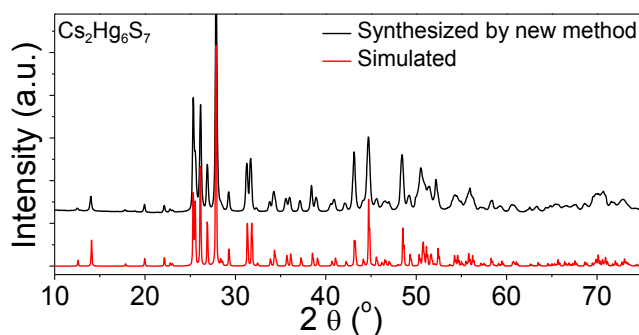


**Figure 21.** Powder X-ray diffraction patterns of  $\text{Cs}_2\text{Hg}_6\text{S}_7$  synthesized using the “vapor transport method”.

Polished specimens were used for single crystal transmittance ( $T$ ) and reflectance ( $R$ ) spectra. From  $T$  and  $R$ , the absorption coefficient ( $\alpha$ ) was calculated by:

$$\alpha = \frac{1}{d} \ln \left[ \frac{(1-R)^2}{2T} + \sqrt{\frac{(1-R)^2}{4T^2} + R^2} \right]$$

where  $d$  is the thickness of the sample. As shown in Figure 4b, a linear fit to  $\alpha^2$  versus energy gives a direct band gap 1.64 eV.

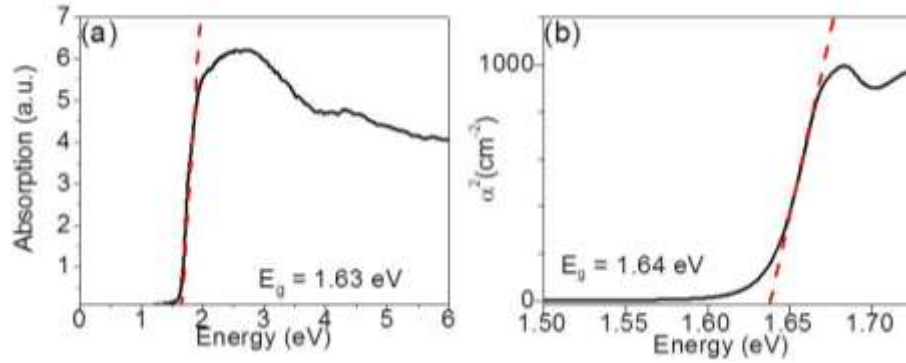


**Figure 22.** (a) UV-vis absorption spectra of polycrystalline  $\text{Cs}_2\text{Hg}_6\text{S}_7$  synthesized by vapor transport method. (b) Absorption spectrum of an undoped  $\text{Cs}_2\text{Hg}_6\text{S}_7$  single crystal.

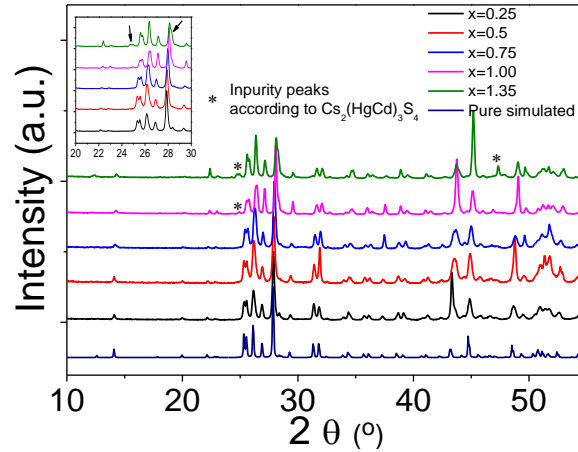


**Figure 23.** Powder X-ray diffraction patterns of  $\text{Cs}_2\text{Hg}_{6-x}\text{Cd}_x\text{S}_7$  samples ( $x = 0.25, 0.5, 0.75, 1.0, 1.35$ ).

**$\text{Cs}_2\text{Hg}_{6-x}\text{Cd}_x\text{S}_7$**  Using isovalent alloying we sought to tune the band gap and the electronic properties of  $\text{Cs}_2\text{Hg}_6\text{S}_7$ . For example, band gap of  $\text{HgTe}$  can be changed by  $\text{Cd}$  alloying.<sup>28,29</sup> Different compositions of  $\text{Cs}_2\text{Hg}_{6-x}\text{Cd}_x\text{S}_7$  ( $x = 0.25, 0.5, 0.75, 1.0, 1.35, 2.0, 3.0, 4.0$ ) were synthesized. In the samples with  $x < 1.0$ , mainly black needle crystals obtained. For samples with  $x \geq 1.0$ , in addition to black/dark red needles of  $\text{Cs}_2\text{Hg}_{6-x}\text{Cd}_x\text{S}_7$ , there were red polyhedra and yellow plate crystals, which were identified to be  $\text{Hg}_{1-y}\text{Cd}_y\text{S}$  and  $\text{Cs}_2\text{Hg}_{3-z}\text{Cd}_z\text{S}_4$  respectively (by EDS analysis). For samples with  $x = 2.0, 3.0$  and  $4.0$ , the main phase were  $\text{Hg}_{1-y}\text{Cd}_y\text{S}$  and  $\text{Cs}_2\text{Hg}_{3-z}\text{Cd}_z\text{S}_4$ . The products with different  $\text{Cd}$  concentration  $x = 0.25, 0.5, 0.75, 1.0$ , and  $1.35$  were checked by PXRD and contained peaks of  $\text{Cs}_2\text{Hg}_{3-z}\text{Cd}_z\text{S}_4$  impurity phase when  $x \geq 1.0$  (**Figure 23**). The diffraction peaks (e.g. the peaks near  $2\theta = 28^\circ$  shown in the inset of **Figure 23**) show a shift to higher angles with higher  $x$  values consistent with a decreased unit cell parameter.

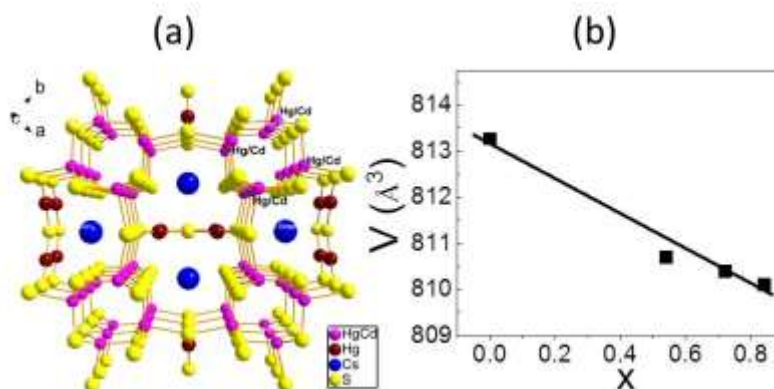


**Figure 24.** (a) Crystal structure of  $\text{Cs}_2\text{Hg}_{5.16}\text{Cd}_{0.84}\text{S}_7$ . Only the tetrahedral Hg(1) atoms are partially replaced by Cd atoms; (b) Unit cell volume of  $\text{Cs}_2\text{Hg}_{6-x}\text{Cd}_x\text{S}_7$  versus stoichiometry  $x$ .

The crystal structure of  $\text{Cs}_2\text{Hg}_6\text{S}_7$  has two distinct types of Hg sites. Hg(1) atom has tetrahedral coordination and the other Hg(2) atom has linear coordination. We hypothesized the Hg(1) atom could be replaced with Cd atom in a series of compositions  $\text{Cs}_2\text{Hg}_{6-x}\text{Cd}_x\text{S}_7$ . Black/dark red needle crystals from three samples of  $\text{Cs}_2\text{Hg}_{6-x}\text{Cd}_x\text{S}_7$  ( $x = 0.75, 1.0$  and  $1.35$ ) were picked out for single crystal X-ray refinement. The structures of the three crystals were refined successfully in the  $P4_2nm$  space group with a practically zero Frack parameter and the compounds are isostructural to  $\text{Cs}_2\text{Hg}_6\text{S}_7$ . The structure is noncentrosymmetric, because the S(2) atom is bonded to two Hg(2) atoms in an angle of  $\sim 112.5^\circ$ , and the boomerang shaped Hg(2)-S(2)-Hg(2) fragment point to the same direction along the  $c$ -axis. After assignments of the high electron density peaks as Cs, Hg and S atoms, the thermal parameters and occupancy on each Hg atom sites were examined. As we expected, only the tetrahedrally bound Hg(1) atoms are partially replaced by Cd atoms, as shown in **Figure 24a**. And the final formulae were refined as  $\text{Cs}_2\text{Hg}_{5.46}\text{Cd}_{0.54}\text{S}_7$  for  $x = 0.75$ ,  $\text{Cs}_2\text{Hg}_{5.28}\text{Cd}_{0.72}\text{S}_7$  for  $x = 1.0$  and  $\text{Cs}_2\text{Hg}_{5.16}\text{Cd}_{0.84}\text{S}_7$  for  $x = 1.35$ . The Cd concentration determined by single crystal refinement is higher than that obtained by SEM-EDS (**Table 4**). The non-homogeneous of the samples may be one reason lead to the inaccuracy of the EDS results. The complete data collection parameters, details of the structure solution and structure refinements are given in **Table 4**. The fractional coordinates and temperature factors of all atoms with estimated standard deviations are given in **Table 5**. The unit cell volume of  $\text{Cs}_2\text{Hg}_{6-x}\text{Cd}_x\text{S}_7$  decreases with increasing  $x$  as expected from the incorporation of the smaller Cd atom in the structure, **Figure 24b**. Since single crystals of  $\text{Cs}_2\text{Hg}_{6-x}\text{Cd}_x\text{S}_7$  with  $x > 0.84$  were not found in samples with nominal  $x = 2.0, 3.0$  and  $4.0$ , we deduce that the solubility of Cd in the  $\text{Cs}_2\text{Hg}_{6-x}\text{Cd}_x\text{S}_7$  system is  $\sim 0.84$ .

The band gap of  $\text{Cs}_2\text{Hg}_{6-x}\text{Cd}_x\text{S}_7$  alloys increases with higher Cd doping level, from 1.63 eV ( $x = 0$ ), 1.66 eV ( $x = 0.25$ ) to 1.84 eV ( $x = 1.35$ ), **Figure 25**. This result confirms our hypothesis that adding Cd into  $\text{Cs}_2\text{Hg}_6\text{S}_7$  can increase the band gap energy of the compound.

In the as grown Cd alloyed ingot, air sensitive yellow plate crystals ( $\text{Cs}_2\text{Hg}_{3-2}\text{Cd}_2\text{S}_4$  from EDS) could be found on the upper part of the ingot. We attribute this to the low solubility of Cd in the  $\text{Cs}_2\text{Hg}_6\text{S}_7$  structure ( $\sim 0.84$  as mentioned above), the segregation coefficient  $K_{\text{Cd}}$  (the ratio of Cd in the solid to that in the liquid phase) is calculated to be 0.69, and most of Cd is distributed

as a second phase of  $\text{Cs}_2\text{Hg}_{3-z}\text{Cd}_z\text{S}_4$  at the top of the ingot. Here the  $K_{\text{Cd}}$  is calculated based on the Cd concentration determined by single crystal diffraction.

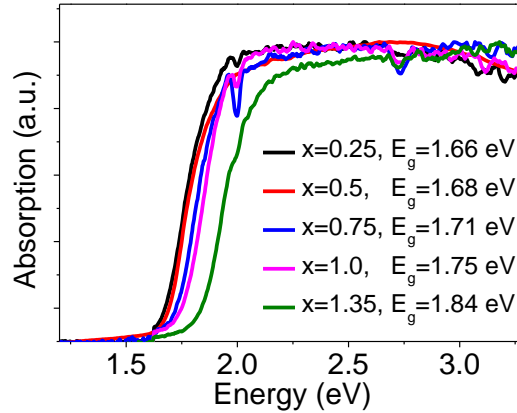


**Figure 25.** Solid state UV-vis absorption spectra of  $\text{Cs}_2\text{Hg}_{6-x}\text{Cd}_x\text{S}_7$  samples ( $x = 0.25, 0.5, 0.75, 1.0, 1.35$ ).

**3.3.2. Microscopic Defects** Cleaved crystals revealing natural faces were used for SEM imaging. The specimens were not polished or etched. **Figure 26a** shows a typical micrograph of the natural face cleaved along the  $c$ -axis from the undoped- $\text{Cs}_2\text{Hg}_6\text{S}_7$  crystal. There are apparent inclusions with dimensions ranging from  $0.05 \mu\text{m}$  to  $0.5 \mu\text{m}$ . Most of them are stripes parallel to the  $c$ -axis, while some are dots of relatively smaller size. The composition of the inclusions was not determined because the sizes are smaller than the electron beam of the SEM-EDS. Compared to inclusions observed in our previous Hg deficient grown crystals, these inclusions are much smaller although the shape and orientation are similar. Other than these inclusions, we also observed parallel strips of step bunches (**Figure 26b**) found near the edge of the natural face on the undoped- $\text{Cs}_2\text{Hg}_6\text{S}_7$  crystals. These step bunches are about  $2\text{-}3 \mu\text{m}$  in size, and they are composed of small stacking steps of about  $0.1 \mu\text{m}$ . Impurities seem to play a role in the formation of such steps.

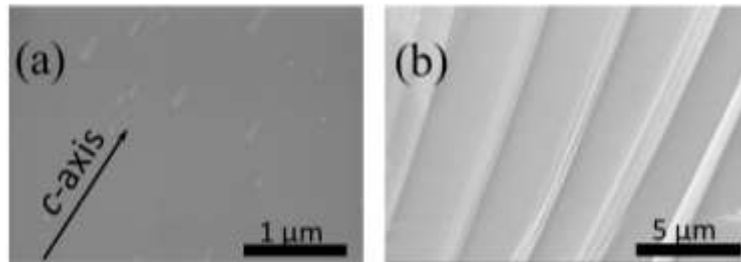


**Figure 26.** Scanning electron micrograph of (a) inclusions in the undoped  $\text{Cs}_2\text{Hg}_6\text{S}_7$  single crystal; (b) So-called step bunches found on the natural cleaved face of  $\text{Cs}_2\text{Hg}_6\text{S}_7$  crystal.

**In and Cl doping** Our previous investigations, of photoconductivity and photoluminescence indicated the presence of shallow acceptor states, which may be due to the Cs and Hg vacancies in the grown  $\text{Cs}_2\text{Hg}_6\text{S}_7$  crystals. These vacancies create holes and  $p$ -type behavior. Therefore our strategy to further increase the resistivity of  $\text{Cs}_2\text{Hg}_6\text{S}_7$  was to compensate by doping with In and Cl.

The In and Cl dopants were introduced into the  $\text{Cs}_2\text{Hg}_6\text{S}_7$  system by adding In metal and  $\text{HgCl}_2$  into the synthesis of starting polycrystalline material. The nominal doping concentration used was  $1 \times 10^{19} \text{ cm}^{-3}$  for In and  $2 \times 10^{20} \text{ cm}^{-3}$  for Cl. The doping concentrations were selected in an exploratory fashion and chosen to be similar to the concentrations used for CdTe. The as-grown ingots appear compositionally uniform, stable in air for months and mechanically robust. An exhaustive study of dopant concentrations was not done.

### 3.3.3. Seebeck coefficient and resistivity

The Seebeck coefficient and resistivity of semiconductor materials strongly depend on the composition and carrier concentration. In this work, the carrier concentration is reduced by using new synthesis method to suppress the impurities and defects, and ion doping to compensate the majority carrier and thus increase the resistivity of  $\text{Cs}_2\text{Hg}_6\text{S}_7$ . The resistivity is used as a gross measurement of the carrier concentration, since the conductivity is proportional to the carrier concentration. I-V curves of different  $\text{Cs}_2\text{Hg}_6\text{S}_7$  crystals are shown in **Figure 27**.

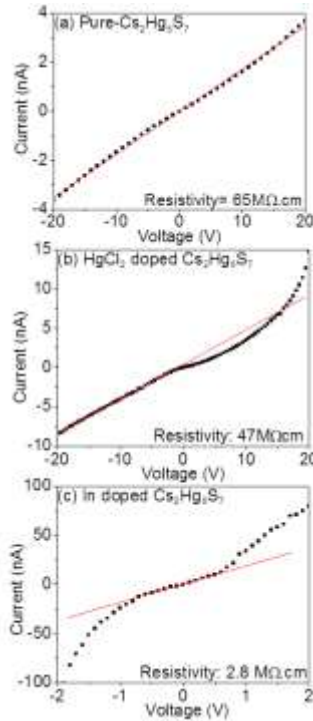


**Figure 27.** Current-voltage characteristics of  $\text{Cs}_2\text{Hg}_6\text{S}_7$  single crystals: (a) pure  $\text{Cs}_2\text{Hg}_6\text{S}_7$  crystal; (b)  $\text{HgCl}_2$  doped  $\text{Cs}_2\text{Hg}_6\text{S}_7$  crystal; (c) In doped  $\text{Cs}_2\text{Hg}_6\text{S}_7$  crystal.

The resistivity of the as grown pure  $\text{Cs}_2\text{Hg}_6\text{S}_7$  single crystal was  $0.65 \times 10^8 \Omega \cdot \text{cm}$ , which is nearly ten times higher than previously grown  $\text{Cs}_2\text{Hg}_6\text{S}_7$  crystals, indicating a lower carrier concentration. Meanwhile, the resistivity of  $\text{HgCl}_2$  doped crystals was  $0.47 \times 10^8 \Omega \cdot \text{cm}$ , of 5% Cd alloyed  $\text{Cs}_2\text{Hg}_{6-x}\text{Cd}_x\text{S}_7$  crystals  $2.0 \times 10^6 \Omega \cdot \text{cm}$  and of In doped crystals  $2.7 \times 10^6 \Omega \cdot \text{cm}$ .

The Seebeck coefficients of undoped,  $\text{HgCl}_2$  doped and In doped  $\text{Cs}_2\text{Hg}_6\text{S}_7$  crystals were measured over a temperature range from 300 to 350 K (**Figure 28**). Due to the high resistivity of the samples, the values of the Seebeck coefficients were difficult to determine accurately. The Seebeck coefficient of the undoped- $\text{Cs}_2\text{Hg}_6\text{S}_7$  crystal was positive in the range of  $\sim 10^3 \mu\text{V/K}$ , indicating a *p*-type semiconductor. That of the  $\text{HgCl}_2$  crystal was negative at  $\sim 10^3 \mu\text{V/K}$ , and for the In doped crystal was also negative at  $\sim 10^2 \mu\text{V/K}$  indicating a *n*-type behavior. These results are consistent with our expectation that by introducing Cl and In dopants compensation of holes can be achieved in  $\text{Cs}_2\text{Hg}_6\text{S}_7$ . The resistivity of the crystals however was not increased presumably due to the high concentration of Cl and In dopants. The resistivity of the  $\text{Cs}_2\text{Hg}_6\text{S}_7$  alloyed with 5at% Cd was also low, presumably due to the creation of  $\text{Cs}_2\text{Hg}_{3-z}\text{Cd}_z\text{S}_4$  impurity leading to inhomogeneous composition of the as grown crystal.



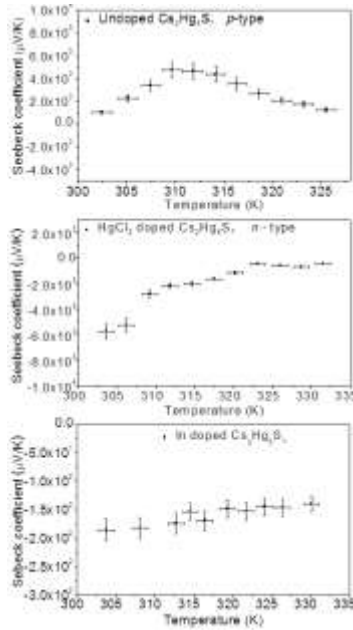


**Figure 28.** Seebeck coefficients as a function of temperature for three different  $\text{Cs}_2\text{Hg}_6\text{S}_7$  samples.

### 3.3.4. Photoluminescence, photoconductivity and detector measurements

Photoluminescence measurements are useful in studying certain luminescent defects in  $\text{Cs}_2\text{Hg}_6\text{S}_7$ . The low temperature PL spectrum at 28K of an undoped- $\text{Cs}_2\text{Hg}_6\text{S}_7$  single crystal is shown in **Figure 29**. There were no peaks near the band gap (1.63 eV), but only one broad peak around 1.54 eV, which can be decomposed using Gaussian functions into two peaks at 1.52 eV and 1.58 eV. The one at 1.52 eV is due to the donor-acceptor pair recombination, while the peak at 1.58 eV can be attributed to a defect center, as explained previously. Compared to the PL spectra of previously grown  $\text{Cs}_2\text{Hg}_6\text{S}_7$ , where four peaks (1.57 eV, 1.62 eV, 1.66 eV and 1.68 eV) were observed, in this work, where only two peaks are present, suggests that the present specimens have fewer defect centers, and thus higher crystalline quality.

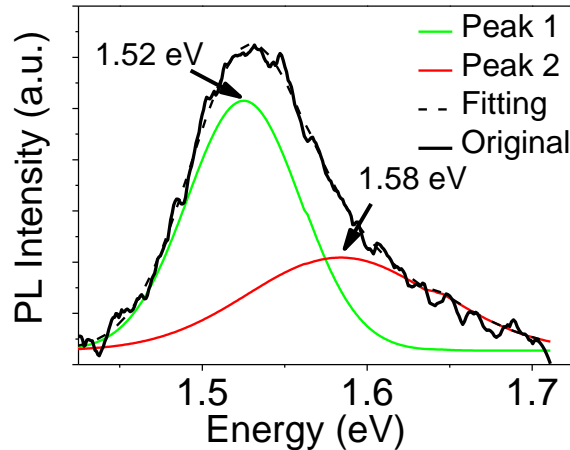


**Figure 29.** Photoluminescence of undoped  $\text{Cs}_2\text{Hg}_6\text{S}_7$  crystal at 28 K.

The photoconductivity response as a function of bias for undoped and  $\text{HgCl}_2$  doped crystal are shown in **Figure 30**. The data were fitted as described in the experimental section and the  $\mu\tau$  values were obtained for electrons and holes of all samples, as listed in **Table 6**. The electron mobility-lifetime products are  $(\mu\tau)_e = 1.3 \times 10^{-3} \text{ cm}^2/\text{V}$  for the undoped sample,  $(\mu\tau)_e = 1.7 \times 10^{-3} \text{ cm}^2/\text{V}$  for the  $\text{HgCl}_2$  doped sample, while the hole mobility-lifetime products are  $(\mu\tau)_h = 9.1 \times 10^{-4} \text{ cm}^2/\text{V}$  for the undoped sample and  $(\mu\tau)_h = 2.4 \times 10^{-3} \text{ cm}^2/\text{V}$  for the  $\text{HgCl}_2$  doped sample. The hole mobility-lifetime products of  $\text{Cs}_2\text{Hg}_6\text{S}_7$  crystals are greatly improved compared to those measured in the early stages of this work above. Furthermore, the  $(\mu\tau)_h$  for  $\text{HgCl}_2$  doped  $\text{Cs}_2\text{Hg}_6\text{S}_7$  is much higher than the commercial benchmark detector material CZT ( $\sim 10^{-4} \text{ cm}^2/\text{V}^3$ ).

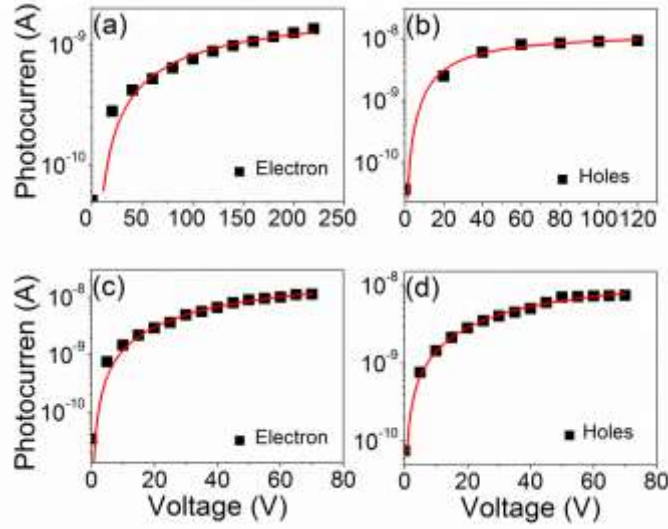


**Figure 30.** Photocurrent response of  $\text{Cs}_2\text{Hg}_6\text{S}_7$  samples: (a) and (b) electrons and holes of undoped  $\text{Cs}_2\text{Hg}_6\text{S}_7$  crystal, (c) and (d) electrons and holes of  $\text{HgCl}_2$  doped  $\text{Cs}_2\text{Hg}_6\text{S}_7$  crystal.

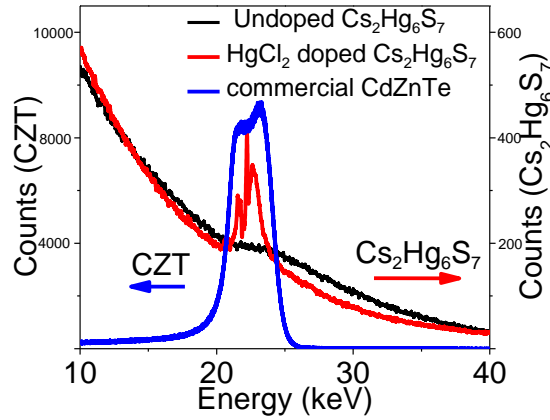


**Figure 31.** Spectroscopy response of  $\text{Cs}_2\text{Hg}_6\text{S}_7$  crystals to Ag X-ray unfiltered radiation and comparison with a commercial CZT crystal.

The spectroscopic radiation response of two  $\text{Cs}_2\text{Hg}_6\text{S}_7$  crystals (one undoped and one  $\text{HgCl}_2$  doped) was evaluated using unfiltered Ag X-ray radiation source (22 keV). Both  $\text{Cs}_2\text{Hg}_6\text{S}_7$  crystals can detect X-rays (**Figure 31**). There is a broad peak in the spectrum detected by the undoped crystal, while there are sharp peaks detected by the  $\text{HgCl}_2$  doped crystal. The  $\text{HgCl}_2$  doped crystal gives better response probably due to its higher  $(\mu\tau)_h$  for holes than that of the undoped crystal. Comparing to the commercial CZT crystal, the spectra for both  $\text{Cs}_2\text{Hg}_6\text{S}_7$  crystals are much weaker, have more noise and higher background. One reason is that the resistivity of our  $\text{Cs}_2\text{Hg}_6\text{S}_7$  crystals is still much lower compared to CZT. Another reason may be the carbon paste used as contact material for anode and cathode, which is not an optimized. This could lead to high surface leakage current and insufficient collection of excited electron and hole carriers.

To conclude polycrystalline  $\text{Cs}_2\text{Hg}_6\text{S}_7$  material was synthesized using a so called “vapor transport method”, and single crystals with resistivity  $\sim 30$  times higher than previously

reported were grown by the Bridgman method using improved growth conditions. Low temperature PL spectra confirm that there are fewer defect centers in the grown crystal. Inclusions with dimensions range from 0.05  $\mu\text{m}$  to 0.5  $\mu\text{m}$  and step bunches were found in the crystals by SEM. Alloying with Cd increases the band gap of  $\text{Cs}_2\text{Hg}_{6-x}\text{Cd}_x\text{S}_7$  from 1.63 to 1.83 eV. Cl and In act as donor dopants and produce *n*-type samples. The  $(\mu\tau)$  products of the compound have been greatly improved to  $> 10^{-3} \text{ cm}^2/\text{V}$ . While In doping at the relatively large concentrations used decreased the resistivity,  $\text{HgCl}_2$  doping gave a similar conductivity to the undoped material. The property that was impacted most by the  $\text{HgCl}_2$  doping was the  $(\mu\tau)$  for holes which improved by over one order of magnitude. The  $(\mu\tau)_h = 2.4 \times 10^{-3} \text{ cm}^2/\text{V}$  for  $\text{HgCl}_2$  doped  $\text{Cs}_2\text{Hg}_6\text{S}_7$  is higher than commercial CZT. Though, the resistivity of these crystals is still lower than desired, it is markedly improved over previous samples and both undoped and  $\text{HgCl}_2$ -doped  $\text{Cs}_2\text{Hg}_6\text{S}_7$  crystals have shown response to Ag X-ray with the spectrum obtained using the latter crystals showing higher resolution. Future work will aim at increasing the resistivity and detector response through improvements in purity as well as native defect control.

**Table 4.** Crystal data and structure refinement for  $\text{Cs}_2\text{Hg}_{5.46}\text{Cd}_{0.54}\text{S}_7$ ,  $\text{Cs}_2\text{Hg}_{5.28}\text{Cd}_{0.72}\text{S}_7$  and  $\text{Cs}_2\text{Hg}_{5.16}\text{Cd}_{0.84}\text{S}_7$ .

Empirical formula	$\text{Cs}_2\text{Hg}_{5.46}\text{Cd}_{0.54}\text{S}_7$	$\text{Cs}_2\text{Hg}_{5.28}\text{Cd}_{0.72}\text{S}_7$	$\text{Cs}_2\text{Hg}_{5.16}\text{Cd}_{0.84}\text{S}_7$
Formula weight	1646.16	1629.84	1620.14
Temperature, Wavelength		293(2) K, 0.71073 Å	
Crystal system, Space group		Tetragonal, $P4_2nm$	
Unit cell dimensions	$a = 13.968(2) \text{ Å}$ , $c = 4.1551(8) \text{ Å}$ , $\alpha = \beta = \gamma = 90.00^\circ$	$a = 13.963(2) \text{ Å}$ , $c = 4.1567(8) \text{ Å}$ , $\alpha = \beta = \gamma = 90.00^\circ$	$a = 13.966(2) \text{ Å}$ , $c = 4.1535(8) \text{ Å}$ , $\alpha = \beta = \gamma = 90.00^\circ$
Volume, Z	810.7(2) Å <sup>3</sup> , 2	810.4(2) Å <sup>3</sup> , 2	810.1(2) Å <sup>3</sup> , 2
Density (calculated)	6.743 g/cm <sup>3</sup>	6.679 g/cm <sup>3</sup>	6.642 g/cm <sup>3</sup>
Absorption coefficient	57.492 mm <sup>-1</sup>	56.010 mm <sup>-1</sup>	55.131 mm <sup>-1</sup>
F(000)	1369	1358	1351
Crystal size	0.05 × 0.03 × 0.12 mm <sup>3</sup>	0.08 × 0.08 × 0.2 mm <sup>3</sup>	0.04 × 0.03 × 0.1 mm <sup>3</sup>
$\theta$ range for data collection	2.06 to 29.18°	2.06 to 29.12°	2.06 to 24.95°
Index ranges	-7 ≤ h ≤ 18, -19 ≤ k ≤ 19, -5 ≤ l ≤ 4	-19 ≤ h ≤ 19, -19 ≤ k ≤ 16, -5 ≤ l ≤ 4	-11 ≤ h ≤ 16, -16 ≤ k ≤ 16, -4 ≤ l ≤ 4
Reflections collected	3725	7568	2481
Independent reflections	1080 [ $R_{\text{int}} = 0.0458$ ]	1090 [ $R_{\text{int}} = 0.0746$ ]	732 [ $R_{\text{int}} = 0.1555$ ]
Completeness to $\theta = 24.95^\circ$	99.5%	99.8%	99.8%
Refinement method	Full-matrix least-squares on $F^2$		
Data / restraints / parameters	1080 / 1 / 44	1090 / 1 / 44	732 / 1 / 43
Goodness-of-fit	1.026	1.047	1.082
Final R indices [ $>2\sigma(I)$ ]	$R_{\text{obs}} = 0.0268, wR_{\text{obs}} = 0.0602$	$R_{\text{obs}} = 0.0261, wR_{\text{obs}} = 0.0581$	$R_{\text{obs}} = 0.0595, wR_{\text{obs}} = 0.1587$
R indices [all data]	$R_{\text{all}} = 0.0290, wR_{\text{all}} = 0.0644$	$R_{\text{all}} = 0.0265, wR_{\text{all}} = 0.0584$	$R_{\text{all}} = 0.0604, wR_{\text{all}} = 0.1647$
Extinction coefficient	0.0075(3)	0.00334(15)	0.0042(7)
Largest diff. peak and hole	1.628 and -2.036 e·Å <sup>-3</sup>	1.410 and -1.003 e·Å <sup>-3</sup>	3.900 and -2.563 e·Å <sup>-3</sup>

$R = \sum ||F_o| - |F_c|| / \sum |F_o|$ ,  $wR = \{\sum [w(|F_o|^2 - |F_c|^2)^2] / \sum [w(|F_o|^4)]\}^{1/2}$  and calc  $w = 1/[\sigma^2(F_o^2) + (0.1092P)^2 + 28.0106P]$  where  $P = (F_o^2 + 2F_c^2)/3$

**Table 5.** Atomic coordinates ( $\times 10^4$ ) and equivalent isotropic displacement parameters ( $\text{\AA}^2 \times 10^3$ ) for  $\text{Cs}_2\text{Hg}_{5.46}\text{Cd}_{0.54}\text{S}_7$ ,  $\text{Cs}_2\text{Hg}_{5.28}\text{Cd}_{0.72}\text{S}_7$  and  $\text{Cs}_2\text{Hg}_{5.16}\text{Cd}_{0.84}\text{S}_7$  at 293(2) K with estimated standard deviations in parentheses.

Label	x	y	z	Occupancy	$U_{\text{eq}}^*$
$\text{Cs}_2\text{Hg}_{5.46}\text{Cd}_{0.54}\text{S}_7$					
Hg(1)	0.1526(1)	0.4264(1)	0.4248(2)	0.865(7)	29(1)
Cd(1)	0.1526(1)	0.4264(1)	0.4248(2)	0.135(7)	29(1)
Hg(2)	0.4007(1)	0.4007(1)	0.10188(2)	1	25(1)
Cs(1)	0.6686(1)	0.3314(1)	0.4156(3)	1	27(1)
S(1)	0.3168(2)	0.3168(2)	0.14208(11)	1	20(1)
S(2)	0.5	0.5	0.7045(14)	1	25(2)
S(3)	0.212(2)	0.3084(2)	0.4242(7)	1	20(1)
$\text{Cs}_2\text{Hg}_{5.28}\text{Cd}_{0.72}\text{S}_7$					
Hg(1)	0.1526(1)	0.4266(1)	0.4248(1)	0.819(7)	25(1)
Cd(1)	0.1526(1)	0.4266(1)	0.4248(1)	0.181(7)	25(1)
Hg(2)	0.4007(1)	0.4007(1)	0.10187(2)	1	21(1)
Cs(1)	0.6685(1)	0.3315(1)	0.4149(3)	1	22(1)
S(1)	0.3168(2)	0.3168(2)	0.14193(10)	1	14(1)
S(2)	0.5	0.5	0.7037(13)	1	19(1)
S(3)	0.211(2)	0.3083(2)	0.4244(6)	1	15(1)
$\text{Cs}_2\text{Hg}_{5.16}\text{Cd}_{0.84}\text{S}_7$					
Hg(1)	0.1525(1)	0.4264(1)	0.4247(2)	0.791(16)	26(1)
Cd(1)	0.1525(1)	0.4264(1)	0.4247(2)	0.209(16)	26(1)
Hg(2)	0.4007(1)	0.4007(1)	0.10195(6)	1	25(1)
Cs(1)	0.6685(2)	0.3315(2)	0.4143(8)	1	27(1)
S(1)	0.3169(4)	0.3169(4)	0.1421(3)	1	20(2)
S(2)	0.5	0.5	0.705(4)	1	22(3)
S(3)	0.215(4)	0.3079(4)	0.4234(16)	1	20(2)

\*  $U_{\text{eq}}$  is defined as one third of the trace of the orthogonalized  $U_{ij}$  tensor.

**Table 6.** Comparison of different  $\text{Cs}_2\text{Hg}_6\text{S}_7$  crystals: resistivity and photoconductive properties.

Sample number	Synthesis method	Doping/ Alloying	Resistivity ( $\text{M}\Omega\cdot\text{cm}$ )	$(\mu\tau)_e$ ( $\text{cm}^2/\text{V}$ )	$(I_0)_e$ (nA)	$(s/\mu)_e$ ( $\text{V}\cdot\text{cm}^{-1}$ )	$(\mu\tau)_h$ ( $\text{cm}^2/\text{V}$ )	$(I_0)_h$ (nA)	$(s/\mu)_h$ ( $\text{V}\cdot\text{cm}^{-1}$ )	Reference
JA	(1)	no	5.0	$2 \times 10^{-3}$			$3.4 \times 10^{-4}$			[ <sup>13</sup> ]
HL1-192-1	(2)	Excess S	8.3	$1.2 \times 10^{-3}$	4.0		$1.1 \times 10^{-4}$	0.8		[ <sup>1</sup> ]
HL2-4-1	(3)	no	65	$1.3 \times 10^{-3}$	2.1	584	$9.1 \times 10^{-4}$	12.8	65	This work
HL2-102-2	(3)	$\text{HgCl}_2$	47	$1.7 \times 10^{-3}$	30.9	14.8	$2.4 \times 10^{-3}$	15.1	4.0	This work
HL2-126-1	(3)	Cd	2.7	$8.2 \times 10^{-5}$	0.2	39	$1.1 \times 10^{-4}$	0.1	20	This work
HL2-159-1	(3)	In	2.0	NA			NA			This work
CZT		Zn	$1 \times 10^4$	$4.5 \times 10^{-2}$			$1.1 \times 10^{-4}$			[ <sup>7,10</sup> ]

#### **4.0. QUATERNARY MATERIALS**

In addition to work on the ternary materials described above we also investigated the quaternary Cs/Cd/In/Q (Q = Se, Te) system and studied in detail two CsCdInSe<sub>3</sub> and CsCdInTe<sub>3</sub>, synthesized using the flux method. Their crystal structures, electronic band structures, and optical absorption properties are reported. Single crystals of CsCdInSe<sub>3</sub> and CsCdInTe<sub>3</sub> with dimensions up to 1 cm have been grown by the vertical Bridgman method. The resistivity and photoconductivity measurements on the single crystals are reported and the obtained carrier mobility-lifetime products demonstrate their relevance as X-ray and  $\gamma$ -ray detection materials.

##### **4.1. Experimental work on quaternary materials**

The following reagents were used as received: (i) Indium metal, 99.99%, Cerac, Milwaukee, WI; (ii) Cadmium powder, 99.99%, Alfa Aesar, Ward Hill, MA; (iii) Cesium metal, 99.9+%, Strem Chemicals, Newburyport, MA. Selenium (99.999%) and Tellurium shot, 99.99% (5N Plus Inc, St-Laurent, QC, Canada) were purified by the fast Bridgman method. The raw material was loaded into fused silica tubes and sealed under a vacuum of  $< 10^{-4}$  mbar. A single zone Bridgman furnace was used for the purification, with the furnace set to 240 °C for Se and 500 °C for Te, and a lowering speed of  $\sim 8$ -15 cm/d. After one run, the furnace was cooled to room temperature and the top and bottom parts of the ingots were discarded. The processes were repeated 3-4 times and the obtained ingots were ground into powder for the synthesis of starting material for crystal growth. Cs<sub>2</sub>Se<sub>3</sub> and Cs<sub>2</sub>Te<sub>3</sub> were synthesized by stoichiometric reaction in liquid ammonia.

CsCdInSe<sub>3</sub> (**I**) was first found by discovery synthesis using the alkali metal flux method.<sup>36-40</sup> A mixture of Cs<sub>2</sub>Se<sub>3</sub> (0.1859 g, 0.37 mmol), Cd powder (0.0415 g, 0.37 mmol), In metal (0.0849 g, 0.74 mmol), and Se powder (0.0584 g, 0.74 mmol) in the ratio of 1:1:2:2 was loaded into a 9 mm O.D. carbon coated quartz tube in a N<sub>2</sub>-filled glove box. The tube was flame sealed under a vacuum of  $< 10^{-4}$  mbar and placed in a temperature controlled furnace. The mixture was heated slowly from room temperature to 200 °C and kept there for 12 h, then heated to 600 °C in 8 h and kept there for 2 d, and then cooled to room temperature in 10 h. The product was washed with degassed DMF to remove the excess Cs<sub>2</sub>Se<sub>x</sub> flux and dried with ether. The final product consisted of yellow and orange-red plate-like crystals. Semi-quantitative energy-dispersive (EDS) analysis of the yellow crystals indicated an average composition of Cs<sub>1.0</sub>In<sub>1.03</sub>Se<sub>2.39</sub> (CsInSe<sub>2</sub>). EDS on the orange-red crystals indicated an average composition of Cs<sub>1.0</sub>Cd<sub>1.03</sub>In<sub>0.97</sub>Se<sub>2.95</sub> (CsCdInSe<sub>3</sub>). Following the crystal structure determination, a direct combination reaction based on the CsCdInQ<sub>3</sub> composition was subsequently used for the preparation of the target compounds as single phases (see below). The structure and physical properties of CsInSe<sub>2</sub> and CsInTe<sub>2</sub> have not been reported in detail, therefore in this work we also synthesized and characterized the two ternaries for comparison with the quaternaries. Efforts to synthesize the heavier analogs of CsHgInS<sub>3</sub>, e.g. CsHgInQ<sub>3</sub> (Q=Se, Te) were not successful. Reactions involving Cs/Hg/In/Q (Q=Se, Te) yielded only binary HgQ and ternary CsInQ<sub>2</sub> as identifiable phases.

**Synthesis of CsCdInSe<sub>3</sub> (**I**).** A mixture of Cs<sub>2</sub>Se<sub>3</sub> (0.1508 g, 0.3 mmol), Cd (0.0674 g, 0.6 mmol), In (0.0688 g, 0.6 mmol), Se (0.0710 g, 0.9 mmol) was loaded and sealed as described above. The

mixture was heated slowly to 200 °C from room temperature and kept there for 6h, then heated to 800 °C in 8h and kept there for 1 d, and finally cooled to room temperature in 1 d. Orange red crystals can be picked out from the black ingot, with a yield of ~95% based on In.

**CsCdInTe<sub>3</sub> (II).** Cs<sub>2</sub>Te<sub>3</sub> (0.2594 g, 0.4 mmol), Cd (0.0899 g, 0.8 mmol), In (0.0918 g, 0.8 mmol), Te (0.1531 g, 1.2 mmol) was loaded and sealed as described above. The mixture was heated to 650 °C in 18h and kept there for 2.5 d, and then cooled to room temperature in 3 d. Dark red crystals can be picked out from the black ingot, with a yield of ~92%. Semiquantitative energy-dispersive (EDS) analysis on several crystals indicated an average composition of Cs<sub>1.0</sub>Cd<sub>1.02</sub>In<sub>1.08</sub>Te<sub>3.19</sub>.

**Crystal growth.** In order to get high purity quaternary polycrystalline raw materials, another method was adopted to synthesize the compounds for subsequent large crystal growth. Here we call it the "vapor transport method". For the synthesis of CsCdInSe<sub>3</sub> (I): Cd powder (0.7394 g, 6.5 mmol), small In metal pieces (0.7552 g, 6.5 mmol), Se powder (1.5581 g, 19.7 mmol) were loaded into a 15 mm quartz tube first. A short 9 mm quartz crucible filled with Cs metal (0.8942 g, 6.5 mmol) was then loaded into the 15 mm tube and held in place by an indentation that was made in advance in the middle of the 15 mm tube. The setup is shown in **Figure 32**. The tube was sealed under a vacuum of  $< 10^{-4}$  mbar, and then placed vertically into a tube furnace. The temperature was raised to 240 °C over 24h and held there for 24h followed by heating to 600 °C over 6h. After 1 d at 600 °C, the tube was cooled to room temperature in 6h. Products were taken out of the tube by scraping with a spatula, and then ground and reloaded into a carbon coated fused silica tube. The tube then was sealed and reheated to 800 °C for 2 d to ensure a complete reaction and pure raw material. CsCdInTe<sub>3</sub> (II) was synthesized in the same way as (I), using the starting materials: Cd powder (0.6986 g, 6.2 mmol), In metal (0.7135 g, 6.2 mmol), grounded Te powder (2.3791 g, 18.6 mmol) and Cs metal (0.8260 g, 6.2 mmol). The polycrystalline samples of (I) and (II) were loaded into carbon coated fused silica crucibles with a tapered bottom and sealed under a pressure of  $< 10^{-4}$  mbar. The crucibles were loaded into a home made two-zone vertical Bridgman furnace. The temperature of the furnace for CsCdInSe<sub>3</sub> was set at 920 °C for the hot zone and at 650 °C for cool zone, while for CsCdInTe<sub>3</sub> the temperatures were 800 °C and 530 °C, respectively. The temperature gradient in the growth zone was ~10–30 °C/cm. The tube lowering speed was ~1–5 cm/day. After the growth run, the furnaces were cooled to room temperature in 24h.

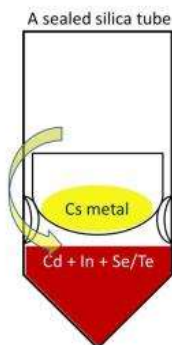


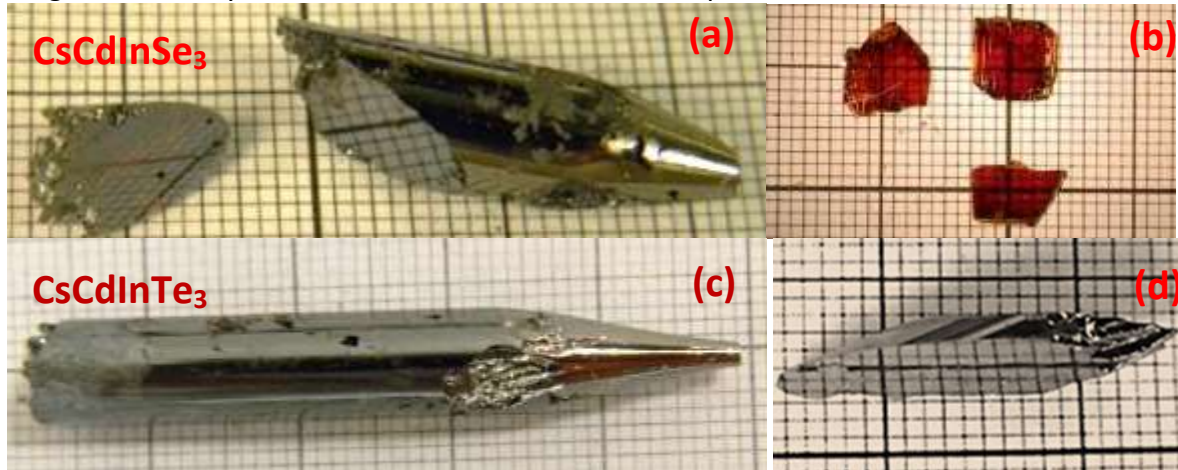
**Figure 32.** The set up of the “vapor transfer method” for synthesis of CsCdInQ<sub>3</sub> (Q=Se,Te).

Small single crystals of **I**, **II**, **III** and **IV** were picked manually and mounted on thin glass fibers. Single crystal intensity data of the four compounds were collected at room temperature using a STOE IPDS II diffractometer with Mo K $\alpha$  ( $\lambda = 0.71073$  Å) radiation operating at 50 kV and 40 mA with a 34 cm diameter imaging plate. The parameters for data collection and the details of the structure refinement are given in **Table 7**.

**Table 7.** Crystallographic data and refinement details for CsCdInQ<sub>3</sub> and CsInQ<sub>2</sub> ( Q = Se, Te ) at 293(2) K.

Empirical formula	CsCdInSe <sub>3</sub>	CsCdInTe <sub>3</sub>	CsInSe <sub>2</sub>	CsInTe <sub>2</sub>
Formula weight	1194.02	1485.86	811.30	1005.86
Temperature			293(2) K	
Wavelength			0.71073 Å	
Crystal system			Monoclinic	
Space group			C2/c	
Unit cell dimensions	$a = 11.708(2)$ Å, $b = 11.712(2)$ Å, $c = 23.051(5)$ Å, $\beta = 97.28(3)^\circ$	$a = 12.523(3)$ Å, $b = 12.517(3)$ Å, $c = 24.441(5)$ Å, $\beta = 97.38(3)^\circ$	$a = 11.573(2)$ Å, $b = 11.555(2)$ Å, $c = 17.000(3)$ Å, $\beta = 99.71(3)^\circ$	$a = 12.344(3)$ Å, $b = 12.343(3)$ Å, $c = 18.059(4)$ Å, $\beta = 99.86(3)^\circ$
Volume	3135.6(11) Å <sup>3</sup>	3799.3(13) Å <sup>3</sup>	2240.6(8) Å <sup>3</sup>	2710.7(9) Å <sup>3</sup>
Z	8	8	8	8
Density (calculated)	5.059 g/cm <sup>3</sup>	5.195 g/cm <sup>3</sup>	4.810 g/cm <sup>3</sup>	4.929 g/cm <sup>3</sup>
Absorption coefficient	24.044 mm <sup>-1</sup>	17.380 mm <sup>-1</sup>	23.443 mm <sup>-1</sup>	17.076 mm <sup>-1</sup>
F(000)	4064	4928	2752	3328
Crystal size	0.08 x 0.04 x 0.01 mm <sup>3</sup>	0.10 x 0.03 x 0.01 mm <sup>3</sup>	0.17 x 0.06 x 0.02 mm <sup>3</sup>	0.20 x 0.09 x 0.03 mm <sup>3</sup>
$\theta$ range for data collection	1.78 to 24.99°	2.31 to 25.00°	2.43 to 29.23°	2.29 to 25.00°
Index ranges	-13<= $h$ <=13, - 13<= $k$ <=13, - 27<= $l$ <=26	-14<= $h$ <=14, - 14<= $k$ <=14, - 28<= $l$ <=23	-15<= $h$ <=15, - 15<= $k$ <=14, - 23<= $l$ <=23	-14<= $h$ <=14, - 14<= $k$ <=14, - 21<= $l$ <=21
Reflections collected	9680	9334	8189	8625
Independent reflections	2747 [R <sub>int</sub> = 0.0678]	3338 [R <sub>int</sub> = 0.0655]	2993 [R <sub>int</sub> = 0.1414]	2389 [R <sub>int</sub> = 0.1300]
Completeness to $\theta = 25.00^\circ$	99.9%	99.3%	98.2%	100%
Refinement method	Full-matrix least-squares on F <sup>2</sup>			
Data / restraints / parameters	2747 / 0 / 110	3338 / 1 / 115	2993 / 0 / 74	2389 / 0 / 74
Goodness-of-fit	1.066	0.988	0.977	0.989
Final R indices [ $>2\sigma(I)$ ]	R <sub>obs</sub> = 0.0497, wR <sub>obs</sub> = 0.0778	R <sub>obs</sub> = 0.0429, wR <sub>obs</sub> = 0.0993	R <sub>obs</sub> = 0.0702, wR <sub>obs</sub> = 0.1675	R <sub>obs</sub> = 0.0470, wR <sub>obs</sub> = 0.1014
R indices [all data]	R <sub>all</sub> = 0.0901, wR <sub>all</sub> = 0.0883	R <sub>all</sub> = 0.0760, wR <sub>all</sub> = 0.1107	R <sub>all</sub> = 0.1297, wR <sub>all</sub> = 0.1979	R <sub>all</sub> = 0.0867, wR <sub>all</sub> = 0.1118
Largest diff. peak and hole	1.186 and -0.997 e·Å <sup>-3</sup>	3.011 and -1.457 e·Å <sup>-3</sup>	2.335 and -2.021 e·Å <sup>-3</sup>	1.710 and -1.366 e·Å <sup>-3</sup>

**Figure 33** shows the large ingots and single crystals of **I** and **II** grown using the Bridgman method; single crystals up to 1 cm in length can be separated from the ingots. Due to the layered structure, CsCdInQ<sub>3</sub> single crystals are apt to cleave along the (001) plane, which was determined from X-ray diffraction as shown in the Supporting Information. The CsCdInSe<sub>3</sub> single crystal is orange-red, while CsCdInTe<sub>3</sub> appears dark red under an optical microscope and almost black by eye. The CsCdInSe<sub>3</sub> crystal is stable in air for about one month, while the CsCdInTe<sub>3</sub> crystal is stable in air for a couple of days. Both crystals are oxidized when exposed to air for a long time, so they should be stored under inert atmosphere.

**Figure 33.** The as grown CsCdInSe<sub>3</sub> (a), (b) and CsCdInTe<sub>3</sub> (c), (d) ingots and single crystals.

A Hitachi S-3400 scanning electron microscope (SEM) equipped with a PGT energy dispersive X-ray analyzer was used for semi-quantitative microprobe analyses of the crystals. Data were collected with an accelerating voltage of 25 kV and a 60 s accumulation time.

Differential thermal analysis (DTA) was performed with a computer-controlled Shimadzu DTA-50 thermal analyzer. The ground single crystals (~30 mg total mass) of **I** and **II** were sealed in fused silica ampoules under vacuum. An ampoule containing  $\alpha\text{-Al}_2\text{O}_3$  of equal mass was sealed and placed on the reference side of the detector. For  $\text{CsCdInSe}_3$  (**I**), the sample and reference were heated to 900 °C at a rate of 5 °C/min and cooled at a rate of 5 °C/min to 50 °C. For  $\text{CsCdInTe}_3$  (**II**), the sample and reference were heated to 800 °C at a rate of 5 °C/min and cooled at a rate of 5 °C/min to 50 °C. All DTA measurements have been repeated once. The products of the DTA experiments were examined by X-ray powder diffraction.

The electronic band structures of  $\text{CsCdInSe}_3$  (**I**) and  $\text{CsCdInTe}_3$  (**II**) were investigated by first-principles electronic structure calculations within the density functional theory (DFT) framework. We employed the plane-wave basis set and pseudo-potential scheme using the projector augmented wave method<sup>45</sup> implemented in the Vienna Atomic Simulation Package (VASP) code. The cut-off energy for the plane-wave basis was set to 450 eV and a 10x10x4 k-point mesh was used for Brillouin zone sampling. For exchange-correlation functional, generalized gradient approximation (GGA) method is used with Perdew-Burke-Ernzerhof formalism.

Resistivity measurements were conducted through a two probe direct-current method on selected plate crystals using a Keithley 617 electrometer. The resistance of the plate crystals was measured both perpendicular and parallel to the (001) plane. In order to avoid electromagnetic noise and light illumination, a metallic enclosure was used. Carbon paste bought from TED PELLA, Inc. was used as contact materials for the two compounds. Measurements were repeated after 4-5 d with no changes observed. Photoconductivity response was measured on the single crystalline samples in a custom setup available in the Wessels lab. A diode laser (405 nm) with stable intensity was focused on the crystal sample and the chopper frequency was kept at 51 Hz. The photocurrent passing through the crystals was recorded as a function of positive and negative voltage up to 150 V.

## **4.2. Discussion of findings**

### **4.2.1. Synthesis and crystal growth**

$\text{CsInQ}_2$  and  $\text{CsCdInQ}_3$  (Q = Se, Te) can be synthesized in high yield by stoichiometric reaction of  $\text{Cs}_2\text{Q}_3$ , Q, Cd and In (Q = Se, Te). The powder XRD patterns for the ground crystals are shown in **Figure 34**. The experimental Bragg peak positions match well with the simulated patterns calculated from the refined crystal structures, which are described later in this paper.  $\text{CsInSe}_2$  and  $\text{CsInTe}_2$  were first found in this work as byproducts of the reactive alkali metal flux reactions. They can be synthesized in high purity by direct combination at 600 °C and 700 °C respectively. Since  $\text{CsInSe}_2$  has a relatively low density for a  $\gamma$ -ray detector material and  $\text{CsInTe}_2$  is air sensitive, we focused our work on the quaternary compounds  $\text{CsCdInQ}_3$  (Q = Se, Te).

From the DTA curves shown in **Figure 35** compounds (**I**) and (**II**) appear to melt congruently. For  $\text{CsCdInSe}_3$  (**I**), there is only one endothermic peak at 858 °C on the heating curve and one exothermic peak at 800 °C on the cooling curve; while for  $\text{CsCdInTe}_3$  (**II**), there is one endothermic peak observed at 738 °C upon heating and one exothermic peak at 716 °C upon cooling. All DTA curves were repeatable and the PXRD pattern of the material obtained after the DTA experiment confirmed that both compounds crystallized as pure single phases. Therefore, large single crystals of  $\text{CsCdInSe}_3$  (**I**) and  $\text{CsCdInTe}_3$  (**II**) can be grown by the Bridgman



method. Although the partial vapor pressures of Cs and Cd are somewhat high, both of the title compounds melt at relatively low temperatures and can be grown in an ordinary carbon coated fused silica tube without any high pressure protection.

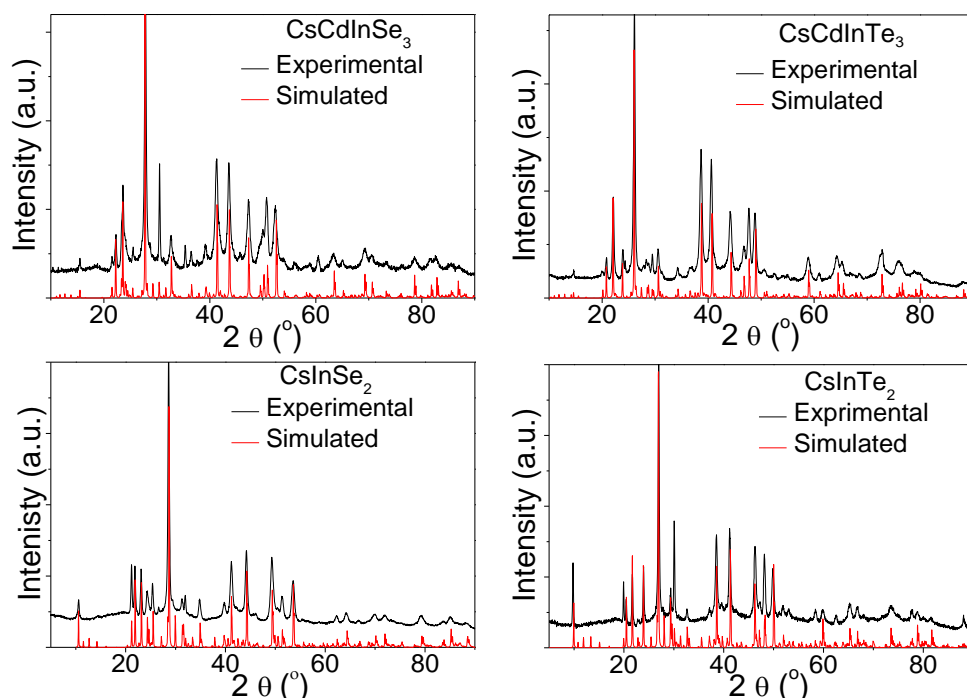


**Figure 34.** PXRD patterns of  $\text{CsCdInSe}_3$ ,  $\text{CsCdInTe}_3$ ,  $\text{CsInSe}_2$  and  $\text{CsInTe}_2$  compounds compared against the simulated patterns.

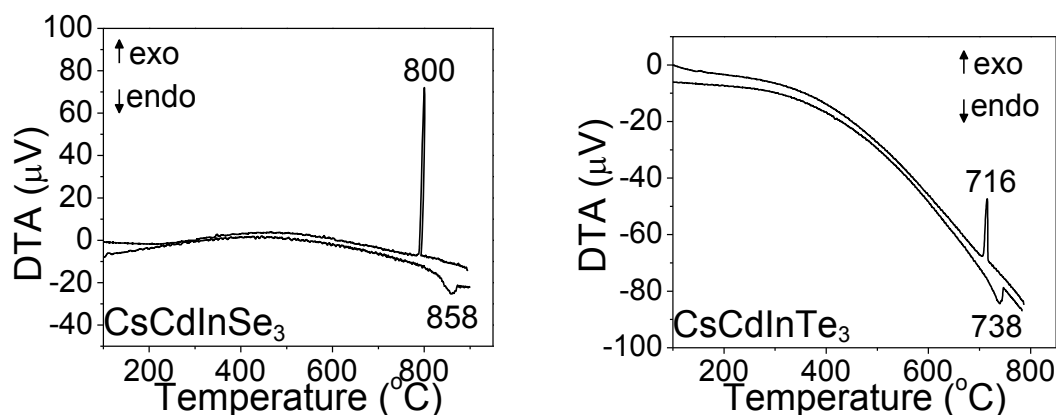


**Figure 35.** DTA curves of  $\text{CsCdInSe}_3$  and  $\text{CsCdInTe}_3$  compounds. Both  $\text{CsCdInSe}_3$  and  $\text{CsCdInTe}_3$  melt congruently at 858 °C and 738 °C, respectively.

#### 4.2.2. Structure description

In  $\text{CsCdInSe}_3$  the adamantane-type  $\text{In}_4\text{Se}_{10}$  units are found in the middle by the insertion of the  $[\text{CdSe}]$  layers, which are built of  $\text{CdSe}_4$  tetrahedra; the In and Se atoms lie above and below the  $[\text{CdSe}]$  layers, **Figure 36(B)**. The resulting  $[\text{Cd}_2\text{In}_2\text{Se}_6]^{2-}$  layers (**Figure 36(A)**) are packing along the  $c$ -axis (**Figure 36(C)**). The Cs atoms are also in the grooves between the In-Se chains. The full structure of  $\text{CsCdInSe}_3$  is shown in **Figure 36(C)**. In the structure of  $\text{CsCdInSe}_3$ , the Cd-Se bond

distances are in the range of 2.609(2)-2.631(2) Å, the In-Se bond distances vary from 2.5705(19)-2.592(2) Å. Since the contrast between the atomic structure factors of Cd and In is very small and practically indistinguishable by conventional X-ray diffraction we utilized valence-bond-sum calculations to address the assignment of Cd and In sites in the CsCdInQ<sub>3</sub> system. Using valence-bond sum calculations the three Cd<sup>2+</sup> sites were found to be 2.16, 2.17 and 2.13, respectively, whereas valence sum for the two In<sup>3+</sup> sites gave 2.97 and 2.96. When the Cd<sup>2+</sup> and In<sup>3+</sup> sites were exchanged in the model, the valence sum for In<sup>3+</sup> was in the 2.58-2.61 range, while the valence sum for Cd<sup>2+</sup> was around 2.44. The valence bond sum for the latter case where Cd and In sites were exchanged deviates significantly from the expected values of 2 and 3 respectively indicating that the assignment of Cd and In sites in the former model is more reasonable.

The structure of CsCdInTe<sub>3</sub> can be solved as isostructural analogue to CsCdInSe<sub>3</sub>. The difference is that the five Cd<sup>2+</sup> and In<sup>3+</sup> sites were found to be mixed occupied. In the model where the Cd<sup>2+</sup> and In<sup>3+</sup> cations occupied their own site, the valence sum for Cd<sup>2+</sup> was found to be around 2.25, and the valence sum for In<sup>3+</sup> was around 3.20. After exchanging the Cd<sup>2+</sup> and In<sup>3+</sup> sites, the valence sum for In<sup>3+</sup> became 2.94 and for Cd<sup>2+</sup> was 2.43. Therefore, by valence-bond argument it is possible that Cd<sup>2+</sup> and In<sup>3+</sup> are disordered in all five sites.

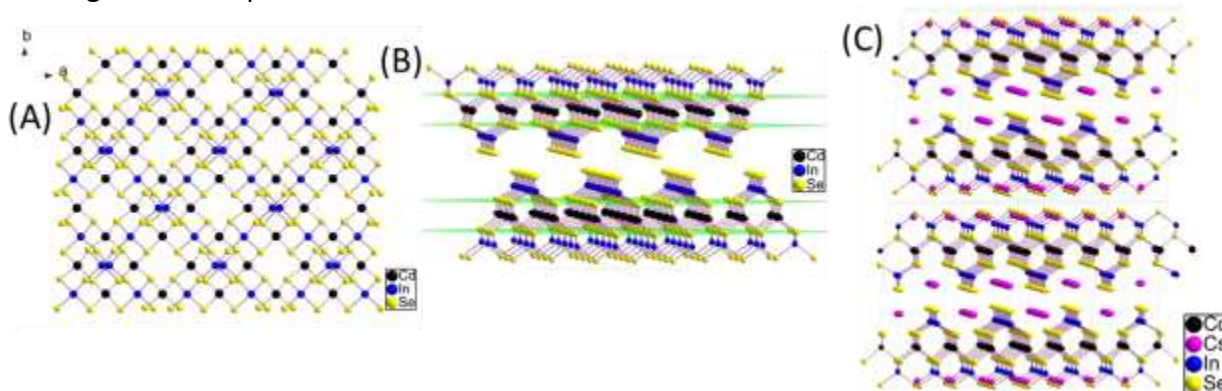


**Figure 36.** The structure of CsCdInSe<sub>3</sub>. (A) The [Cd<sub>2</sub>In<sub>2</sub>Se<sub>6</sub>] layer, the Cs atoms have been omitted for clarity; (B) The packing and configuration of the [Cd<sub>2</sub>In<sub>2</sub>Se<sub>6</sub>] layer; (C) The structure of CsCdInSe<sub>3</sub>.

Comparing the ternary CsInQ<sub>2</sub> and quaternary CsCdInQ<sub>3</sub>, there are [CdQ] layers within the [In<sub>2</sub>Q<sub>4</sub>] layers in the latter compounds. This result in a higher density for the CsCdInQ<sub>3</sub> phases compared to the corresponding CsInQ<sub>2</sub> phases. The densities of CsCdInSe<sub>3</sub> and CsInTe<sub>2</sub> are 5.089 g/cm<sup>3</sup> and 4.810 g/cm<sup>3</sup>, respectively, as shown in **Table 7,8**. Furthermore, the thickness of the [In<sub>2</sub>Q<sub>4</sub>] layer is 5.9682 Å in CsInSe<sub>2</sub> and 6.4182 Å in CsInTe<sub>2</sub>, while the thickness of the [Cd<sub>2</sub>In<sub>2</sub>Q<sub>6</sub>] layer is 8.9689 Å in CsCdInSe<sub>3</sub> and 9.5954 Å in CsCdInTe<sub>3</sub>. Because of these thicker layers the structures of CsCdInQ<sub>3</sub> are "less 2 dimensional" or "more 3 dimensional" than the ternary CsInQ<sub>2</sub>. In this context the thicker layers should possess broader electronic bands near the Fermi level and consequently higher mobility. For X-ray and γ-ray detection at room temperature, materials with high atomic number and relatively high density are needed to provide high stopping power.

$\text{CsCdInSe}_3$  ( $Z_{\text{Cs}} = 55$ ,  $Z_{\text{Cd}} = 48$ ,  $Z_{\text{In}} = 49$ , and  $Z_{\text{Se}} = 34$ ) and  $\text{CsCdInTe}_3$  ( $Z_{\text{Te}} = 52$ ) have relatively high densities, which are suitable for X-ray and  $\gamma$ -ray detection. The attenuation lengths for hard radiation of the two compounds as a function of photon energy were calculated using the atomic attenuation coefficient tabulated by NIST and are shown in **Figure 37**.  $\text{CsCdInTe}_3$  and the leading detector material  $\text{Cd}_x\text{Zn}_{1-x}\text{Te}$  (CZT) have similar attenuation lengths in most the energy range. Namely,  $\text{CsCdInSe}_3$  has a slightly larger attenuation length than CZT in the energy range above 32 keV, but has a comparable attenuation length to CZT in the lower energy range. Therefore, both  $\text{CsCdInSe}_3$  and  $\text{CsCdInTe}_3$  have relatively high stopping power.

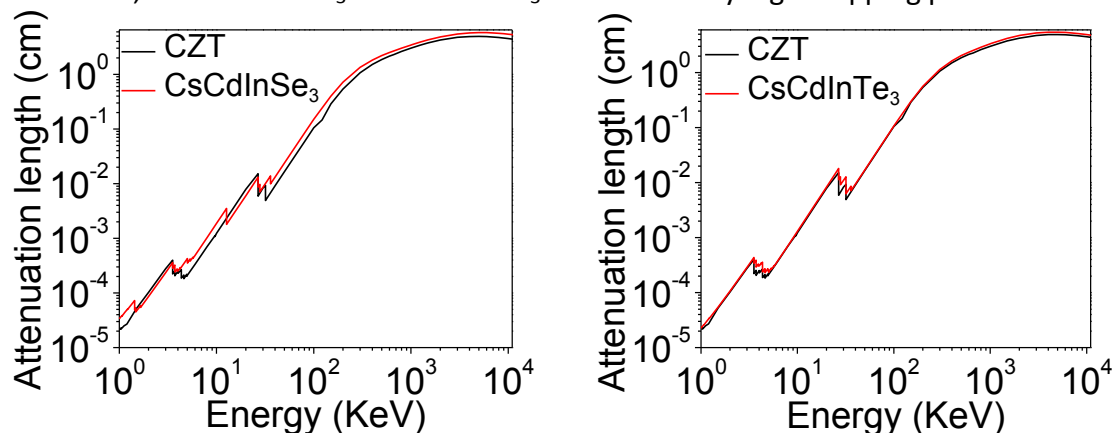


**Figure 37.** Calculated attenuation length as a function of incident photon energy in (a)  $\text{CsCdInSe}_3$ ; (b)  $\text{CsCdInTe}_3$  compared with CZT.

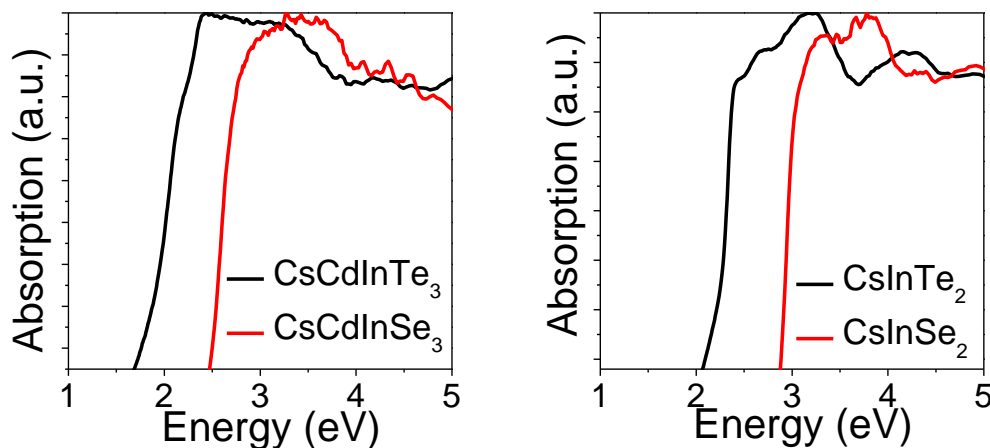


**Figure 38.** Solid state UV-Vis spectra for  $\text{CsCdInSe}_3$ ,  $\text{CsCdInTe}_3$ ,  $\text{CsInSe}_2$ , and  $\text{CsInTe}_2$  ground crystals.

#### 4.2.3. Band gap energy

The band gaps of  $\text{CsInQ}_2$  and  $\text{CsCdInQ}_3$  were determined with solid-state UV-Vis optical spectroscopy using ground crystals and the absorption spectra are shown in **Figure 38**. The band gaps of  $\text{CsInSe}_2$  and  $\text{CsInTe}_2$  are 2.81 eV and 2.16 eV, respectively, and are consistent with the light yellow ( $\text{CsInSe}_2$ ) and red ( $\text{CsInTe}_2$ ) color of the crystals. The band gaps of  $\text{CsCdInSe}_3$

(orange red) and CsCdInTe<sub>3</sub> (dark red) are 2.40 eV and 1.78 eV, respectively. To confirm the band gap, single crystals of the two compounds were selected for transmittance ( $T$ ) and reflectance ( $R$ ) spectra measurement. The absorption coefficient ( $\alpha$ ) can be calculated from  $T$  and  $R$ , the  $T$  and  $R$  were measured perpendicular to the (001) plane. A linear fit to  $\alpha^2$  versus energy gives a linear fit with direct band gap of 2.17 eV for CsCdInSe<sub>3</sub> and 1.81 eV for CsCdInTe<sub>3</sub>. The value of the band gap measured with diffuse reflectance and absorption method may be different due to the anisotropic characteristic of the plate crystals of CsCdInQ<sub>3</sub> (Q=Se, Te). A comparison of structure parameters, densities, and band gaps is summarized in **Table 8**.

**Table 8.** Comparison of cell parameters and physical properties between CsHgInS<sub>3</sub>, CsCdInSe<sub>3</sub> and CsCdInTe<sub>3</sub> with their parent ternary compounds CsInQ<sub>2</sub> (Q=S, Se, Te).

Compounds	Cell parameters				Density (g/cm <sup>3</sup> )	Band gap (eV)	$(\mu\tau)_e$ ( $\mu\tau)_h$ (cm <sup>2</sup> V <sup>-1</sup> )	
	$a$ (Å)	$b$ (Å)	$c$ (Å)	$\beta$ (°)				
CsHgInS <sub>3</sub> <sup>b</sup>	11.2503(6)	11.2531(5)	22.2884(14)	97.260(5)	5.168	2.3	$3.6 \times 10^{-5}$	$2.9 \times 10^{-5}$
CsCdInSe <sub>3</sub>	11.708(2)	11.712(2)	23.051(5)	97.28(3)	5.059	2.4	$1.18 \times 10^{-5}$	$2.74 \times 10^{-6}$
CsInTe <sub>2</sub>	12.344(3)	12.343(3)	18.059(4)	99.86(3)	4.929	2.16	N/A	
CsCdInTe <sub>3</sub>	12.523(3)	12.517(3)	24.441(5)	97.38(3)	5.195	1.78	$1.07 \times 10^{-4}$	$1.32 \times 10^{-5}$

The observed band gaps can be understood in terms of the concept of "dimensional reduction" (DR), which predicts structures of lower dimensionality to have larger energy band gaps. With the insertion of [HgS] and [CdQ] layers into the CsInQ<sub>2</sub> structure the thicker layers of CsHgInS<sub>3</sub> and CsCdInQ<sub>3</sub> are formed and constitute a "dimensional increase" relative to CsInQ<sub>2</sub>. The smaller band gaps of the quaternary CsCdInQ<sub>3</sub> compounds are more advantageous for X-ray and  $\gamma$ -ray detection than those of CsInQ<sub>2</sub>, since it ensures a lower electron-hole pair average ionization energy, which provides higher-resolution radiation spectroscopy.

#### 4.2.4. Electronic Structure

The electronic band structures of CsCdInQ<sub>3</sub> (Q=Se, Te), shown in **Figure 39**, reveal a direct band gap of 1.53 eV (I) and 1.39 eV (II) at the  $\Gamma$  point, which are underestimated compared to the experimental band gaps of 2.40 eV and 1.78 eV. Both calculations are performed on the level of semi-local approximation like GGA, and the gaps are known to be underestimated compared to experimental values. More exact methods are needed to predict the correct band gap. The conduction bands of the two compounds are quite dispersive along the  $\Gamma$ -X and  $\Gamma$ -Y directions, which should result in a small effective mass for electron carriers. On the other hand, the valence bands near the Fermi level are less dispersive compared to the conduction bands, especially along the  $\Gamma$ -Z direction where the valence bands of both compounds are almost flat. This is the direction that is perpendicular to the layers and the flat bands can be understood by the lack of covalent bonds along this direction.

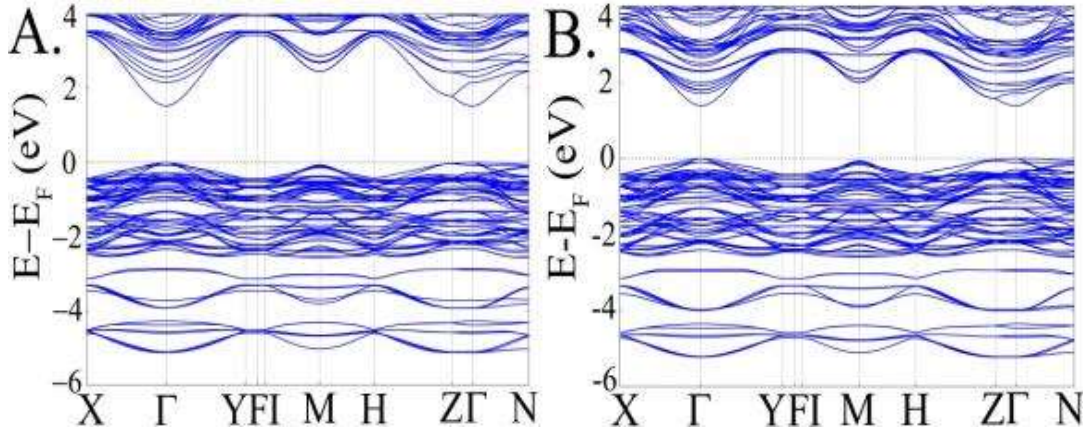


**Figure 39.** Calculated electronic band structure for (A) CsCdInSe<sub>3</sub> and (B) CsCdInTe<sub>3</sub>.

In order to better assess the carrier properties, we calculated effective masses near the conduction and valence band edges, since the mobility is inversely proportional to the effective mass. In CsCdInSe<sub>3</sub>, the effective mass is  $0.189m_0$  for electrons and  $0.811m_0$  for holes, while in CsCdInTe<sub>3</sub> the values are  $0.173m_0$  and  $0.630m_0$ , respectively. These values are comparable to CdTe, which are  $0.11m_0$  for electrons and  $0.73m_0$  for holes. Interestingly, the calculations suggest that CsCdInTe<sub>3</sub> has a smaller hole effective mass than CdTe, so it could have higher hole mobility.

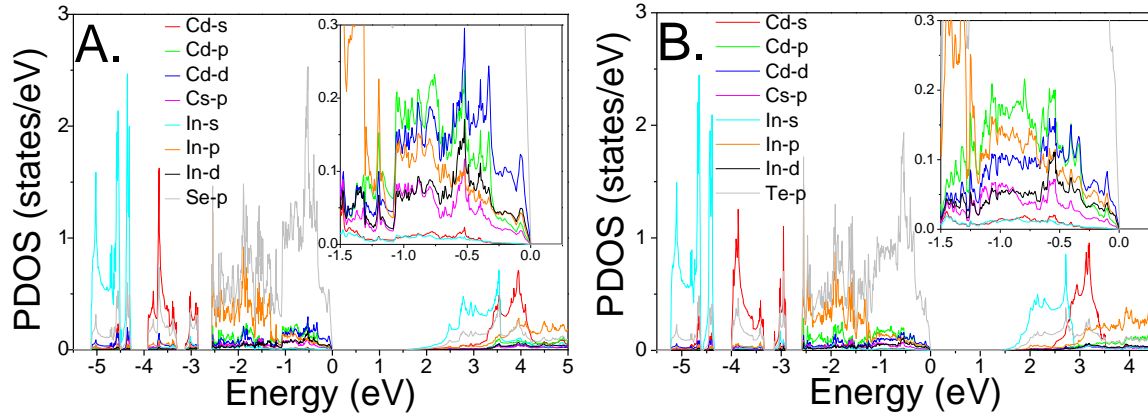


**Figure 40.** Projected density of states plots (per eV per unit cell) for (A) CsCdInSe<sub>3</sub> and (B) CsCdInTe<sub>3</sub>.

From projected density of states (DOS) calculations, shown in **Figure 40**, we can see that valence band maxima (VBM) are mainly composed of Se(Te) 4p(5p)-orbitals. Cd 4d-orbitals contribute to a much lesser extent to the VBM and the conduction band minima (CBM) consist of hybridization bands made up of Se(Te) 4p(5p)-orbitals and In 5s-orbitals.

#### 4.3. Resistivity and Photoconductivity

The resistivity of single crystals of CsCdInSe<sub>3</sub> and CsCdInTe<sub>3</sub> was measured using a two probe method. Carbon paste was used to put electrodes onto the crystals but a non-ohmic behavior was observed for CsCdInTe<sub>3</sub>. Silver paste was also tried, but it was observed to react with the crystals and did not give repeatable results. The current-voltage characteristics of the single crystals were measured both parallel and perpendicular to the (001) plane and are shown

in **Figure 41**. The I-V curves of CsCdInTe<sub>3</sub> deviate from linearity at low bias ( $\sim \pm 3$  V), which is normal behavior for a Schottky contact barrier and has often been found in commercially available CZT detectors. Both of the quaternary compounds have resistivities that are highly anisotropic, which is in agreement with their layered structure. CsCdInSe<sub>3</sub> has a relatively high resistivity of 4.2 G $\Omega$ .cm perpendicular to the (001) plane and 28 M $\Omega$ .cm parallel to the (001) plane, with a ratio between the two directions of about 150. The resistivity of CsCdInTe<sub>3</sub> is  $\sim 190$  M $\Omega$ .cm perpendicular to the (001) plane and 1.5 M $\Omega$ .cm parallel to the (001) plane, with a ratio of about 120. The larger band gap of CsCdInSe<sub>3</sub> relative to CsCdInTe<sub>3</sub> accounts for its higher resistivity.

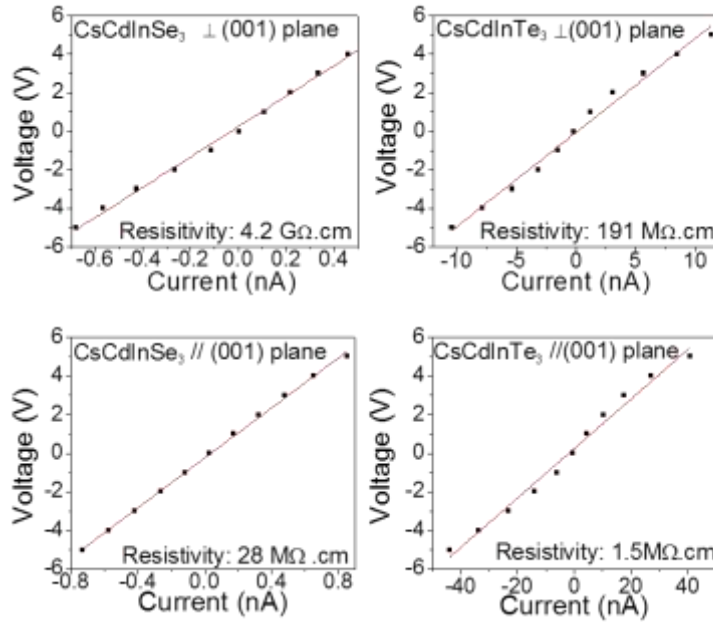


**Figure 41.** Current-voltage characteristics for the CsCdInSe<sub>3</sub> and CsCdInTe<sub>3</sub> crystals, For CsCdInTe<sub>3</sub>, the points near the  $\pm 3$  V are off the fitted linear line due to the Schottky barrier behavior.

The figure of merit used to predict the response of a detector material to X-ray and  $\gamma$ -ray radiation is the  $\mu\tau$  product of both the electron and hole carriers, which is related to the drift length  $\lambda = \mu\tau E$  ( $E$  is the electric field). The carriers (electrons and holes) created by the absorbed ionizing radiation should have a large enough drift length  $\lambda$  to reach the electrodes, before they recombine or get trapped by defects. Therefore, a higher  $\mu\tau$  product results in a higher response to radiation readout. Photoconductivity measurements using a visible light diode laser (405 nm) were performed to evaluate the  $\mu\tau$  product of both carriers. This method has been adopted previously and has given equivalent results as when using X-rays and  $\gamma$ -rays. Single crystals of CsCdInSe<sub>3</sub> and CsCdInTe<sub>3</sub> cleaved directly from the as grown ingots with intact natural (001) faces were illuminated by the laser, the wavelength of which is shorter than the absorption edge of either compound and is strongly absorbed. Under a constant laser intensity, the photocurrent  $I$  depends on the bias voltage  $V$ , which can be modeled by the Many eq (1) (see above).



**Figure 42** shows the photoconductivity curves for CsCdInSe<sub>3</sub> and CsCdInTe<sub>3</sub> crystals. Fitting the photocurrent data to equation (1), both the  $\mu\tau$  products and surface recombination velocities  $s/\mu$  were determined. For CsCdInSe<sub>3</sub> the measured values are  $(\mu\tau)_e = 1.18 \times 10^{-5} \text{ cm}^2\text{V}^{-1}$  and  $(\mu\tau)_h = 2.74 \times 10^{-6} \text{ cm}^2\text{V}^{-1}$ , while for CsCdInTe<sub>3</sub> the products are  $(\mu\tau)_e = 1.07 \times 10^{-4} \text{ cm}^2\text{V}^{-1}$  and  $(\mu\tau)_h = 1.32 \times 10^{-5} \text{ cm}^2\text{V}^{-1}$ . The values for CsCdInSe<sub>3</sub> are smaller than CsCdInTe<sub>3</sub>, which is consistent with the theoretical results that the calculated effective mass of the electrons in I to be higher than in II.

The  $\mu\tau$  product of CsCdInTe<sub>3</sub> is comparable to the well-known detector material  $\alpha\text{-HgI}_2$  which has  $(\mu\tau)_e = 1 \times 10^{-4} \text{ cm}^2\text{V}^{-1}$  and  $(\mu\tau)_h = 4 \times 10^{-5} \text{ cm}^2\text{V}^{-1}$ . The  $\mu\tau$  product of CsCdInSe<sub>3</sub> is higher than that of PbI<sub>2</sub> ( $(\mu\tau)_e = 8 \times 10^{-6} \text{ cm}^2\text{V}^{-1}$  and  $(\mu\tau)_h = 9 \times 10^{-7} \text{ cm}^2\text{V}^{-1}$ ), another well investigated semiconductor for hard radiation detection. The  $\mu\tau$  products for electrons however are lower than those of CZT, the leading material for X-ray and  $\gamma$ -ray detection at room temperature, which has  $(\mu\tau)_e = 4.5 \times 10^{-2} \text{ cm}^2\text{V}^{-1}$  and  $(\mu\tau)_h = 1 \times 10^{-4} \text{ cm}^2\text{V}^{-1}$ . The carrier mobility-lifetime products of CsCdInTe<sub>3</sub> should reach higher values if better crystal quality could be obtained by further optimizing growth conditions.

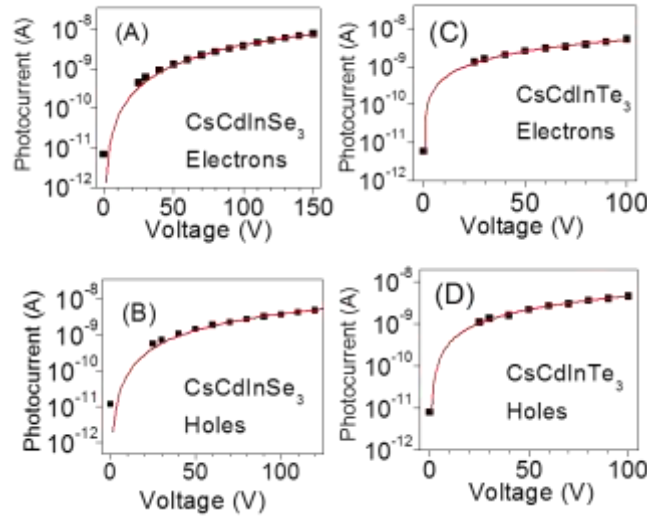


**Figure 42.** Photocurrent versus applied voltage for (A) electrons and (B) holes for CsCdInSe<sub>3</sub>; (C) electrons and (D) holes for CsCdInTe<sub>3</sub>.

#### 4.4. Theory component of the research

##### Formation of native defects in the gamma-ray detector material, Cs<sub>2</sub>Hg<sub>6</sub>S<sub>7</sub>

Semiconductor devices detecting hard radiation such as x-rays and  $\gamma$ -rays have been receiving much attention owing to their broad applications in scientific research, medical diagnostics, and homeland security. However, the search for new detector materials is challenging since they should satisfy multiple criteria: high atomic number, high density, optimized band gap, and high mobility-carrier lifetime ( $\mu\tau$ ). In a recent study, we presented an effective screening strategy, so called “dimensional reduction”, and from the strategy, we predicted that Cs<sub>2</sub>Hg<sub>6</sub>S<sub>7</sub> can be a promising candidate material for  $\gamma$ -ray detectors.

In spite of its superior bulk properties for a good  $\gamma$ -ray detector material, the performance of Cs<sub>2</sub>Hg<sub>6</sub>S<sub>7</sub> applications can be limited owing to a native defect degrading  $\mu\tau$  or increasing dark

current. Since the formation of a native defect can be controlled by changing growth conditions, understanding the relationship between growth conditions and the properties of native defects is crucial. By using first-principles calculations, we carried out formation energy calculations for all possible native defects of  $\text{Cs}_2\text{Hg}_6\text{S}_7$  and we estimated their concentration as a function of the growth condition. Based on the calculated results, we suggest optimal growth conditions to decrease detrimental defects in  $\text{Cs}_2\text{Hg}_6\text{S}_7$ .

**Calculation details:** To investigate electronic and thermodynamic properties of native defects of  $\text{Cs}_2\text{Hg}_6\text{S}_7$ , we performed first principles DFT total energy calculation for super-cells including a point defect. We used a 1x1x4 super-cell which accommodates 120 atoms. Based on DFT total energy calculations, we determined defect formation energies ( $\Delta H_{D,q}$ ) using the formula,

$$\Delta H_{D,q} = (E_{D,q} - E_H) + qE_F + \sum n_\alpha \mu_\alpha, \quad \text{eq(4)}$$

where  $E_{D,q}$  and  $E_H$  are total energies of the system including a defect  $D$  with charge  $q$  and pristine system, respectively,  $E_F$  is the Fermi level,  $n_\alpha$  is the number of atoms of  $\alpha$  removed from the super-cell to the reservoir of  $\alpha$ , and  $\mu_\alpha$  is the chemical potential of the reservoir of  $\alpha$ . The total energies of super-cells were calculated using the projector augmented-wave method implemented in the “*Vienna Ab-initio Simulation Package*” (VASP) code. For the exchange-correlation functional, we employed the generalized gradient approximation within the Perdew-Burke-Ernzerhof formalism. All defect configurations were fully relaxed. In order to correct the finite cell effect, we calculated correction terms of the band filling effect and image charge. Based on the calculated defect formation energies, the concentration of intrinsic defects and carrier densities were calculated self-consistently as a function of temperature and chemical environment.

**Formation of native defects in  $\text{Cs}_2\text{Hg}_6\text{S}_7$ :** We considered 3 types of possible native defects: vacancy, anti-site, and interstitial defects. As shown in **Figure 43(a)**, 6 vacancy defects emerge from Cs atom ( $V_{\text{Cs}}$ ), two different Hg atoms ( $V_{\text{Hg1}}$  and  $V_{\text{Hg2}}$ ), and three types of Sulfur atoms ( $V_{\text{S1}}$ ,  $V_{\text{S2}}$ , and  $V_{\text{S3}}$ ). We also considered anti-site defects on cation sites: Hg defect replacing Cs atom ( $\text{Hg}_{\text{Cs}}$ ) and Cs defect replacing Hg atom ( $\text{Cs}_{\text{Hg1}}$  and  $\text{Cs}_{\text{Hg2}}$ ). And we considered interstitial defects which accommodate the large empty space denoted by A in **Figure 43(a)** ( $\text{Cs}_i$ ,  $\text{Hg}_i$ , and  $\text{S}_i$ ).

In order to understand the electronic and thermodynamic properties of those 12 native defects, we carried out formation energy calculations following Eq. 1. In **Figure 43(c)** and (d), we presented the calculated formation energies under the two extreme growth conditions, Cs-rich/S-poor limit and Cs-poor/S-rich limit, which are denoted by blue and red circles in **Figure 43(b)**. In the Cs-rich/S-poor limit,  $V_{\text{S}}$  are the most dominant defects.  $V_{\text{S1}}$  and  $V_{\text{S2}}$ , which correspond to the two lowest red dotted-lines, are electrically inactive defects. However,  $V_{\text{S3}}$ , denoted by red solid-lines, has a deep donor level due to the large distortion of the 2+ charged configuration. It is well known that such a deep level can cause charge trapping or recombination of electrons and holes, which decreases the  $\mu\tau$  value and results in degrading the performance of the  $\gamma$ -ray detector. Therefore,  $V_{\text{S3}}$  can be considered as one of the detrimental defects.



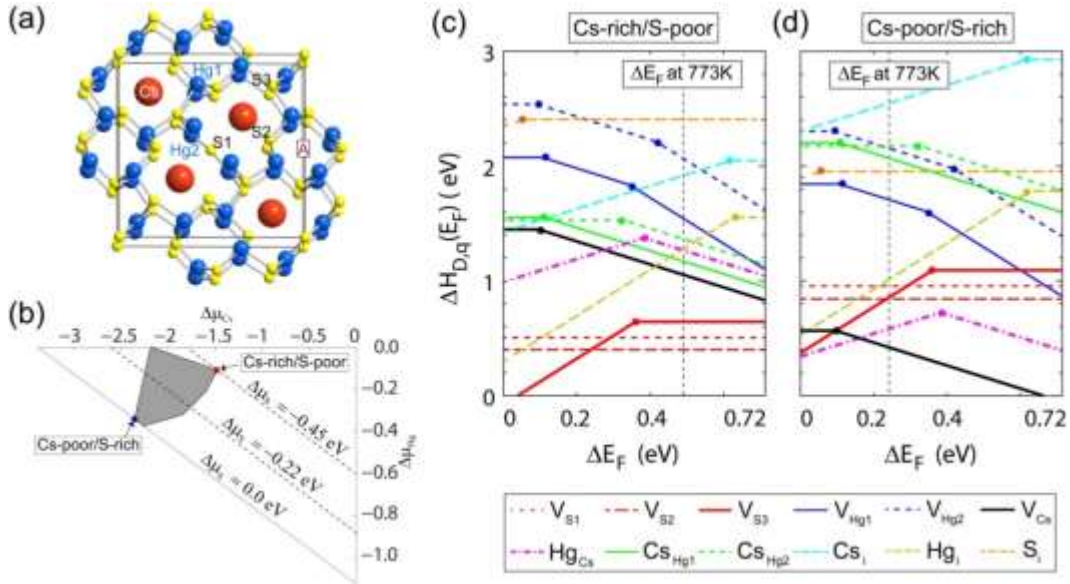


**Figure 43** (a) Crystal structure of  $\text{Cs}_2\text{Hg}_6\text{S}_7$ , (b) Thermodynamic stability map of  $\text{Cs}_2\text{Hg}_6\text{S}_7$ , and formation energies of native defects under (c) Cs-rich/S-poor limit and (d) Cs-poor/S-rich limit conditions. In panel (a), Cs, Hg, and S atoms are represented by red, blue, and yellow spheres, respectively. In panel (b), the grey area indicates the region where  $\text{Cs}_2\text{Hg}_6\text{S}_7$  can be stabilized. Blue and red dots represent Cs-poor/S-rich limit and Cs-rich/S-poor limit conditions, respectively. In panel (c) and (d), each line corresponds to a native defect, denoted in the lower panel. The vertical dotted lines in (c) and (d) indicate the equilibrium Fermi level at 773 K.

In the Cs-poor/S-rich limit,  $\text{Hg}_{\text{Cs}}$  and  $V_{\text{Cs}}$  are the most dominant native defects. As shown in **Figure 43(d)**,  $\text{Hg}_{\text{Cs}}$  forms a deep level similar to that of  $V_{\text{S3}}$ , so this defect can also be considered as detrimental as well. On the other hand,  $V_{\text{Cs}}$  forms a shallow acceptor level at 0.1 eV above the valence band maximum (VBM). Owing to the low formation energy and the low ionization energy of the  $V_{\text{Cs}}$ , the equilibrium  $\Delta E_F$  moves down to the VBM. As shown in **Figure 43(d)**, the equilibrium  $\Delta E_F$  equals 0.24 eV above the VBM at the experimental growth temperature (= 773K). As a result, hole-carriers are released from  $V_{\text{Cs}}$  into the valence band and  $\text{Cs}_2\text{Hg}_6\text{S}_7$  becomes a p-type semiconductor.

From the formation energy of the defects, we evaluated the concentration of defects and the carrier density as a function of the chemical environment and growth temperature. In **Figure 44(a)(b)**, the concentrations of two detrimental defects,  $V_{\text{S3}}$  and  $\text{Hg}_{\text{Cs}}$  are presented, at the experimental growth temperature 773 K. In the case of  $V_{\text{S3}}$  the concentration is predicted to be the minimum value ( $8.8 \times 10^{14} \text{ cm}^{-3}$ ) at point A and the maximum value ( $3.2 \times 10^{17} \text{ cm}^{-3}$ ) at point B, as shown in **Figure 44(a)**. However, the concentration of  $\text{Hg}_{\text{Cs}}$  is minimized ( $2.4 \times 10^{13} \text{ cm}^{-3}$ ) at point B and maximized ( $2.0 \times 10^{18} \text{ cm}^{-3}$ ) at point C, as shown in **Figure 44(b)**. Thus, growth conditions to minimize concentration of  $V_{\text{S3}}$  and  $\text{Hg}_{\text{Cs}}$  cannot be satisfied simultaneously.

**Figures 44 (c) and 44 (d)** present the net carrier density,  $N = N_{\text{electron}} + N_{\text{hole}}$ , of  $\text{Cs}_2\text{Hg}_6\text{S}_7$  at 300K with fixed concentration of defects at 773K and 900 K, respectively. From the calculation, we found several distinct features for  $N$ . First, as the growth condition changes from the Cs-rich/S-poor limit (point B) to the Cs-poor/S-rich limit (point D), the major carrier changes from electron to hole because the dominant defect changes from  $V_{\text{S}_3}$  to  $V_{\text{Cs}}$ . This result indicates that in a certain range of chemical potentials, both carrier densities can be suppressed simultaneously. Such conditions are found in the white-colored region where  $N < 10^{12} \text{ cm}^{-3}$  in **Figures 44 (c) and 44 (d)**. Second,  $N$  changes mainly depending on  $\mu_{\text{Cs}}$ . This can be explained by the relationship between the equilibrium position of  $\Delta E_F$  and  $\mu_{\text{Cs}}$ . Due to the lower thermal ionization energy of  $V_{\text{Cs}}$  than that of other electron donor defects,  $V_{\text{S}_3}$  and  $\text{Hg}_{\text{Cs}}$ , the equilibrium  $\Delta E_F$  highly depends on  $\mu_{\text{Cs}}$ . Accordingly,  $N$  also highly depends on  $\mu_{\text{Cs}}$ . Additionally, **Figure 44(c),(d)** show the dependence of  $N$  on the growth temperature. The maximum value of  $N$  increases at higher growth temperature, but the effect on the minimum region is negligible.

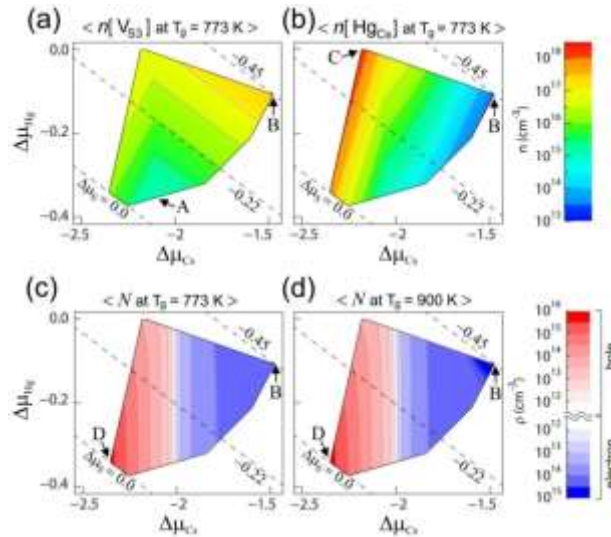


**Figure 44** The calculated concentrations of defects and carrier densities as a function of the chemical potentials in the thermodynamic stability presented in Fig. 13 (b). (a) and (b) present the concentrations of  $V_{\text{S}_3}$ , and  $\text{Hg}_{\text{Cs}}$  at 773 K; (c) and (d) show the electron- and hole-carrier densities at 300K with fixed defect concentrations at 773K and 900 K.

Based on these results, we can determine the optimal growth condition of  $\text{Cs}_2\text{Hg}_6\text{S}_7$  for  $\gamma$ -ray detector materials. The experimentally measured resistivity of  $\text{Cs}_2\text{Hg}_6\text{S}_7$  is as low as  $2 \times 10^6 \Omega \text{cm}$ , while the  $\mu\tau$  values are comparable with those of CZT which is the most widely used  $\gamma$ -ray detector material. Thus, the primary requirement for  $\text{Cs}_2\text{Hg}_6\text{S}_7$  is to achieve the high resistivity. As shown in **Figure 44(c),(d)**, the growth conditions corresponding to the white-colored region minimizes carrier densities. Accordingly, this growth condition can be the optimal growth condition for  $\text{Cs}_2\text{Hg}_6\text{S}_7$  for higher resistivity. However, the growth condition reducing concentrations of  $V_{\text{S}_3}$  or  $\text{Hg}_{\text{Cs}}$  is not perfectly compatible with the optimal growth conditions for the high resistivity. Nevertheless, our results show that we can control chemical potentials to decrease concentrations of  $V_{\text{S}_3}$  and  $\text{Hg}_{\text{Cs}}$  within the conditions of the minimum  $N$ , and can enhance further the performance of the  $\gamma$ -ray detector. For instance, under the optimal values

of  $\mu_{Cs}$  for the high resistivity, we can decrease the partial pressure of Hg to the value that corresponds to  $\mu_{Hg}$  near point A in **Figure 44(a)**. Then, this condition leads to decreasing concentrations of  $V_{S3}$  and  $Hg_{Cs}$  in appropriate levels.

### 5.0. Photo-induced current transient spectroscopy of semi-insulating single crystal $Cs_2Hg_6S_7$

We also investigated the defect levels in the semi-insulating semiconductor  $Cs_2Hg_6S_7$  by the current transient spectroscopy light to photoexcite carriers. The photoinduced current transient spectroscopy (PICTS) technique is well-suited for defect detection in semi-insulating materials. The important deep-level defect parameters including trap ionization energy, capture cross section, concentration, and recombination rate can be obtained. It has been previously used to detect deep level defects in high-resistivity semiconductors including bulk CdS and CdTe [Yoshie O and Kamihara M 1983 *Jpn. J. Appl. Phys.* **22** 621; Yoshie O and Kamihara M 1983 *Jpn. J. Appl. Phys.* **22** 629]. Although PICTS measurement does not allow one to directly quantify the trap concentration, the spectra can be used to obtain qualitative information on the deep trap concentration. In this study, we measured a series of defect levels in undoped semi-insulating  $Cs_2Hg_6S_7$  over the energy range of 0.1 to 1.0 eV. Identification and subsequent control of these defects should lead to semi-insulating semiconductors with higher resistivity and larger  $\mu\tau$  products, resulting in high efficiency radiation detectors that operate at room temperature.

The PICTS technique can be used to identify both the acceptor and donor traps. In PICTS the device is illuminated with light pulses of definite duration. Above bandgap light creates electron-hole pairs in a region underneath the semi-transparent Au metal electrode. When bias is applied to the contacts, electrons or holes are transported through a short distance into the bulk and trapped by empty centers. A positive bias applied to the Au contact injects only holes into the bulk of the crystal and hence the transient signal is due to the hole current. Similarly, a negative bias applied to the Au electrode injects electrons and produces transient due to detrapping of captured electrons.

#### Experiment details for the PICTS study

**Growth of  $Cs_2Hg_6S_7$  single crystals:**  $Cs_2Hg_6S_7$  polycrystals were first synthesized from high-purity elements by reacting appropriate stoichiometric ratios of  $Cs_2S$  with  $\beta$ -HgS. Single crystals were subsequently grown by the Bridgman method using sealed quartz tubes as crucibles. The grown ingots were analyzed by Laue back-scattered reflection to verify their single crystalline nature. The dimensions of the  $Cs_2Hg_6S_7$  single crystal (HL-2-4-1) used in this study are  $\sim 5 \times 4 \times 2$  mm<sup>3</sup>. The crystals are semi-insulating. The measured room temperature resistivity of the crystal cut perpendicular to the growth direction is of the order of  $1 \times 10^8$   $\Omega$ -cm. Ohmic contacts were made by vacuum depositing semi-transparent 80 nm gold electrodes on the top and bottom surfaces of the crystals in a parallel plate configuration. The quality of the contacts was assessed from the I-V characteristics, which is linear at room temperature.

**Schematic of the PICTS setup:** The PICTS apparatus consists of a pulsed laser, a high gain low noise Keithley 428 current amplifier, a digital oscilloscope, and a liquid nitrogen cryostat. The schematic of the system is shown in **Figure 45**. The sample is placed in the vacuum cryostat with an optically transparent entrance window. A thermocouple is attached to the sample for monitoring its temperature, and also connected to a temperature controller. A heater attached

to the sample holder enables temperature control from 77 to 325 K. The excitation light source is a nitrogen pulsed laser with a wavelength of 337 nm (above band-gap excitation). The laser has a pulse width of 4 ns and an output power large enough to saturate the traps in the semiconductor. A DC voltage of +75 V was applied to bias the sample. The crystal was illuminated through the semitransparent Au electrode. Pulsed light excitation results in a current transient signal that is amplified using the Keithley 428 current amplifier. The current is converted into a voltage signal using a 50  $\Omega$  resistor and the signal is fed to the oscilloscope. The trigger signal for the oscilloscope is generated by the nitrogen-pulsed laser supply. The detection of the transient signal is carried out at temperatures in the range of 80 – 310 K with a step of 10 K during the heating of the sample with a rate of 2K/min. The transient curves were sampled at 2000 equally spaced points ( $\Delta t = 50 \mu s$ ).

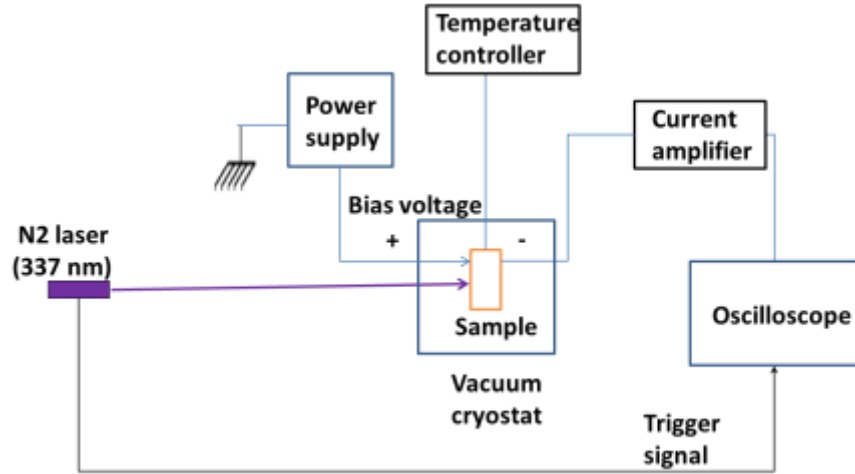


**Figure 45.** Schematic of PICTS setup. A nitrogen pulsed laser was used as the excitation source.

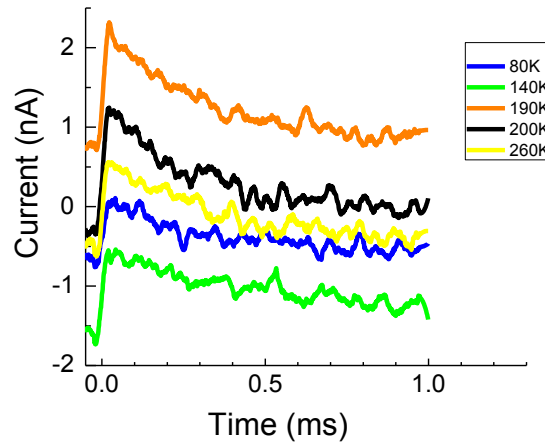


**Figure 46.** Transient current versus time for different temperatures. For the 24 datasets observed, only five are shown. Transient current was measured from 80 K to 310 K. Datasets were collected at 10 K intervals.

To calculate the trap parameters of thermal activation energy and capture cross-section, the current transient is analyzed using the normalized double gate method.<sup>Error! Bookmark not defined.</sup> In

the double gate PICTS, two gate times  $t_m$  and  $t_n$  are selected ( $t_n > t_m$ ) on the transient current curve. Here the PICTS response  $S(t)$  is given by:

$$S(t) = I(t_m) - I(t_n) \quad (1)$$

where  $I(t)$  is the transient current. The transient current after cessation of the pulse is given as [Rakhshani A E, Khan W I, and Mathew X 1996 *Phys. Stat. Sol. B* **196** 163; Brasil M J S P, and Motisuke P 1990 *J. Appl. Phys.* **68** 3370]

$$I(t) = K e_i e^{-e_i t} \quad (2)$$

where  $e_i$  is the emission rate ( $s^{-1}$ ) from trap  $i$  with an ionization energy  $E_i$ . The prefactor  $K$  depends on the device parameters and applied bias. The emission rate  $e_i$  is given by

$$e_i (s^{-1}) = H T^2 \sigma_i e^{E_i/kT} \quad (3)$$

where  $\sigma_i$  is the capture cross-section of the trap in  $cm^2$ ,  $T$  is the temperature and the constant  $H$  is related to the density of states and trap degeneracy factor. The PICTS signal has a maximum when

$$\frac{dS}{de_i} \times \frac{de_i}{dT} = 0 \quad (4)$$

Using the condition in Eq. (4), the relations between  $e_i$ ,  $t_m$ , and  $t_n$  for the maxima of the PICTS spectra are given by:

$$\left(t_n - \frac{1}{e_i}\right) = \left(t_m - \frac{1}{e_i}\right) e^{(t_n - t_m)e_i} \quad (5)$$

Thus the emission coefficients ( $e_i$ ) of a trap for different pairs of gate positions  $t_n$  and  $t_m$  are obtained using Eqn. (5). For a given trap, a graph of  $\ln(T^2 \tau_i)$  vs.  $1/T$  is plotted where  $\tau_i = 1/e_i$ . The temperature  $T$  corresponds to the temperature that yields a maximum PICTS signal for each pair of  $t_n$  and  $t_m$ . From Eq. (3) the log of the emission rate is linear with a slope  $E_i/k$ , where  $E_i$  is the trap ionization energy,  $k$  is Boltzmann constant. The intercept with the  $1/T$  axis is  $-\ln(H\sigma)$ .

**Results and discussion for the PICTS study:** Figure 46 shows the observed transient current signal versus time for different temperatures for semi-insulating  $Cs_2Hg_6S_7$ . Datasets were collected between 80 and 310 K with 10 K interval. Of the 24 temperatures in the dataset, only five are shown. The typical PICTS signal versus temperature for the double gate method of a semi-insulating  $Cs_2Hg_6S_7$  crystal is shown in Figure 47. Sampling gate 1 is chosen at 100  $\mu s$ , 200  $\mu s$ , 300  $\mu s$ , 400  $\mu s$ , 500  $\mu s$ , and gate 2 at 600  $\mu s$ , 700  $\mu s$ , 800  $\mu s$ , 900  $\mu s$ , 1000  $\mu s$ , respectively. Five distinct traps labeled A, B, C, D, and E are observed. The temperature dependence of the thermal emission rate for traps A, B, C, D, and E are shown in Figure 48 for  $\ln(T^2 \tau_i)$  vs.  $1000/T$  diagram for each peak, respectively. The thermal activation energy and capture cross-section are calculated from the slope and intercept of the linear fitting. In order to determine cross section  $\sigma_i$ , the prefactor  $H$  is calculated by using the simulated values of the carrier density ( $10^{12} cm^{-3}$  for hole, and  $10^{15} cm^{-3}$  for electron) and trap degeneracy factor (value of 2). The values of the thermal activation energy  $E_i$  of the traps and the effective capture cross section  $\sigma_i$  are listed in Table 9 together with the temperature range in which the trap is detected. The measured defect energies are 0.17, 0.10, 0.11, 0.21, 1.21 eV, respectively for peaks A, B, C, D, and E. Three of shallow levels of 0.10, 0.11, 0.21 eV are consistent with results from prior

photoluminescence and photoconductivity measurements [Peters J A, Cho N K, Liu Z, Wessels B W, Li H, Androulakis J, and Kanatzidis M G 2012 *J. Appl. Phys.* **112** 063702].

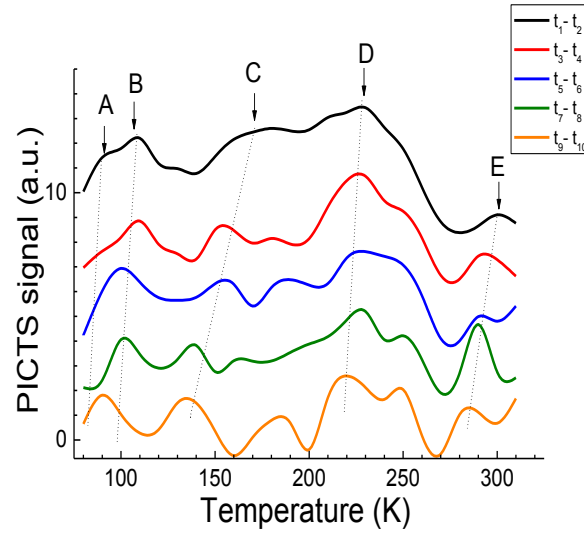


**Figure 47.** PICTS signal versus temperature for the two gate method (shifted water fall drawing). Gate 1 was chosen at 100  $\mu$ s, 200  $\mu$ s, 300  $\mu$ s, 400  $\mu$ s, 500  $\mu$ s, and gate 2 at 600  $\mu$ s, 700  $\mu$ s, 800  $\mu$ s, 900  $\mu$ s, 1000  $\mu$ s, respectively.

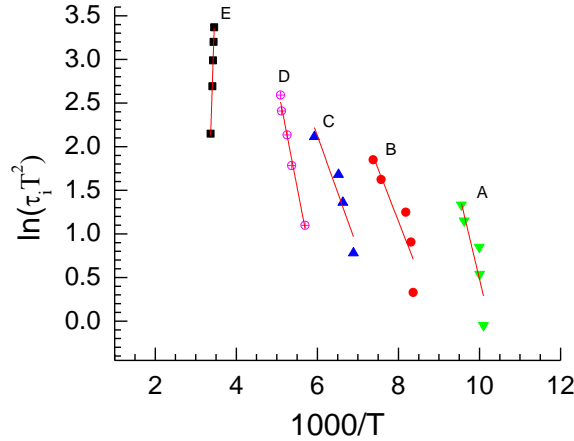


**Figure 48.**  $\ln(T^2\tau_i)$  vs.  $1000/T$  for five different peaks A, B, C, D and E. The thermal activation energy and capture cross-section are derived from the slope and intercept of the linear fitting.

**Table 9** lists the four shallow levels and one deep level and their corresponding energies and cross sections. **Table 10** compares energies of defects using three different measurement techniques including: PICTS, photoluminescence spectroscopy, and photocurrent spectroscopy. It should be noted that the peak A at 0.17 eV did not follow the normal trend of the higher the defect activation energy the higher the peak temperature. Presumably due to its small capture cross section of  $1 \times 10^{-24} \text{ cm}^2$ . **Figure 49** shows the trap energy assignment of  $\text{Cs}_2\text{Hg}_6\text{S}_7$  as corresponding to the peaks of A, B, C, D and E.

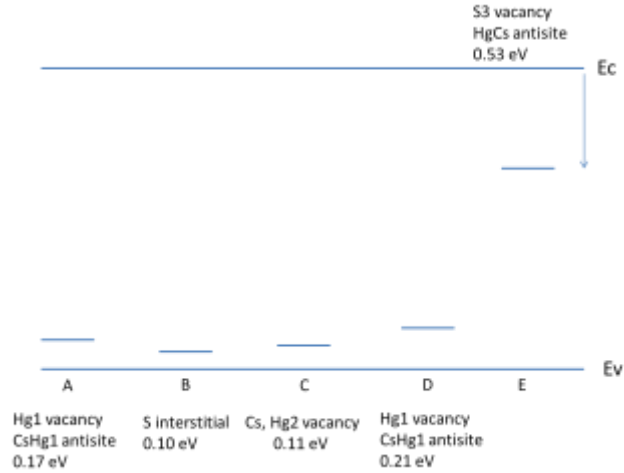


**Figure 49.** Plot of assigned trap energy levels as compared to references 9 and 10. Peaks B, C, and D were observed by PL and PC previously.  $E_c$  = energy of conduction band;  $E_v$  = energy of valence band.

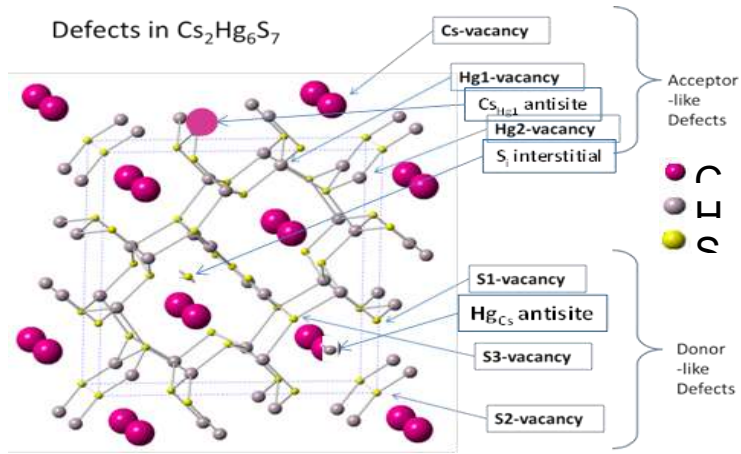


**Figure 50.** Schematic diagram showing the types of defects in a  $\text{Cs}_2\text{Hg}_6\text{S}_7$  crystal.

DFT calculations discussed above indicate that there are a number of shallow levels above the valence band edge. The first five of them are: sulfur interstitial  $\text{S}_i$ , Cs vacancy [ $\text{V}_{\text{Cs}}$ ], mercury vacancies including [ $\text{V}_{\text{Hg1}}$ ], [ $\text{V}_{\text{Hg2}}$ ], and mercury antisite  $\text{Cs}_{\text{Hg1}}$ . These are all acceptors with energies of 0.10, 0.11, 0.17, 0.21 eV. The energy difference between [ $\text{V}_{\text{Cs}}$ ] and [ $\text{V}_{\text{Hg2}}$ ] is negligible. Calculation also indicates there are two deep levels, [ $\text{V}_{\text{S3}}$ ] and  $\text{Hg}_{\text{Cs}}$ , though their energy difference is minimal. By comparing the trap energies obtained from DFT calculation with those obtained by PICTS measurements, we tentatively assign the peaks. By referring to **Figure 2(a)**, the two mercury atoms as well as the three sulfur atoms each has different neighboring atom configurations and therefore the assignment of peaks is linked to specific atoms. There are four acceptor levels, namely, peak B (sulfur interstitial), peak C (Cs or  $\text{Hg}_2$  vacancy), peaks A and D ( $\text{Hg}_1$  vacancy,  $\text{Cs}_{\text{Hg1}}$  antisite defect), and one donor level at peak E (S-vacancy or  $\text{Hg}_{\text{Cs}}$ -antisite, defect closer to the conduction band than the valence band). Thus as shown in **Figure 50** there are five acceptor-like defects and four donor-like defects present in  $\text{Cs}_2\text{Hg}_6\text{S}_7$ . The acceptor

levels are all energetically shallow whereas the donor levels are both shallow (S1 and S2 vacancies) and deep (S3 vacancy) levels.

The PICTS study showed that from the spectral measurements a series of acceptor levels at 0.10, 0.11, 0.17, and 0.21 eV, respectively, are observed in the undoped material. A deep level of 1.21 eV, a donor level 0.53 eV below the conduction band, is also observed, and it is in agreement with the first-principles DFT calculations. The peaks are attributed to native defects namely, sulfur interstitial (0.10 eV), Cs or Hg vacancies (0.11 eV), Hg vacancies (0.17 eV), and  $\text{Cs}_{\text{Hg}}$  antisite defects (0.21 eV). The deep level of 0.53 eV is tentatively attributed to donor defects, either a S-vacancy or less likely  $\text{Hg}_{\text{Cs}}$ -antisite defect. Identification and subsequent control of these defects should lead to semi-insulating semiconductors with higher resistivity and larger mobility-lifetime products, resulting in high efficiency,  $\gamma$ -radiation detectors that operate at room temperature.

**Table 9.** Parameters of defect centers in  $\text{Cs}_2\text{Hg}_6\text{S}_7$ . The energies are with respect to the valence band edge.

Trap	$\Delta T$ (K)	E (eV)	$\sigma$ ( $\text{cm}^2$ )	Trap type
A	80-100	0.17	$1.0 \times 10^{-24}$	Acceptor
B	115-140	0.10	$1.1 \times 10^{-20}$	Acceptor
C	150-200	0.11	$2.4 \times 10^{-20}$	Acceptor
D	210-270	0.20	$2.0 \times 10^{-22}$	Acceptor
E	280-310	1.2	--	Donor

**Table 10.** Comparison of energies (unit eV) of defects from different methods  
Explain the different acronym such as **PEAK...**

PICTS	0.10	0.11	0.17	0.21	1.2
PEAK	B	C	A	D	E
PL *	0.115	0.115	--	--	--
PC *	0.120	0.120	--	0.24	--

## 6.0. SUMMARY and CONCLUSIONS

Novel high Z chalcogenide semiconductor materials have been synthesized, grown as large crystals and characterized. The energy band gaps for several of the detector materials were determined from transmission and reflection measurements. In addition, we have measured



transient and DC photocurrent of these materials. Many's theoretical model for detector response is adequate for the extraction of  $\mu\tau$  product and surface recombination velocity. Photoconductivity decay measurement in the strongly and weakly absorbed wavelength regions enabled the determination of carrier lifetimes. **Table 11** gives a summary of the most promising materials found in this project.

Further research is needed to optimize and achieve high sensitivity detectors. In particular, we will be growing thicker and higher density samples for more efficient absorption of X-rays and  $\gamma$ -rays. Furthermore low-temperature photoluminescence and photocurrent mapping measurements will be performed to determine the nature of radiative and non-radiative defects, which may limit detector sensitivity. Near field scanning optical microscopy will be used to determine compositional inhomogeneity at the nanoscale. Detector response of selected materials will need to be measured at x-ray and gamma ray energies.

In this work, we effectively addressed the  $E_g$ -Z limiting issue with a materials design concept we call "dimensional reduction" (DR). We showed that compounds containing very high Z elements such as Hg-based binary chalcogenides, which are zero or narrow band gap semiconductors, can form the basis for generating high band gap ( $>1.6$  eV) materials with high specific density and high resistivity. We report here crystal growth, characterization, theoretical band-structure calculations and  $\mu\tau$  measurements of three such "dimensionally reduced" materials that derive from the very dense materials  $\beta$ -HgS, HgSe, and CdTe. We showed that the resulting materials already exhibit properties that are far superior to  $\text{HgI}_2$  and directly comparable to current state-of-the-art compounds such as CZT. Further funding of this approach should result in the significant improvement of their properties and ultimate development of low cost efficient  $\gamma$ -ray detectors.

Table 11.

## Summary of promising detector parameters measured

Sample	$E_g$ (eV)	$(\mu\tau)_e$ $\text{cm}^2/\text{V}$	$(\mu\tau)_h$ $\text{cm}^2/\text{V}$	$(\lambda)_{\mu\tau}$ nm	PL peaks eV	PC peaks eV	$\gamma$ -ray peak keV	$\gamma$ -ray FWHM (%)
Cs <sub>2</sub> HgSn <sub>3</sub> Se <sub>8</sub>	1.96	$1.07 \times 10^{-5}$	$7.95 \times 10^{-6}$	337	N/A	N/A	N/A	N/A
Cs <sub>2</sub> Hg <sub>6</sub> S <sub>7</sub> (CHS-L1)	1.62	$9.0 \times 10^{-4}$	N/A	768	1.57, 1.62, 1.66, 1.68, 1.73	1.50, 1.61, 1.73	122 (broad peak)	25
Cs <sub>2</sub> Hg <sub>6</sub> S <sub>7</sub> (JA2-168)	1.63	$1.92 \times 10^{-3}$	$3.42 \times 10^{-4}$	633	NO PEAKS	signal noisy	122 (broad peak)	23
CsCdInSe <sub>3</sub>	2.4	$1.18 \times 10^{-5}$	$2.42 \times 10^{-6}$	405	Sample too small for PL	Did not measure	N/A	N/A
Cs <sub>2</sub> Hg <sub>6</sub> S <sub>7</sub> (CHS-L2)	1.62	$2.13 \times 10^{-4}$ @ 100 K	$4.27 \times 10^{-4}$ @ 100 K	768	1.57, 1.63, 1.66, 1.68, 1.74	1.50, 1.61, 1.73	122 (broad peak)	21
Cs <sub>2</sub> Hg <sub>6</sub> S <sub>7</sub> (CHS-M)	1.62	N/A signal noisy	N/A signal noisy	768	1.59, 1.63, 1.66, 1.69, 1.74	1.50, 1.61, 1.72	No resolved peak	N/A
Cs <sub>2</sub> Cd <sub>3</sub> Te <sub>4</sub>	2.45	$7.8 \times 10^{-4}$	$2.1 \times 10^{-4}$	633	NO PEAKS	N/A	N/A	N/A
CsCdInTe <sub>3</sub>	1.78	$1.12 \times 10^{-5}$	$8.56 \times 10^{-6}$	405	Sample too small for PL	Did not measure	N/A	N/A
Cd <sub>0.99</sub> Zn <sub>0.01</sub> Te	1.51	$6.6 \times 10^{-4}$	$3.1 \times 10^{-4}$	633	1.55, 1.56, 1.57	1.46, 1.48, 1.49, 1.50, 1.57	122	16

#### PERSONNEL SUPPORTED:

Professor Mercouri Kanatzidis, Professor Bruce Wessels, Professor Arthur J. Freeman

Dr. Shichao Wang (Chemistry)

Ms. Eva Agha (Chemistry)

Ms Sandy Ngyuen (Chemistry)

Dr Vanishri Saligrama (Chemistry)

Dr. John A. Peters, Dr. Zhifu Liu, (Electrical Engineering)

Dr. Hosub Jin, Dr Jino Im (Physics)

Mr. Hao Li (Chemistry)

Ms Maria Sebastian (Materials Science, to graduate Fall 2014)

Chris Malliakas (Chemistry)

Past postdocs: John Androulakis (currently employed at ZTPlus Inc), Simon Johnsen University of Aarhus, Denmark (Assistant Professor)

#### PhD Thesis

Sandy Ngyuen "Crystal Growth and Characterization of Chalcogenide and Chalcogenide Materials"  
Northwestern University, June 2013.

#### INTERACTIONS TRANSITIONS

Invention Disclosures and Provisional Patent Application filed August 2010. "Materials for x-ray and gamma ray detection"

We have initiated discussions with Radiation Monitoring Devices.

#### Honors Awards:

Professor Mercouri Kanatzidis elected Material Research Society Fellow in 2010.

Professor Mercouri Kanatzidis elected Fellow of the American Association for the Advancement of Science in 2012.

Professor Bruce Wessels elected a fellow of Optical Society of America in 2014

#### PUBLICATIONS (acknowledging DTRA support):

- (1) Androulakis, J.; Peter, S. C.; Li, H.; Malliakas, C. D.; Peters, J. A.; Liu, Z. F.; Wessels, B. W.; Song, J. H.; Jin, H.; Freeman, A. J.; Kanatzidis, M. G. Dimensional Reduction: A Design Tool for New Radiation Detection Materials, *Advanced Materials* **2011**, 23, 4163-+.
- (2) Liu, Z. F.; Peters, J. A.; Zang, C.; Cho, N. K.; Wessels, B. W.; Johnsen, S.; Peter, S.; Androulakis, J.; Kanatzidis, M. G.; Song, J. H.; Jin, H.; Freeman, A. J. In *Chemical, Biological, Radiological, Nuclear, and Explosives*; Fountain, A. W., Gardner, P. J., Eds. 2011; Vol. 8018.
- (3) Im, J.; Jin, H.; Li, H.; Peters, J. A.; Liu, Z. F.; Wessels, B. W.; Kanatzidis, M. G.; Freeman, A. J. Formation of native defects in the gamma-ray detector material  $\text{Cs}_2\text{Hg}_6\text{S}_7$ , *Applied Physics Letters* **2012**, 101.
- (4) Li, H.; Peters, J. A.; Liu, Z. F.; Sebastian, M.; Malliakas, C. D.; Androulakis, J.; Zhao, L. D.; Chung, I.; Nguyen, S. L.; Johnsen, S.; Wessels, B. W.; Kanatzidis, M. G. Crystal Growth and Characterization of the X-ray and gamma-ray Detector Material  $\text{Cs}_2\text{Hg}_6\text{S}_7$ , *Crystal Growth & Design* **2012**, 12, 3250-3256.
- (5) Li, H.; Malliakas, C. D.; Liu, Z. F.; Peters, J. A.; Jin, H.; Morris, C. D.; Zhao, L. D.; Wessels, B. W.; Freeman, A. J.; Kanatzidis, M. G.  $\text{CsHgInS}_3$ : a New Quaternary Semiconductor for gamma-ray Detection, *Chemistry of Materials* **2012**, 24, 4434-4441.
- (6) Peters, J. A.; Cho, N. K.; Liu, Z. F.; Wessels, B. W.; Li, H.; Androulakis, J.; Kanatzidis, M. G. Investigation of defect levels in  $\text{Cs}_2\text{Hg}_6\text{S}_7$  single crystals by photoconductivity and photoluminescence spectroscopies, *Journal of Applied Physics* **2012**, 112.
- (7) Li, H.; Malliakas, C. D.; Peters, J. A.; Liu, Z. F.; Im, J.; Jin, H.; Morris, C. D.; Zhao, L. D.; Wessels, B. W.; Freeman, A. J.; Kanatzidis, M. G.  $\text{CsCdInQ}_3$  (Q = Se, Te): New Photoconductive Compounds As Potential Materials for Hard Radiation Detection, *Chemistry of Materials* **2013**, 25, 2089-2099.
- (8) Liu, Z.; Peters, J. A.; Li, H.; Kanatzidis, M. G.; Wessels, B. W. Transient photocurrent measurements in alkali chalcogenide ternary compound semiconductors, *Semiconductor Science and Technology* **2013**, 28.
- (9) Morris, C. D.; Li, H.; Jin, H.; Malliakas, C. D.; Peters, J. A.; Trikalitis, P. N.; Freeman, A. J.; Wessels, B. W.; Kanatzidis, M. G.  $\text{Cs}_2\text{M(II)M(3)(IV)Q}_8$  (Q=S, Se, Te): An Extensive Family of Layered Semiconductors with Diverse Band Gaps, *Chemistry of Materials* **2013**, 25, 3344-3356.
- (10) Li, Hao; Malliakas, Christos; Liu, Zhifu; Peters, John; Sebastian, Maria; Zhao, Li-Dong; Chung, Duck Young; Wessels, Bruce; Kanatzidis, Mercouri "Investigation of semi-insulating  $\text{Cs}_2\text{Hg}_6\text{S}_7$  and  $\text{Cs}_2\text{Hg}_{6-x}\text{Cd}_x\text{S}_7$  alloy for hard radiation detection" *Crystal Growth & Design*, 2014, in press.

#### **Opportunities for training and professional development**

These young scientists attended the MRS Meeting in San Francisco (April 2013) and attended the symposium "Gamma-Ray and Neutron Detector Materials". Sandy Nguyen also attended and presented in the SPIE Conference in Sand Diego August 12-15, 2012. One student and one postdoc also attended and presented posters at the DTRA Grantees conference in Alexandria VA (July 2012). This year these students and postdocs will attend the Annual DTRA Grantees Conference in VA in July 2013.

#### **"Training" activities**

Ms. Maria Sebastian, a Ph.D. graduate student in Materials Science at Northwestern University, has been involved in one-on-one training with her mentor, Dr. J. A. Peters, an expert with advanced professional skills and experience in semiconductor analysis.

#### “Professional development”

Dr. Zhifu Liu attended the SPIE 2012 Symposium on Hard X-ray, Gamma ray, and Neutron Detector Physics held in San Diego, California. He presented our research findings and communicated with experts from government agencies, academia, and industry.

Dr. John A. Peters attended the 2012 DTRA grantees conference that was held in the Washington, DC metropolitan area. His poster focused on the optical characterization of Cs-based semiconductor compounds and radiation detection measurements.

Dr. Jino Im attended the 2012 American Physical Society meeting and presented his ARI funded work there in an oral presentation.

#### **Conference presentations**

1. APS March Meeting 2013 , Monday–Friday, February 27–March 2 2013; Boston, Massachusetts, Session V7: Focus Session: Computational Design of Materials - Engineering of Electronic Structure Materials, Mercouri Kanatzidis, Title: Dimensional Reduction: A design tool for new semiconductor compounds for radiation detection.
2. Hao Li, Christos D. Malliakas, Zhifu Liu, John A. Peters, Hosub Jin, Jino Im, Maria Sebastian, Bruce W. Wessels, Arthur J. Freeman and Mercouri G. Kanatzidis Title: New Cs compound semiconductors for X-ray and gamma ray detection, in *Symposium WW: Nuclear Radiation Detection Materials*, 2013 MRS Spring Meeting, April 1-5, 2013, San Francisco, California (April 2013).
3. Zhifu Liu, John A. Peters, Sandy Nguyen, Maria Sebastian, Bruce W. Wessels, Shichao Wang, Hosub Jin, Jino Im, Arthur J. Freeman, and Mercouri G. Kanatzidis, “Characterization of thallium-based ternary semiconductor compounds for radiation detection,” in *Hard X-Ray, Gamma-Ray, and Neutron Detector Physics XIV*, SPIE 2012 Symposium, August 14, 2012, San Diego, California (August 2012). Acknowledgement of federal support: YES.
4. American Chemical Society, National Meeting & Exposition, Anaheim CA, March 27, 2011. “New Metal Chalcogenides and their Diverse Properties”, Mercouri G Kanatzidis, Department of Chemistry, Northwestern University, Evanston IL 60208, ACS Award in Inorganic Chemistry: Symposium in Honor of Robert J. Cava (invited). Acknowledgement of federal support: YES.
5. 243<sup>rd</sup> ACS National Meeting and Exposition, San Diego, California March 25 - 29, 2012 Dimensional reduction: A design tool for new radiation detection materials Mercouri G Kanatzidis, Department of Chemistry, Northwestern University, Evanston, Illinois 60208, United States (invited). Acknowledgement of federal support: YES.
6. J.A. Peters, Nam Ki Cho, Zhifu Liu, B. W. Wessels,, J. Androulakis, M. G. Kanatzidis, H. Jin and A. Freeman, “Dimensional Reduction: A design tool for new semiconductor compounds for radiation detection”, contributed talk given at the APS 2012 March Meeting, Boston, MA. Acknowledgement of federal support: YES.
7. SPIE Conference, Optical Engineering and Applications, 12 - 16 August 2012, San Diego, CA, Symposium: Hard X-Ray, Gamma-Ray, and Neutron Detector Physics XIV. Solid state chemistry approach to new hard radiation detection, materials (*Invited Paper*), Mercouri G. Kanatzidis, Hao Li, Sandy Nguyen, John Androulakis, Christos D. Malliakas, John A. Peters, Zhifu Liu, Hosub Jin, Arthur J. Freeman, Bruce W. Wessels, Northwestern University. Acknowledgement of federal support: YES.
8. SPIE Conference, Optical Engineering and Applications, 12 - 16 August 2012, San Diego, CA, Symposium: Hard X-Ray, Gamma-Ray, and Neutron Detector Physics XIV. Characterization of

thallium-based ternary semiconductor, compounds for radiation detection, Zhifu Liu, John A. Peters, Maria Sebastian, Bruce W. Wessels, Sandy Nguyen, Shichao Wang, Mercuri G. Kanatzidis, Hosub Jin, Arthur J. Freeman, Northwestern University. Acknowledgement of federal support: YES.

**DEPARTMENT OF DEFENSE**

DEFENSE THREAT REDUCTION  
AGENCY  
8725 JOHN J. KINGMAN ROAD  
STOP 6201  
FORT BELVOIR, VA 22060  
ATTN: A. LYALIKOV

DEFENSE TECHNICAL  
INFORMATION CENTER  
8725 JOHN J. KINGMAN ROAD,  
SUITE 0944  
FT. BELVOIR, VA 22060-6201  
ATTN: DTIC/OCA

**DEPARTMENT OF DEFENSE  
CONTRACTORS**

QUANTERION SOLUTIONS, INC.  
1680 TEXAS STREET, SE  
KIRTLAND AFB, NM 87117-5669  
ATTN: DTRIAC